

A SEARCH FOR STARS OF VERY LOW METAL ABUNDANCE. VI. DETAILED ABUNDANCES OF 313 METAL-POOR STARS¹

IAN U. ROEDERER,^{2,4} GEORGE W. PRESTON,² IAN B. THOMPSON,² STEPHEN A. SHECTMAN,² CHRISTOPHER SNEDEN,³
GREGORY S. BURLEY,² DANIEL D. KELSON²

Accepted for publication in the Astronomical Journal

ABSTRACT

We present radial velocities, equivalent widths, model atmosphere parameters, and abundances or upper limits for 53 species of 48 elements derived from high resolution optical spectroscopy of 313 metal-poor stars. A majority of these stars were selected from the metal-poor candidates of the HK Survey of Beers, Preston, and Shtetman. We derive detailed abundances for 61% of these stars for the first time. Spectra were obtained during a 10-year observing campaign using the Magellan Inamori Kyocera Echelle spectrograph on the Magellan Telescopes at Las Campanas Observatory, the Robert G. Tull Coudé Spectrograph on the Harlan J. Smith Telescope at McDonald Observatory, and the High Resolution Spectrograph on the Hobby-Eberly Telescope at McDonald Observatory. We perform a standard LTE abundance analysis using MARCS model atmospheres, and we apply line-by-line statistical corrections to minimize systematic abundance differences arising when different sets of lines are available for analysis. We identify several abundance correlations with effective temperature. A comparison with previous abundance analyses reveals significant differences in stellar parameters, which we investigate in detail. Our metallicities are, on average, lower by ≈ 0.25 dex for red giants and ≈ 0.04 dex for subgiants. Our sample contains 19 stars with $[\text{Fe}/\text{H}] \leq -3.5$, 84 stars with $[\text{Fe}/\text{H}] \leq -3.0$, and 210 stars with $[\text{Fe}/\text{H}] \leq -2.5$. Detailed abundances are presented here or elsewhere for 91% of the 209 stars with $[\text{Fe}/\text{H}] \leq -2.5$ as estimated from medium resolution spectroscopy by Beers, Preston, and Shtetman. We will discuss the interpretation of these abundances in subsequent papers.

Subject headings: Galaxy: halo — nuclear reactions, nucleosynthesis, abundances — stars: abundances — stars: atmospheres — stars: Population II

1. INTRODUCTION

Observations of the high redshift Universe reveal carbon, magnesium, and other metals in the clouds of hydrogen that fueled the rising star formation rate density during the first several Gyr after the Big Bang (e.g., Sargent et al. 1988; Cooke et al. 2011; Matejek & Simcoe 2012). Surely some of those gas clouds evolve into galaxies like today’s Milky Way, whose stellar halos retain a chemical memory of those early epochs of star formation and metal production. If, however, one is interested in studying the early nucleosynthesis of less abundant metals, like holmium (Snedden et al. 1996) or uranium (Cayrel et al. 2001), stars in the Milky Way are the only practical targets. For this and many other reasons, the importance of expanding the inventory of halo stars whose heavy metal abundances are known in great detail has long been recognized.

¹ This paper includes data gathered with the 6.5 meter Magellan Telescopes located at Las Campanas Observatory, Chile, and The McDonald Observatory of The University of Texas at Austin. The Hobby-Eberly Telescope is a joint project of the University of Texas at Austin, the Pennsylvania State University, Stanford University, Ludwig-Maximilians-Universität München, and Georg-August-Universität Göttingen.

² Carnegie Observatories, 813 Santa Barbara St., Pasadena, CA 91101, USA

³ Department of Astronomy, University of Texas at Austin, 1 University Station, C1400, Austin, TX 78712, USA

⁴ Present address: Department of Astronomy, University of Michigan, 500 Church Street, Ann Arbor, MI 48109, USA; iur@umich.edu

1.1. Previous Surveys of Metal-Poor Stars

Noteworthy in regard to the storyline of the present study are the surveys of Bond (1970, 1980) and Bidelman & MacConnell (1973). The photographic plates for their objective-prism surveys were taken with the University of Michigan’s 0.61 m Curtis Schmidt Telescope. This telescope, initially located near Ann Arbor, was relocated in 1966 to Cerro Tololo Inter-American Observatory (CTIO). Most of the observations for Bond (1970) were made in Michigan, while Bidelman & MacConnell and Bond (1980) made their observations at CTIO. Bond also used Strömgren photometry to assign spectral types and luminosity classes to his candidates, and he measured radial velocities from followup coudé spectroscopy when possible.

Many of the well-known and bright metal-poor stars in the Henry Draper (HD), Bonner Durchmusterung (BD), or Córdoba Durchmusterung (CD) Catalogs were identified during this period by these surveys. Other metal-poor stars were found among the high proper motion stars in the Lowell Proper Motion Survey (Giclas et al. 1971, 1978; these stars are identified with a “G” prefix before their catalog designation) and the New Luyten Two Tenths Catalog (NLTT, Luyten 1979). Ryan (1989) discusses the methods used to identify metal-poor stars in these surveys.

1.2. The HK Objective-Prism Survey

Our own work on the subject began with an objective-prism survey at the Curtis Schmidt (CS) Telescope at

CTIO, initiated by G. Preston and S. Shectman, in 1978–1979. The key advance was the use of an interference filter to expose only the region around the stellar Ca II H and K absorption lines at a spectral resolution of $\approx 5 \text{ \AA}$ ($R \equiv \lambda/\Delta\lambda \sim 800$). This interference filter reduced crowding and sky fog and allowed longer exposure times (90 minutes) than had been practical previously. The “HK” Survey plates reach $B \approx 15$, several magnitudes fainter than the surveys of Bond (1970, 1980) and Bidelman & MacConnell (1973). Visual inspection of the plates using a low-power binocular microscope yielded about 1800 metal-poor candidate stars on 72 plates.

Broadband *UBV* photometry and followup medium resolution (1 \AA ; $R \sim 4,000$) spectroscopy covering the 3700–4500 \AA wavelength range were obtained for 450 candidates. Beers, Preston, & Shectman (1985) presented metallicity estimates for 134 metal-poor candidates with $[\text{Fe}/\text{H}] < -2.0$. Using a revised metallicity calibration (Beers et al. 1990), Beers, Preston, & Shectman (1992; hereafter BPS92) published metallicity estimates, radial velocity measurements, and distances for 1044 dwarfs and giants with subsolar $[\text{Fe}/\text{H}]$ from 135 unique fields covering 3375 square degrees (8% of the sky).

The relocation of Case Western Reserve University’s Burrell Schmidt (BS) Telescope from Cleveland to Kitt Peak National Observatory (KNPO) in 1979 enabled a similar survey in the Northern Hemisphere. Followup medium resolution spectroscopy for these candidates was not yet available in 1992. Beers (2013) describes the impressive worldwide network of 2–4 m class telescopes involved in the subsequent medium resolution spectroscopic followup of metal-poor candidates from both the Northern and Southern portions of the HK Survey. Detailed abundances of metal-poor candidates from the Northern portion of the HK Survey have been published elsewhere (e.g., Honda et al. 2004a,b; Lai et al. 2004, 2008) and will not be considered in the sample presented here.

An analysis of digital scans of the original HK Survey plates was made by Rhee (2001) and in subsequent unpublished work by J. Rhee, T. Beers, and coworkers (see also Section 3.3.1 of Beers & Christlieb 2005). The goal of this “HK-II” Survey was to identify metal-poor red giant stars that may have been overlooked in the original visual scans of the plates due to the unavoidable temperature bias against cool stars. These candidates will not be considered in the sample presented here.

1.3. Subsequent Surveys

The Hamburg/ESO (HE) Survey (Wisotzki et al. 2000) introduced quantitative methods to identify metal-poor candidates from digitized spectra (Christlieb et al. 2008). These techniques increase the effective yields of genuine metal-poor stars, especially among giants, when color information is included as part of the selection criteria. This survey also reaches several magnitudes deeper than the HK Survey.

Recent surveys have built on these quantitative techniques to identify even greater numbers of candidate metal-poor stars from low resolution spectroscopy, including the Radial Velocity Experiment (RAVE; see Fulbright et al. 2010), the Sloan Digital Sky Survey (SDSS),

and the Sloan Extensions for Galactic Understanding and Exploration (SEGUE-1 and SEGUE-2; Yanny et al. 2009; Rockosi 2012). Many metal-poor candidates are also expected to be found among ongoing surveys by the Large sky Area Multi-Object fiber Spectroscopic Telescope (LAMOST; e.g., Deng et al. 2012); and the SkyMapper Telescope (Keller et al. 2012).

1.4. Detailed Abundance Followup of Metal-Poor Candidates

Bright stars identified by the surveys of Bond (1970, 1980) and Bidelman & MacConnell (1973) have been analyzed in great chemical detail by numerous investigators, including Luck & Bond (1981, 1985), Hartmann & Gehren (1988), Gilroy et al. (1988), Gratton & Sneden (1988, 1991, 1994), Magain (1989), Peterson et al. (1990), Zhao & Magain (1990), and Johnson (2002). Ryan et al. (1991), Fulbright (2000, 2002), Stephens & Boesgaard (2002), and Ishigaki et al. (2010) studied the compositions of stars selected from the early objective prism and proper motion surveys. Detailed abundance studies of large samples of stars from the HE Survey have been conducted by Carretta et al. (2002), Cohen et al. (2002, 2004, 2008), Barklem et al. (2005), Aoki et al. (2007), Hollek et al. (2011), Norris et al. (2013), and Yong et al. (2013). Candidates from the HK-II Survey have been observed as part of the Chemical Abundances of Stars in the Halo (CASH) project at the University of Texas (Frebel et al. 2008b; Roederer et al. 2008b). Detailed chemical followup of large numbers of stars from the SDSS and SEGUE have been performed by Aoki et al. (2008, 2013), Caffau et al. (2011), and Bonifacio et al. (2012).

Over the last several decades, high resolution optical spectroscopic followup of candidates from BPS92 has confirmed hundreds of them as genuine metal-poor stars. Chemical abundances of handfuls of stars from Beers et al. (1985) were presented by Molaro & Bonifacio (1990), Molaro & Castelli (1990), Norris et al. (1993), and Primas et al. (1994). McWilliam et al. (1995a,b), Norris et al. (1996), and Ryan et al. (1996) were the first to analyze larger samples of stars (34 stars between them) from BPS92. Since then, the number of detailed abundance studies conducted on candidates from BPS92 has grown tremendously, and there are far too many excellent ones to list here individually. There have been several dedicated observing campaigns to obtain high resolution spectroscopy of substantial numbers of stars (typically ≈ 10 –30), including analyses by Aoki et al. (2005, 2007), Honda et al. (2004a,b), Lai et al. (2008), the “First Stars” team (Cayrel et al. 2004; Spite et al. 2005; François et al. 2007; Bonifacio et al. 2009), and a reanalysis of the published values from many of these studies by Yong et al. (2013).

The detailed chemical analysis performed by McWilliam et al. (1995a,b) launched our efforts to use these stars as probes of the earliest epoch of metal enrichment in the Galaxy. Our subsequent abundance studies based on high resolution spectroscopy of metal-poor candidates from the HK Survey have examined carbon rich metal-poor stars (Preston & Sneden 2001; Sneden et al. 2003; Roederer et al. 2014), individual stars of interest (Sneden et al. 1994; Ivans et al. 2005; Preston et al. 2006b; Thompson et al. 2008), stars on the

horizontal branch (Preston et al. 2006a), and stars with kinematics indicative of a cold stellar stream (Roederer et al. 2010).

In this paper we present abundance results for 313 stars, including 217 stars from the HK Survey, using high resolution spectroscopy obtained from 2003–2013 at the Magellan Telescopes at Las Campanas Observatory. As of July, 2013, detailed abundances for 91% (191/209) of the stars with estimated $[\text{Fe}/\text{H}] \leq -2.5$ in BPS92 are presented here or have been published elsewhere previously. Sixty-one percent (132/217) of the stars from the HK Survey presented in this work are analyzed in such a manner for the first time. Abundances in the other 85 stars have been examined previously by the studies above or others named below. A limited selection of stars from the BD, CD, G, HD, and HE catalogs are also (re)analyzed in the present study.

2. ABUNDANCE NOTATION

We adopt standard definitions of elemental abundances and ratios. For element X, the logarithmic absolute abundance is defined as the number of atoms of element X per 10^{12} hydrogen atoms, $\log \epsilon(\text{X}) \equiv \log_{10}(N_{\text{X}}/N_{\text{H}}) + 12.0$. For elements X and Y, the logarithmic abundance ratio relative to the solar ratio is defined as $[\text{X}/\text{Y}] \equiv \log_{10}(N_{\text{X}}/N_{\text{Y}}) - \log_{10}(N_{\text{X}}/N_{\text{Y}})_{\odot}$.

Abundances or ratios denoted with the ionization state are defined to be the total elemental abundance as derived from transitions of that particular ionization state after ionization corrections, assuming Saha (1921) equilibrium, have been applied. For example, $\log \epsilon(\text{Fe II})$ denotes the number density of all iron atoms as derived from Fe II lines.

When reporting relative abundance ratios for a specific element X (e.g., $[\text{X}/\text{Fe}]$), these ratios are constructed by comparing total abundances derived from species in the same ionization state. For example, if X is a neutral species, the ratio $[\text{X}/\text{Fe}]$ is calculated using the total abundance of element X derived from the neutral species with the total iron abundance derived from Fe I. Similarly, if X is an ionized species, the ratio $[\text{X}/\text{Fe}]$ is calculated using the total abundance of element X derived from the ionized species with the total iron abundance derived from Fe II.

3. OBSERVATIONS

3.1. Target Selection

Over the course of this program we have observed 88% (184/209) of the stars with estimated $[\text{Fe}/\text{H}] \leq -2.5$ in BPS92, excluding three duplicate identifications in Table 5 of BPS92. Abundances derived from previous moderate or high resolution spectroscopy of seven of the remaining 25 stars have been presented elsewhere by Norris et al. (1993), Spite et al. (2000), Preston & Sneden (2001), Lai et al. (2004), and T. Masseron et al. (unpublished; see Masseron et al. 2010). The 18 remaining unobserved candidates are faint by our standards, $V > 14.5$, and most are fainter than $V > 15.0$.

We also observed other metal-poor stars to expand the sample to higher metallicity and into the Northern hemisphere. These additional targets include higher metallicity candidates from BPS92 and bright stars from the catalogs discussed in Section 1. Some of these stars have

TABLE 1
REPEAT STAR IDENTIFICATIONS

Primary Name	Additional Designations
CS 22169–035	HE 0409–1212
CS 22172–029	HE 0328–1047
CS 22185–007	HE 0315–1528
CS 22189–009	HE 0239–1340
CS 22873–128	HE 2002–5843
CS 22886–003	CS 29512–030
CS 22886–012	CS 29512–015
CS 22886–013	CS 29512–013
CS 22888–014	CS 30493–023
CS 22890–064	CS 30306–117
CS 22892–052	HE 2214–1654
CS 22894–023	CS 22952–011
CS 22937–072	CS 29501–051
	CS 30492–102
CS 22942–002	HE 0044–2459
CS 22948–066	CS 30343–064
CS 22949–037	HE 2323–0256
CS 22952–015	HE 2334–0604
CS 22954–015	HE 0236–0242
CS 22957–027	HE 2356–0410
CS 22968–014	HE 0305–5442
CS 29517–042	CS 31060–052
CS 30339–069	HE 0027–3613

been previously analyzed elsewhere. Our final sample includes observations of 217 stars from the HK Survey and 96 stars from other sources.

All stars in our sample are present in the SIMBAD database, and their coordinates may be found there. During the course of the objective-prism survey, portions of some fields were observed multiple times with different plates. This led to multiple identification numbers for a few candidates. In such cases we adopt the number associated with the earliest observation. Table 1 lists the stars in our survey that received multiple identification numbers. Several of these stars were also rediscovered during the course of the HE Survey, and the HE designations are listed in Table 1. The HK Survey itself rediscovered stars with previous catalog names, and these are listed in Table 6 and on page 2033 of BPS92.

3.2. High Resolution Spectroscopy

Observations conducted at Las Campanas Observatory were made with the Magellan Inamori Kyocera Echelle (MIKE) spectrograph (Bernstein et al. 2003). This instrument is currently mounted on the f/11 Nasmyth platform at the 6.5 m Landon Clay Telescope (Magellan II). Early observations for our program were taken while MIKE was mounted on the 6.5 m Walter Baade Telescope (Magellan I) in 2003. The MIKE spectra were taken with the $0''.7 \times 5''.0$ slit, yielding a resolving power of $R \sim 41,000$ in the blue and $R \sim 35,000$ in the red as measured from isolated ThAr lines. A dichroic splits the two arms around 4950 Å, although the wavelength at the split is bluer in earlier observations. This setup gives approximately 2.4 pixels per resolution element (RE) in the blue and 2.1 pixels RE⁻¹ in the red. Many of the observations taken in 2003 and 2004 were made using the double aperture $0''.7 \times 2''.0$ slit (“A-B mode”). In this mode, exposures are made with the star in aperture A and the sky in aperture B simultaneously; the pattern is then reversed for the subsequent exposure. This observing procedure was adopted to optimize sky subtraction

for faint targets. This strategy proved unnecessary for our targets, which are not sky-noise limited, and all subsequent MIKE observations were made using the single $0''.7 \times 5''.0$ slit. This setup achieves complete wavelength coverage from 3350–9150 Å, although some of the early exposures only extend to 7250 Å in the red.

For the exposures made in the A-B mode, bias subtraction, flat-fielding, sky and scattered light subtraction, cosmic ray removal, and correction of the slit tilt were accomplished with software written by S.A.S. Aperture extraction, wavelength calibration (derived from ThAr frames taken before or after each stellar integration), co-addition of separate observations, and continuum normalization were performed within the IRAF environment. For the exposures made using the single $0''.7 \times 5''.0$ slit, data reduction, extraction, and wavelength calibration were performed using the MIKE data reduction pipeline written by D. Kelson (see also Kelson 2003). Observations were often broken into several sub-exposures (not longer than 2400 s per sub-exposure). We refer to the addition of these sub-exposures as one observation. Coaddition of repeat observations and continuum normalization were performed within the IRAF environment.

Other observations were made with the Robert G. Tull Coudé Spectrograph (Tull et al. 1995) on the 2.7 m Harlan J. Smith Telescope at McDonald Observatory. These spectra were taken with the $2''.4 \times 8''.0$ slit, yielding a resolving power $R \sim 33,000$ and approximately 4.0 pixels RE^{-1} . This setup delivers complete wavelength coverage from 3700–5700 Å, with small gaps between the echelle orders further to the red. For our abundance analysis we only use the spectra blueward of 8000 Å.

Additional observations were made with the High Resolution Spectrograph (HRS; Tull 1998) on the 9.2 m Hobby-Eberly Telescope (Ramsey et al. 1998) at McDonald Observatory. These exposures were taken during the standard queue observing mode (Shetrone et al. 2007). Using the $1''.0$ slit yields a resolving power $R \sim 30,000$ and approximately 3.1 pixels RE^{-1} . In the bluest cross-dispersion setting this instrument delivers complete wavelength coverage from 3900–6800 Å.

For the data obtained with the Tull Spectrograph and HRS, reduction, extraction, sky and scattered light removal, and wavelength calibration (derived from ThAr exposures taken before or after each stellar exposure) of the spectra were accomplished using the REDUCE software package (Piskunov & Valenti 2002). These observations were also broken into several sub-exposures with exposure times typically not longer than 1800 s. Coaddition and continuum normalization were performed within the IRAF environment.

We have observed 250 stars with Magellan+MIKE, 52 stars with Smith+Tull, and 19 stars with HET+HRS. After accounting for duplicate observations of the same star and three double-lined spectroscopic binaries whose abundances are not examined in this paper, we are left with a total of 313 stars. These 532 individual observations account for nearly 495 hours of integration time. In Table 2 we present a record of all observations. A full version of Table 2 is available in the online edition of the journal.

Signal to noise (S/N) estimates, listed in Table 3, are

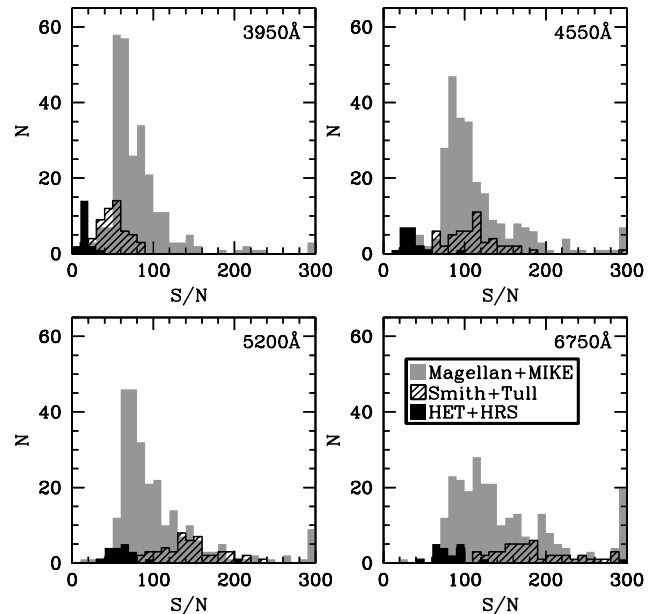


FIG. 1.— S/N estimates at four wavelengths. The gray shaded histogram represents spectra obtained with the MIKE spectrograph, the hatched histogram represents spectra obtained with the Tull spectrograph, and the black shaded histogram represents spectra obtained with the HRS. The last bar to the right in each panel indicates the number of stars with $S/N > 300/1$.

based on Poisson statistics for the number of photons collected in the continuum at several reference wavelengths once all observations of a given target have been coadded together. Spectra obtained with different instruments were not coadded. These S/N estimates are illustrated in Figure 1. We have succeeded in achieving a relatively high S/N at 3950 Å, between the Ca II H and K lines, for most stars observed with the MIKE and Tull spectrographs ($S/N \gtrsim 50$ and 40, respectively). The HRS is not optimized for blue response, and similar S/N levels were not practical in stars observed with this setup. The S/N continues to increase when moving toward the red for stars observed with all three instruments. High S/N levels in the blue region of the spectrum are essential for deriving abundances of many species whose most promising transitions are found in this spectral region.

4. RADIAL VELOCITIES

To measure the radial velocity (RV) of each of our target stars, we cross correlate our spectra against standard template stars using the *fxcor* task in IRAF. The RV with respect to the ThAr lamp is found by cross correlating the echelle order containing the Mg I b lines. For spectra taken with the MIKE and Tull spectrographs, we also cross correlate the echelle order containing the telluric O₂ B band near 6900 Å with a template to remove any velocity shifts resulting from thermal and mechanical motions in the spectrographs. We use empirical O₂ wavelengths from Griffin & Griffin (1973) to create this zero-velocity template from one spectrum with high S/N ratios obtained with each instrument. The HRS spectra do not contain this band, and we cross-correlate against the telluric O₂ α band near 6300 Å using laboratory wavelengths from Babcock & Herzberg (1948). These measurements are consistent with no shift. Heliocentric

TABLE 2
LOG OF OBSERVATIONS

Star	Telescope/ Instrument	Observer	Exp. time (s)	Date	UT mid- exposure	Heliocentric JD	Heliocentric V_r (km s $^{-1}$)
CS 22166–016	Magellan-Clay/MIKE	GWP	1600	2004 Aug 12	10:19	2453229.934	−210.0
CS 22169–008	Magellan-Clay/MIKE	IBT	4000	2004 Sep 23	08:55	2453271.874	+184.2
CS 22169–035	Magellan-Baade/MIKE	GWP	1400	2003 Jan 18	04:22	2452657.684	+15.4
CS 22169–035	Magellan-Baade/MIKE	GWP	2400	2003 Jan 20	02:05	2452659.589	+14.1
CS 22169–035	Magellan-Clay/MIKE	GWP	1700	2007 Aug 24	09:56	2454336.914	+14.1
CS 22171–031	Magellan-Clay/MIKE	GWP	2800	2008 Sep 10	07:59	2454719.837	+38.8
CS 22171–037	Magellan-Clay/MIKE	IBT	7200	2003 Nov 01	05:53	2452944.750	−261.4
CS 22171–037	Magellan-Clay/MIKE	IUR	7200	2012 Aug 26	06:12	2456165.762	−261.1

NOTE. — The complete version of Table 2 is available online only. A short version is shown here to illustrate its form and content.

TABLE 3
OBSERVATIONAL STELLAR DATA

Star	$\langle RV \rangle$ (km s $^{-1}$)	Binary flag ¹	Literature RV Ref.	Total exp. time (s)	No. obs.	S/N 3950Å	S/N 4550Å	S/N 5200Å	S/N 6750Å
CS 22166–016	−210.0	1	1	1600	1	115	175	95	140
CS 22169–008	+184.2	0	...	4000	1	100	135	70	95
CS 22169–035	+14.5	1	2	5500	3	75	135	170	285
CS 22171–031	+38.8	0	...	2800	1	60	80	70	115
CS 22171–037	−261.3	1	...	14400	2	95	125	125	180
CS 22172–029	...	2	3	7600	2	80	110	105	180

REFERENCES. — (1) Giridhar et al. 2001; (2) Bonifacio et al. 2009; (3) Barklem et al. 2005; (4) Honda et al. 2004a; (5) McWilliam et al. 1995a; (6) Lai et al. 2008; (7) Aoki et al. 2002a; (8) Tsangarides et al. 2004; (9) Cohen et al. 2002; (10) Lai et al. 2004; (11) Preston 2009; (12) Preston et al. 2006a; (13) Hollek et al. 2011; (14) Preston & Sneden 2001; (15) Primas et al. 1994; (16) Norris et al. 2001; (17) Depagne et al. 2002; (18) Preston & Sneden 2000; (19) Norris et al. 1997; (20) Bonifacio et al. 1998; (21) Roederer et al. 2014; (22) Sivarani et al. 2006; (23) Aoki et al. 2007; (24) Sneden et al. 2003; (25) Aoki et al. 2002b; (26) Sbordone et al. 2010; (27) Aoki et al. 2009; (28) Hill et al. 2002; (29) Carney et al. 2003; (30) Zhang et al. 2009; (31) Latham et al. 2002; (32) Latham et al. 1991; (33) Ito et al. 2013; (34) Carney et al. 2008; (35) Pourbaix et al. 2004; (36) Bonifacio et al. 1999; (37) Norris 1986; (38) Nordström et al. 2004; (39) Gratton & Sneden 1994; (40) Roederer et al. 2008a; (41) Ryan & Norris 1991; (42) Aoki et al. 2002c; (43) Van Eck et al. 2003; (44) Lucatello et al. 2005; (45) Cohen et al. 2008; (46) Fulbright 2002

NOTE. — The complete version of Table 3 is available online only. A short version is shown here to illustrate its form and content.

¹ Binary flags: (0) unknown binary status; (1) no RV variations detected in multiple epochs; (2) RV variations detected, suspected binary, no systemic velocity listed; (3) spectroscopic binary confirmed by other studies, systemic velocity listed.

corrections are computed using the IRAF *rvcorrect* task. Heliocentric RV measurements for each observation are listed in Table 2.

Table 3 lists the mean RV derived for each of our targets. We have searched the literature for previous RV measurements to identify stars that are members of binary or multiple star systems. We compare our heliocentric RV measurements to those measured by previous investigators. These references are listed in Table 3. Our measurements for known RV-constant stars are all in good agreement with previous investigations. Typical RV uncertainties for previous studies are ≈ 1 km s $^{-1}$ when the previous measurement was made from high resolution spectra, and RV uncertainties are often several km s $^{-1}$ for lower resolution data. Panel A of Figure 2 displays the RV differences that arise from comparison of our mean measurements to those obtained by previous investigations. We only make this comparison when the previous study reported an error less than 1 km s $^{-1}$; many of these stars also have been observed at many epochs (i.e., $\gg 3$), so it is probable that they are indeed RV constant. For the 160 measurements presented in

Panel A, $\sigma = 0.81$ km s $^{-1}$. Panel B compares the differences when a single measurement is compared to the mean of other measurements made by us of the same star for stars that show no RV variations in excess of 2 km s $^{-1}$. This subset has $\sigma = 0.64$ km s $^{-1}$. For a sample of 95 observations, the total shown in Panel B, and a normal distribution with a dispersion of 0.64 km s $^{-1}$, we would expect less than one observation to deviate by more than 2 km s $^{-1}$. This suggests that 2 km s $^{-1}$ is a reasonable discriminant for identifying RV constant stars at the $\approx 3\sigma$ level. Based on these tests, we estimate a total uncertainty in each RV measurement of ≈ 0.6 –0.8 km s $^{-1}$.

Column 3 of Table 3 indicates the binary status of each star. A flag of “0” indicates that the star has only been observed during a single epoch (e.g., one observation, or several observations separated in time by less than one week). For stars lacking RV variations during this limited time, we assume that we cannot distinguish between a single star or a multiple star system with a relatively long orbital period, so we classify the binary nature of these stars as unknown. A flag of “1” indicates that the

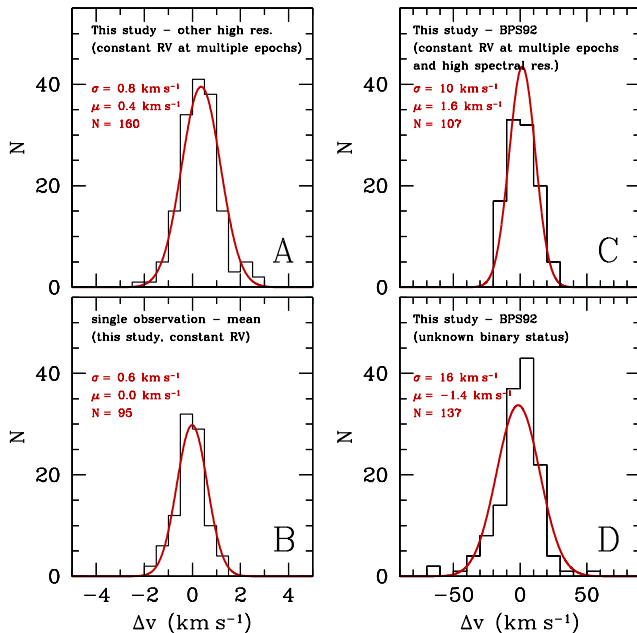


FIG. 2.— Differences in our measured RV displayed as histograms when compared to RV constant stars observed by other investigators (Panel A), repeated measurements of RV constant stars made by us (Panel B), measurements made from moderate resolution spectroscopy by BPS92 of RV constant stars (Panel C), and measurements made from moderate resolution spectroscopy by BPS92 for stars with an unknown binary status (Panel D). The mean (μ), standard deviation (σ), and number of points included (N) are listed in each panel.

star has been observed in multiple epochs, either by us or in combination with previous investigators, and does not exhibit any RV variations beyond the mutual uncertainties of the measurements. A flag of “2” indicates that the star exhibits RV variations, either in our measurements or in combination with previous investigators. These stars are likely in binary or multiple star systems, but we lack sufficient information to determine an orbital solution or systemic RV. A flag of “3” indicates that the star has previously been identified as a member of a binary or multiple star system. For these stars, we list the systemic velocity as determined by Preston & Sneden (2000, 2001), Latham et al. (2002), Carney et al. (2003), Sneden et al. (2003), Pourbaix et al. (2004), or Roederer et al. (2014).

Many of our targets from the HK Survey have not been observed previously at high spectral resolution, but BPS92 made RV estimates from moderate resolution ($\sim 1\text{\AA}$) spectroscopy. Figure 2 also displays the differences in RV measured from the moderate resolution and high resolution spectroscopy. Panel C shows the differences for stars that have been observed at high spectral resolution at multiple epochs (either by us or in combination with other investigators) and do not exhibit any RV variations as measured from the high resolution spectroscopy. The standard deviation, 10 km s^{-1} , is identical to the uncertainty estimate reported by BPS92, and the mean offset is only 1.6 km s^{-1} . This indicates that their estimates are generally reliable. Panel D shows the differences for stars that have only been observed at high spectral resolution at a single epoch. The larger σ of this sample, 18 km s^{-1} , leads us to speculate that at least

TABLE 4
STARS WITH DEVIANT RV MEASUREMENTS IN BPS92

Star	BPS92 RV (km s^{-1})	High res. RV ^a (km s^{-1})	Other Ref. ^a
CS 22892–052	−75	+13.0	1, 2
CS 22945–058	−36	+23.4	...
CS 22949–037	−79	−125.4	1, 3
CS 22949–048	−95	−160.8	1
CS 22954–004	+28	−10.5	...
CS 22956–081	+210	+244.6	...
CS 22957–022	+25	−31.6	4
CS 22957–024	−37	−67.4	...
CS 22957–026	+14	−18.9	...
CS 22957–036	−88	−154.5	...

REFERENCES. — (1) McWilliam et al. 1995a; (2) Bonifacio et al. 2009; (3) Depagne et al. 2002; (4) Lai et al. 2008

^a The RV listed in Column 3 is derived from the present study. In all cases this value agrees with previous investigations, referenced in Column 4, within 2 km s^{-1} .

some of these stars may be in binary or multiple star systems; however, caution is warranted regarding this conclusion. Several of the RV estimates reported in BPS92 deviate significantly from the RV measurements derived from high resolution spectroscopy. Stars whose RV estimate in BPS92 differs by more than 30 km s^{-1} from our high resolution RV measurements are listed in Table 4 and are not shown in Figure 2. Barring any misidentifications in the present survey, we attribute these discrepancies to irregularities of unknown origin that occurred during the course of the BPS92 survey. In light of this, we refrain from assigning a binary status classification to any star with only a single high resolution RV measurement, even if the star has a RV estimate from BPS92.

Finally, our observations reveal two new double-lined spectroscopic binary stars, CS 22884–033 and HE 2047–5612. We also reaffirm earlier work by Masseron et al. (2012) showing that the spectrum of CS 22949–008 exhibits two sets of lines. We present the observational data for these three stars in Table 2, but we omit them from the subsequent analysis.

5. EQUIVALENT WIDTHS

We measure equivalent widths (EWs) from our spectra using a semi-automatic routine that fits Voigt absorption line profiles to continuum-normalized spectra. This routine presents a plot of every fit to the user for final approval or modification. The local continuum is identified automatically by an iterative clipping procedure using a region of 3.5\AA on either side of the line of interest, but the user can identify a different continuum level for each line when necessary. Typically 7–11 points surrounding the line center are used for the fit, covering ~ 3 –4 times the Gaussian full width at half-maximum depth of the line for weak lines. For stronger lines with clearly visible wings and no obvious blending features, the number of fitting points is increased. We choose to fit Voigt profiles to the absorption lines to simultaneously account for the Gaussian core and the dispersion wings present in some stronger lines; for weak lines, the Voigt profile effectively resembles a Gaussian profile.

The complete list of 47,744 EW measurements for all stars analyzed is given in Table 5. Other lines fit by spectrum synthesis (9,268 lines) or used to derive upper limits

TABLE 5
SAMPLE TABLE OF EW MEASUREMENTS

Star	Wavelength (Å)	Species	E.P. (eV)	log <i>gf</i>	E.W. (mÅ) ^a
CS 22166-016	6707.80	Li I	0.00	0.17	limit
CS 22166-016	6300.30	[O I]	0.00	-9.78	...
CS 22166-016	7771.94	O I	9.14	0.37	...
CS 22166-016	7774.17	O I	9.14	0.22	...
CS 22166-016	7775.39	O I	9.14	0.00	...
CS 22166-016	4057.51	Mg I	4.35	-0.89	24.5
CS 22166-016	4167.27	Mg I	4.35	-0.71	39.4
CS 22166-016	4702.99	Mg I	4.33	-0.38	...
CS 22166-016	5172.68	Mg I	2.71	-0.45	180.1
CS 22166-016	5183.60	Mg I	2.72	-0.24	195.4
CS 22166-016	5528.40	Mg I	4.34	-0.50	58.8
CS 22166-016	5711.09	Mg I	4.34	-1.72	...
CS 22166-016	3943.99	Al I	0.00	-0.64	...
CS 22166-016	3961.52	Al I	0.01	-0.34	synth

NOTE. — The complete version of Table 5 is available online only. A short version is shown here to illustrate its form and content.

^a “Synth” indicates an abundance was derived from spectrum synthesis; “limit” indicates that an upper limit on the abundance was derived from the line.

(12,279 lines) are indicated using “synth” or “limit,” respectively. The complete version of Table 5 is available in the online edition of the journal, and only a sample is shown in the printed edition to demonstrate its form and content.

5.1. Comparison of Equivalent Widths Measured from Spectra Obtained with Different Spectrographs

We have deliberately observed a small number of bright stars with more than one instrument to check the reliability of the reduction processes at handling cosmic rays, scattered light, flat-fielding, etc. We have five stars in common to Magellan+MIKE and Smith+Tull, two stars in common to Magellan+MIKE and HET+HRS, and two stars in common to HET+HRS and Smith+Tull; one star, HD 122563, was observed with all three setups. In Figure 3 we compare the EWs measured from each of these spectra. The standard deviation of each set of comparisons is driven strongly by the S/N of the individual spectra. The largest deviations regularly arise from strong lines that suffer from blending and lower S/N in the blue. We find no evidence of differences in the spectra beyond the EW measurement uncertainties, typically 3–4 mÅ. It is reassuring that the spectra obtained with the different instruments are effectively interchangeable in the wavelength regions where they overlap with adequate S/N.

5.2. Comparison of Equivalent Widths with Those Measured by Other Investigators

Our sample has many stars in common with earlier studies by other investigators. Figure 4 compares EWs for 12 of the stars in common with the First Stars sample (Cayrel et al. 2004). For 1808 lines in common with $3700 < \lambda < 6500$ Å and $0 < \text{EW} < 220$ mÅ, we find a standard deviation (σ) of 4.7 mÅ and a very slight trend for the strongest lines ($\text{EW} \gtrsim 150$ mÅ), where our EW measurements are larger by ≈ 4 –5% on average. The weakest lines ($\text{EW} < 100$ mÅ) show very good agreement and have a smaller σ , 3.6 mÅ. This standard deviation is the same as found in comparisons of EWs measured by us using spectra from different instruments. No signif-

icant variations from these values are found when EWs from these 12 stars are considered on a star-by-star basis. Similar results are obtained when we compare our EWs with those of other investigators. Table 6 lists the standard deviation found when our EWs are compared with those of stars in common for six other studies. Table 6 also lists the slope and zeropoint of the linear regression (where 1.0 and 0.0 represent the slope and zeropoint for perfect agreement) and the mean offset. The slopes range from 0.88 to 0.97 with positive zeropoints; our EWs are systematically larger for the strongest lines. The mean offsets are negligible. The large standard deviation with respect to McWilliam et al. (1995a) is a result of the relatively low S/N of the spectra in that study (typical S/N of 30–45 pix^{-1}). For most other studies, σ for all lines is ≈ 4.0 –5.0 mÅ; when only weak lines are considered ($\text{EW} < 100$ mÅ), σ drops to ≈ 3.5 –4.0 mÅ.

To further investigate the nature of the discrepancy for the strong lines, we examine in detail 20 of the strongest lines commonly used for abundance analyses in the bright, metal-poor giant HD 128279 from a high S/N MIKE spectrum. Figure 5 compares our EW measurements for these lines with measurements made by fitting Voigt and Gaussian profiles in IRAF, by fitting a Voigt profile in SPECTRE (Fitzpatrick & Sneden 1987), and by direct integration in SPECTRE via Simpson’s rule. We find good agreement between the EW measurements from the Voigt profiles and by direct integration, even for the strongest lines with $\text{EW} > 250$ mÅ. Gaussian profiles clearly underestimate absorption in the wings of the strongest lines. Other investigations do account for extra absorption in the line wings, even if the formal Voigt profile is not explicitly invoked. We conclude that the small systematic difference for the strongest lines result from the different methods used to account for this extra absorption.

6. PHOTOMETRY

Optical and infrared broadband photometry is available for most stars in our sample, but these data are only used to calculate initial guesses for the stellar temperatures. Reddening values are taken from the Schlegel

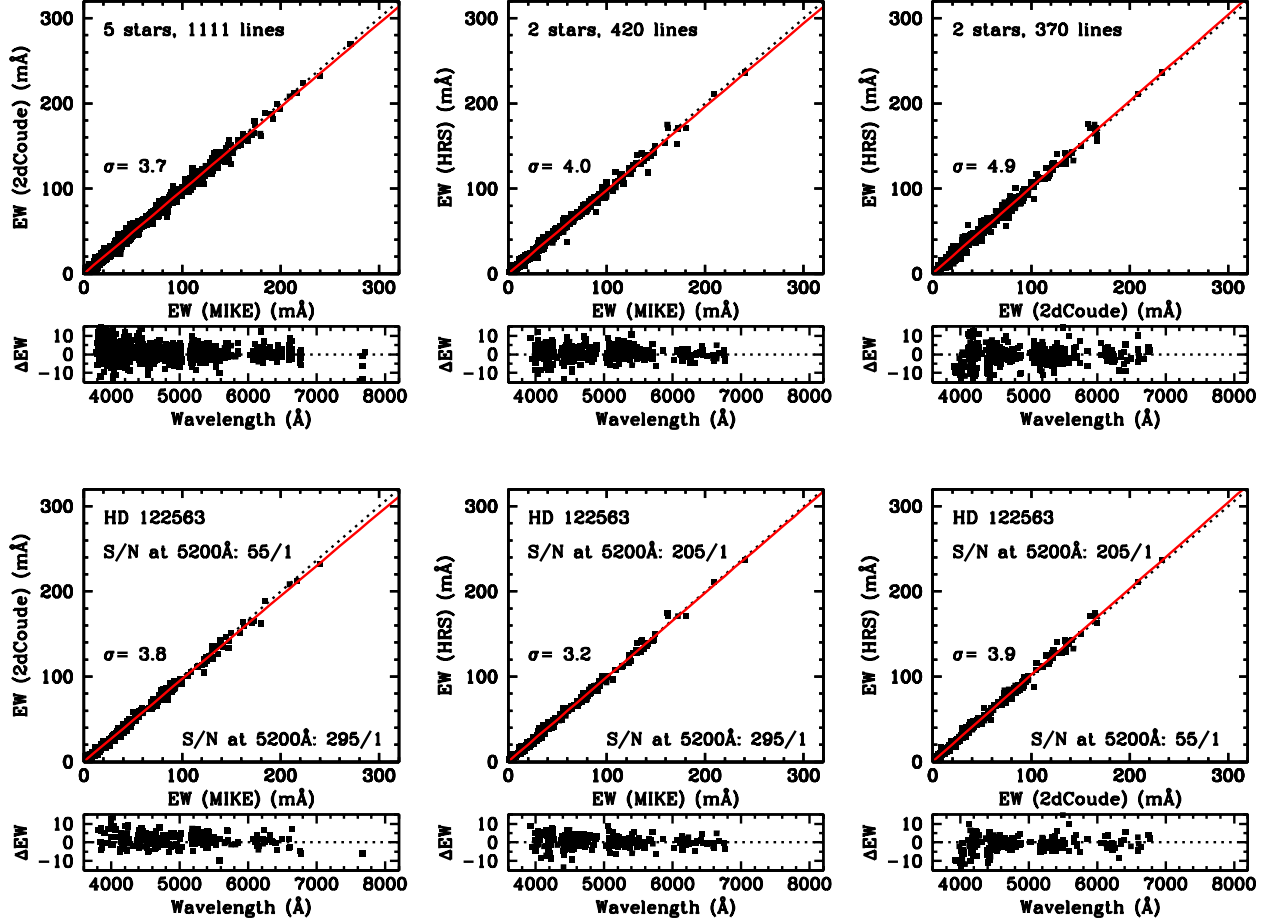


FIG. 3.— Comparison of EWs measured from spectra of the same stars obtained with different spectrographs. The 1:1 correlation is indicated as a dotted line, and the least-squares fit is indicated by the solid red line. The standard deviation (σ) is computed relative to the 1:1 correlation, not the least-squares fit. The top row of panels examines the combined measurement for stars observed with both the MIKE and Tull (“2dCoude”) spectrographs (HD 106373, HD 108317, HD 122563, HD 132475, and HE 1320–1339), MIKE and HRS (G015-010 and HD 122563), and the Tull and HRS (G025-024 and HD 122563). The bottom row of panels examines the measurements for one star observed with all three instruments, HD 122563.

TABLE 6
COMPARISON OF EQUIVALENT WIDTH MEASUREMENTS

Study	Line subset	N_{stars}	N_{lines}	slope	zeropoint	mean offset	σ (mÅ)
Carretta et al. (2002)	all lines	2	155	0.88	5.2	+2.3	7.0
	EW < 100 mÅ	2	123	0.88	5.2	+0.3	5.3
Cayrel et al. (2004)	all lines	12	1808	0.95	1.5	+1.8	4.7
	EW < 100 mÅ	12	1415	0.96	0.8	+0.7	3.6
Honda et al. (2004a)	bright targets						
	all lines	2	276	0.95	1.2	+1.7	3.7
	EW < 100 mÅ	2	231	0.95	1.2	+1.0	3.0
	faint targets						
all lines	2	176	0.85	7.0	+1.9	9.6	
EW < 100 mÅ	2	137	0.86	6.6	-0.9	7.2	
Ivans et al. (2003)	all lines	2	262	0.96	1.5	+0.3	4.2
	EW < 100 mÅ	2	241	0.94	1.8	+0.1	3.8
Johnson (2002)	all lines	3	763	0.93	1.3	+1.9	5.0
	EW < 100 mÅ	3	693	0.95	0.6	+1.3	3.4
Lai et al. (2008)	all lines	3	397	0.97	0.5	+1.3	4.2
	EW < 100 mÅ	3	355	0.97	0.4	+1.0	3.6
McWilliam et al. (1995a)	all lines	8	1350	0.93	5.1	-0.3	11.3
	EW < 100 mÅ	8	1033	0.94	4.7	-1.6	9.6

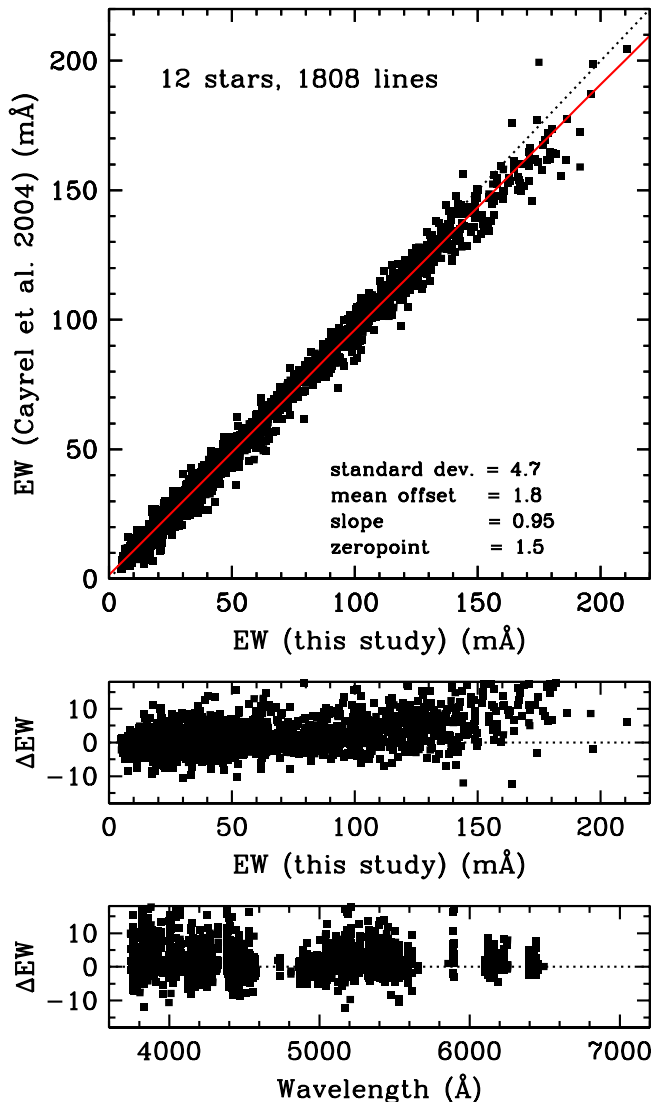


FIG. 4.— Comparison of EW measurements with those of Cayrel et al. (2004). The 1:1 correlation is indicated as a dotted line, and the least-squares fit is indicated by the solid red line in the top panel. The standard deviation is computed relative to the 1:1 correlation, not the least-squares fit. The differences are in the sense of this study *minus* Cayrel et al.

et al. (1998) maps, altered in the case of high reddening according to the prescription of Bonifacio et al. (2000). We adopt the extinction coefficients of Cardelli et al. (1989). We employ the Ramírez & Meléndez (2005) color transformations to place the Two Micron All Sky Survey (2MASS; Skrutskie et al. 2006) infrared photometry on the Telescopio Carlos Sánchez (TCS) scale of Alonso et al. (1999b). The optical photometry originates from many different sources, including Harris & Uggren (1964), Sandage (1969), Nicolet (1978), Carney (1979, 1983), Carney & Aaronson (1979), Bond (1980), Norris et al. (1985, 1999), Carney & Latham (1986), Sandage & Kowal (1986), Lazauskaite & Tautvaisiene (1990), Preston et al. (1991, 1994, 2006a), BPS92, Carney et al. (1994), Beers & Sommer-Larsen (1995), Beers et al. (2000, 2007), Schuster et al. (2004), Rossi et al. (2005), and Christlieb et al. (2008). The V magnitudes, adopted reddenings, and dereddened $B - V$ and $V - K$

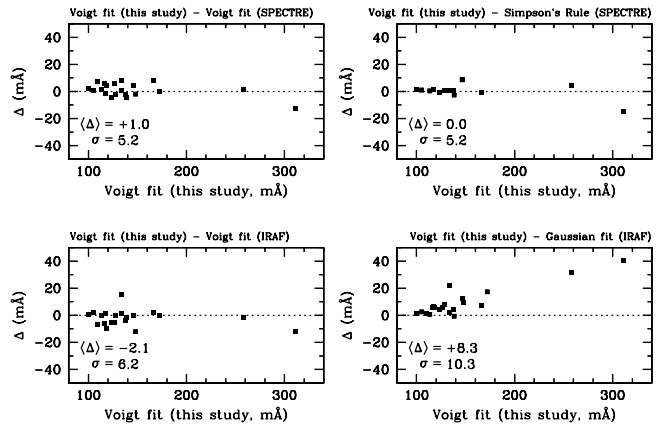


FIG. 5.— Comparison of EWs measured using various techniques and software packages in the high S/N spectrum of HD 128279. Only lines with $EW > 100$ mÅ are considered here. Note that only 13 of the 20 lines have been measured by Simpson’s rule due to weak blends in the wings of these lines. The dotted line indicates a difference of zero. The mean offset and standard deviation of the residuals are shown. The differences in the colors are listed in Table 17.

7. ATOMIC DATA

We start with a list of 474 lines to be considered for each star, but all lines are not observed, detected, and unblended in each star. This list is found in Table 7. The full version of Table 7 is available only in the online edition of the journal. This table includes the line wavelength, species identification, excitation potential (E.P.) of the lower level of the transition, $\log gf$ value, and references to the source for the $\log gf$ value. We perform spectral synthesis for lines broadened by hyperfine splitting (hfs) or in cases where a significant isotope shift (IS) may be present (see Section 9). The references for these data are also included in Table 7. When available, we use damping constants from Barklem et al. (2000) and Barklem & Aspelund-Johansson (2005). In all other cases we resort to the standard Unsöld (1955) approximation.

8. MODEL ATMOSPHERES

Numerous challenges in modeling stellar atmospheres persist, and they limit the accuracy of the derived abundances. These challenges include departures from local thermodynamic equilibrium (LTE) in the stellar atmosphere, time-dependent three-dimensional (3D) versus static one-dimensional (1D) representations of the atmosphere, inadequate treatment of convection, inclusion and proper calculation of all relevant sources of continuous opacity, and inaccurate or incomplete atomic and molecular data. Significant progress has been made to improve the situation in recent years, but it is still impractical to analyze large datasets except by means of the general procedures in common use for decades: namely, EW analysis or spectral synthesis of lines assuming 1D, plane-parallel, static model atmospheres in LTE throughout the line-forming layers. We make use of a recent set of MARCS models (Gustafsson et al. 2008), and we demonstrate in Section 8.2 that very similar results are obtained from the ATLAS9 grid (Castelli & Kurucz 2003).

8.1. Model Atmosphere Parameters

TABLE 7
ATOMIC DATA

λ (Å)	Species	E.P. (eV)	$\log gf$	Ref.
6707.80	Li I	0.00	+0.17	1
	CH $A^2\Delta - X^2\Pi$ G band			2
	NH $A^3\Pi - X^3\Sigma$ band			3
	CN $B^2\Sigma - X^2\Sigma$ band			3
6300.30	[O I]	0.00	-9.78	4
7771.94	O I	9.15	+0.37	4
7774.17	O I	9.15	+0.22	4
7775.39	O I	9.15	+0.00	4

REFERENCES. — (1) Smith et al. 1998; (2) B. Plez (2007, private communication); (3) Kurucz & Bell 1995; (4) Fuhr & Wiese 2009; (5) Chang & Tang 1990; (6) Aldenius et al. 2007; (7) Aldenius et al. 2009; (8) Lawler & Dakin 1989, using hfs from Kurucz & Bell 1995; (9) Lawler et al. 2013; (10) Wood et al. 2013; (11) Pickering et al. 2001, with corrections given in Pickering et al. 2002; (12) Doerr et al. 1985, using hfs from Kurucz & Bell 1995; (13) Biémont et al. 1989; (14) Sobek et al. 2007; (15) Nilsson et al. 2006; (16) Den Hartog et al. 2011 for both $\log(gf)$ value and hfs; (17) O’Brian et al. 1991; (18) Meléndez & Barbuy 2009; (19) Cardon et al. 1982, using hfs from Kurucz & Bell 1995; (20) Nitz et al. 1999, using hfs from Kurucz & Bell 1995; (21) Fuhr & Wiese 2009, using hfs from Kurucz & Bell 1995; (22) Roederer & Lawler 2012; (23) Biémont et al. 2011; (24) Ljung et al. 2006; (25) Nilsson et al. 2010; (26) Whaling & Brault 1988; (27) Palmeri et al. 2005; (28) Wickliffe et al. 1994; (29) Fuhr & Wiese 2009, using hfs/IS from McWilliam 1998 when available; (30) Lawler et al. 2001a, using hfs from Ivans et al. 2006; (31) Lawler et al. 2009; (32) Li et al. 2007, using hfs from Sneden et al. 2009; (33) Den Hartog et al. 2003, using hfs/IS from Roederer et al. 2008a when available; (34) Lawler et al. 2006, using hfs/IS from Roederer et al. 2008a when available; (35) Lawler et al. 2001b, using hfs/IS from Ivans et al. 2006; (36) Den Hartog et al. 2006; (37) Lawler et al. 2001c, using hfs from Lawler et al. 2001d; (38) Wickliffe et al. 2000; (39) Lawler et al. 2004 for both $\log(gf)$ value and hfs; (40) Lawler et al. 2008; (41) Wickliffe & Lawler 1997; (42) Sneden et al. 2009 for both $\log(gf)$ value and hfs/IS; (43) Lawler et al. 2007; (44) Ivarsson et al. 2003, using hfs/IS from Cowan et al. 2005; (45) Biémont et al. 2000, using hfs/IS from Roederer et al. 2012; (46) Nilsson et al. 2002.

NOTE. — The complete version of Table 7 is available online only. A short version is shown here to illustrate its form and content.

The inhomogeneous nature of the optical photometry (Section 6) leads us to adopt model atmosphere parameters that are primarily derived from our spectra. Effective temperatures (T_{eff}) are derived by requiring that abundances derived from Fe I lines show no trend with the E.P. of the lower level of the transition. In many stars the Fe I lines span a range of 0.0 to 4.5 eV, a far broader range than is available for any other species.

Microturbulence velocities (v_t) are derived by requiring that abundances derived from Fe I lines show no trend with line strength, expressed as the unitless quantity $\log(\text{EW}/\lambda)$. Lines with $\log(\text{EW}/\lambda) \gtrsim -5.0$ (e.g., $\text{EW} \gtrsim 40$ mÅ at $\lambda = 4000$ Å) are sensitive to v_t , and the sensitivity to v_t diminishes on the damping portion of the curve of growth, with $\log(\text{EW}/\lambda) \gtrsim -4.4$ (e.g., $\text{EW} > 160$ mÅ near 4000 Å). In many stars the strongest optical Fe I lines used have $\log(\text{EW}/\lambda) > -4.5$

($\text{EW} > 130$ mÅ near 4000 Å), which is on the saturated portion of the curve of growth in both dwarfs and giants. The weakest Fe I lines used often have $\log(\text{EW}/\lambda) < -6.0$ ($\text{EW} < 4$ mÅ near 4000 Å), but the weakest lines detected are a strong function of S/N.

Overionization is the name given to the effect that occurs when the local mean radiation intensity exceeds that predicted by the Planck source function, and overionization leads to a potentially significant underestimate of the number density of minority species. This non-LTE effect can lead to systematic underestimates of the Fe I number density when using the LTE approximation for the source function in metal-poor stars (e.g., Thévenin & Idiart 1999, Asplund 2005). To reduce the impact of this effect on the ionization balance between Fe I and Fe II, in most stars we derive surface gravities ($\log g$, in cgs units) from theoretical isochrones in the Y^2 grid (Demarque et al. 2004). For stars between the main sequence turnoff (MSTO) and the tip of the red giant branch, we interpolate the Y^2 isochrones in T_{eff} for the appropriate metallicity of each star. We assume an input age of 12 Gyr for all stars. Stars with ages 12.0 ± 1.5 Gyr were formed at redshifts $z > 2$, so this range includes the ages of most metal-poor Milky Way globular clusters (e.g., Dotter et al. 2010), the ages of individual halo stars as computed from radioactive decay of heavy elements (e.g., Roederer et al. 2009), and the redshifts of the rising inferred star formation rate density in galaxies that may grow to the size of the Milky Way (e.g., Bouwens et al. 2007). For stars on the horizontal branch (HB), below the isochrone inflection point (i.e., the main sequence; MS), or hotter than the MSTO, we derive surface gravities from the usual method of requiring the ionization balance between Fe I and Fe II. Uncertainties inherent to each of these methods are discussed below.

Fe II is the dominant ionization state, so overionization has little impact on the iron abundance derived from Fe II lines in stars of types F-G-K. We assume that the overall metallicity, $[\text{M}/\text{H}]$, is represented by the iron abundance derived from Fe II lines. The trade off, of course, is that the iron abundance derived from Fe II lines is more sensitive to the surface gravity of the model atmosphere than the iron abundance derived from Fe I lines.

We use the following procedure to converge to a final set of model parameters. Broadband photometry is used only to produce an initial estimate of T_{eff} from dereddened $V - K$ or $J - K$ colors and the Alonso et al. (1999b) color- T_{eff} relations. We have had to extrapolate the Alonso et al. calibrations to stars with $[\text{Fe}/\text{H}] < -3$ in our sample, but the metallicity sensitivity of such relations decreases with decreasing metallicity and these extrapolations are used for initial guesses only. Other relations, e.g., those of González Hernández & Bonifacio (2009), are calibrated directly to the 2MASS photometric system and are valid at $[\text{Fe}/\text{H}] < -3$. These relations are used less frequently in prior abundance surveys, so we adopt the Alonso et al. relations for the sake of comparison. We estimate the initial $\log g$ by interpolating (in $V - K$ or $J - K$) the appropriate Y^2 isochrones. We estimate the initial v_t from $\log g$ using the relation of Gratton et al. (1996). We compile metallicity estimates from many of the literature sources listed above, but they have relatively little impact on the initial estimates of the

other parameters.

We use a recent version (c. 2010) of the spectral line analysis code MOOG⁵ (Snedden 1973) to derive abundances of iron from Fe I and Fe II lines using our EW measurements and a MARCS model atmosphere interpolated for our initial model atmosphere parameters. We refine our initial T_{eff} , v_t , and $[\text{Fe}/\text{H}]$ estimates to enforce no trend of derived iron abundance (from Fe I) with each line’s E.P. or $\log(\text{EW}/\lambda)$ value, and we require that the input model metallicity agrees with the iron abundance derived from Fe II lines. We maintain $\log g$ fixed through these iterations. Then, for stars along the subgiant branch and red giant branch, the revised T_{eff} and $[\text{Fe}/\text{H}]$ estimates are used to refine $\log g$ from the isochrones. For stars on the HB, MS, or warmer than the MSTO, iron ionization equilibrium is enforced to derive $\log g$. Lines whose inferred abundance deviates by more than 2σ from the mean are discarded. We repeat this process until all four parameters converge, and this usually occurs within two to four iterations. We consider convergence to mean that the model atmosphere parameters are stable from one iteration to the next to the nearest 10 K in T_{eff} , 0.05 dex in $\log g$, 0.05 km s^{-1} in v_t , and 0.01 dex in metallicity. We perform this iteration scheme using a version of the batch mode capabilities of MOOG, and all steps are supervised by the user.

Table 17 lists the final T_{eff} , $\log g$, v_t , and $[\text{Fe}/\text{H}]$ for all 313 stars in the survey. Figure 6 illustrates these values. Different colors represent different metallicity ranges. The size of each point corresponds to the size of the microturbulence velocity parameter. Open circles represent stars whose gravity is derived from Fe ionization balance, while filled circles represent stars whose gravity is derived from the Y^2 grid of isochrones. This approach leads to the narrow width of the subgiant and red giant branches and the non-physical gap between the red giant branch and the HB. The latter effect is reminiscent of the difference between absolute magnitudes of field red giants and the fiducial of globular cluster M92 found in Figure 4 of Luck & Bond (1985). The bulk of the stars in our sample are subgiants (151 stars, denoted “SG” in Table 17) or red giants (98 stars, denoted “RG”). Smaller numbers of stars are on the HB (39 stars, denoted “HB”), MS (22 stars, denoted “MS”), or are warmer than the MSTO (3 stars, denoted “BS” in analogy with the blue straggler stars found in globular clusters).

8.2. Statistical Uncertainties

We use the statistical (internal) uncertainty in the derived Fe I and Fe II abundances (σ_{FeI} and σ_{FeII} , respectively) to assess the statistical uncertainties in the model parameters. We relate the sensitivity of T_{eff} and v_t to their correlation with E.P. and $\log(\text{EW}/\lambda)$ through the statistical uncertainty in σ_{FeI} . Our tests for several stars spanning the range of the SG and RG classes suggest that simple linear relations with T_{eff} and v_t are appropriate and lead to the relations $\sigma_{T_{\text{eff}}}^2 = (-0.17T_{\text{eff}} + 540)^2 \times \sigma_{\text{FeI}}^2$ and $\sigma_{v_t}^2 = (0.32v_t - 0.90)^2 \times \sigma_{\text{FeI}}^2$. For other stars in our sample we adopt relationships that are independent of T_{eff} and v_t . For stars on the MS, we find $\sigma_{T_{\text{eff}}}^2 =$

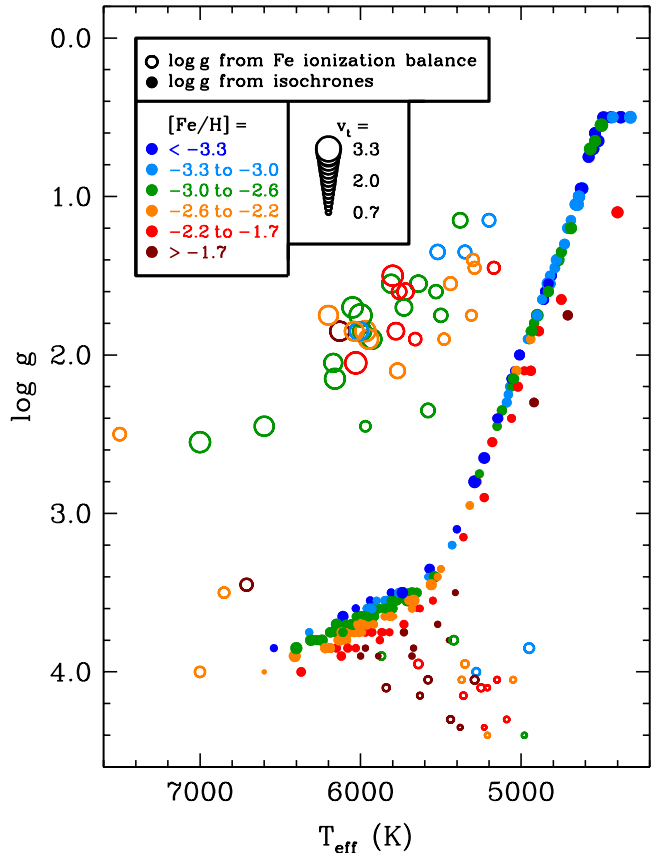


FIG. 6.— T_{eff} versus $\log g$ diagram for all 313 stars in our sample. Color-coding indicates the metallicity (from Fe II), and the point size indicates v_t . Open circles represent stars whose $\log g$ was derived from Fe ionization balance, and closed circles represent stars whose $\log g$ was calculated from isochrones. The “bend” observed for few stars at the top of the red giant branch is a result of encountering the edge of the grid of model atmospheres at $\log g = 0.5$ at low metallicity.

$(400\sigma_{\text{FeI}})^2$ and $\sigma_{v_t}^2 = (1.5\sigma_{\text{FeI}})^2$. For stars on the HB, we find $\sigma_{T_{\text{eff}}}^2 = (520\sigma_{\text{FeI}})^2$ and $\sigma_{v_t}^2 = (0.36\sigma_{\text{FeI}})^2$. For stars warmer than the MSTO (BS), we find $\sigma_{T_{\text{eff}}}^2 = (400\sigma_{\text{FeI}})^2$ and $\sigma_{v_t}^2 = (0.48\sigma_{\text{FeI}})^2$.

For stars in the SG and RG classes, we assess statistical uncertainties in $\log g$ by varying T_{eff} and $[\text{Fe}/\text{H}]$ as input parameters to the grid of Y^2 isochrones. In Figure 7 we illustrate the change in $\log g$ when T_{eff} is varied by ± 100 K. Stars along the giant branch are most sensitive because of its steep slope, with $\Delta \log g$ approaching 0.50 per 100 K, whereas stars in the SG class and near the MSTO show $\Delta \log g$ ranging from only 0.05 to 0.20 per 100 K. Figures 8 and 9 illustrate the change in $\log g$ when the isochrone age is varied by ± 1.5 Gyr, our assumed age uncertainty, or the input metallicity is varied by ± 0.10 dex. (Recall that we assume an age of 12 Gyr in the isochrones.) The gravity is most sensitive to age near the MSTO, whereas stars on the red giant branch have almost no age sensitivity in old stellar populations. The gravity is most sensitive to the isochrone metallicity in more metal-rich stars where line blanketing has a significant impact on the temperature and color. For most of the stars in our sample, the uncertainty in $\log g$ resulting

⁵ <http://www.as.utexas.edu/~chris/moog.html>

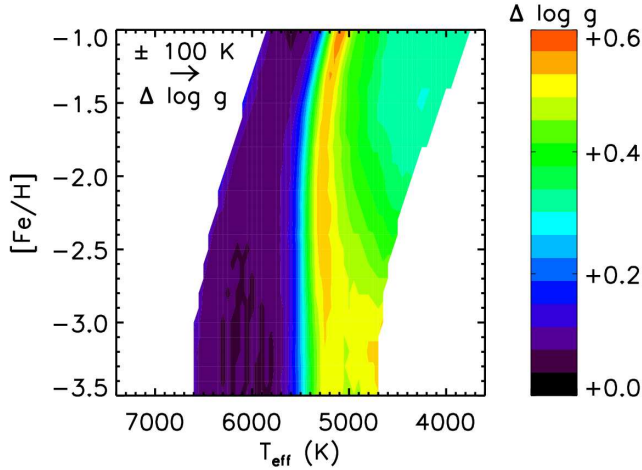


FIG. 7.— Variations in $\log g$ from the Y^2 grid of isochrones corresponding to uncertainties in T_{eff} . At given values of T_{eff} and $[\text{Fe}/\text{H}]$, the corresponding uncertainty in $\log g$ can be read off from the plot. The color bar on the right indicates the magnitude of the uncertainty in $\log g$ for a change in T_{eff} of 100 K.

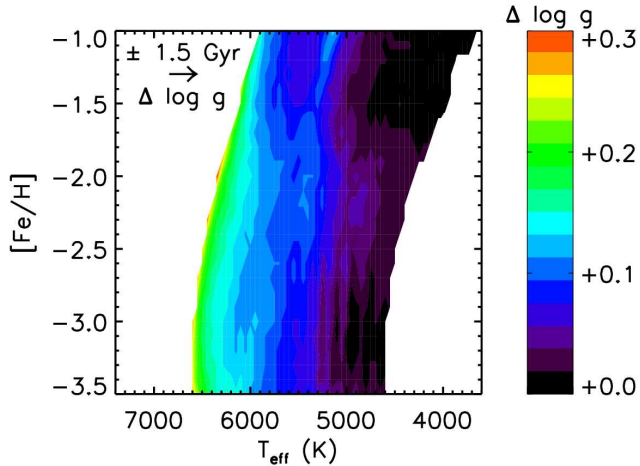


FIG. 8.— Variations in $\log g$ from the Y^2 grid of isochrones corresponding to uncertainties in age. At given values of T_{eff} and $[\text{Fe}/\text{H}]$, the corresponding uncertainty in $\log g$ can be read off from the plot. The color bar on the right indicates the magnitude of the uncertainty in $\log g$ if the isochrone age is varied by 1.5 Gyr (relative to the 12 Gyr isochrones).

from the uncertainty in metallicity is very small relative to other sources of uncertainty. For stars on the MS, HB, and warmer than the MSTO, we assess the statistical uncertainty in $\log g$ by varying the gravity such that the iron abundances derived from Fe I and Fe II remain in agreement within $\pm(\sigma_{\text{Fe I}}^2 + \sigma_{\text{Fe II}}^2)^{1/2}$. We consider statistical uncertainties in $[\text{M}/\text{H}]$ equal to the standard deviation of Fe I, since that species is used in deriving v_t , its uncertainties, and the cross terms discussed in Section 9.1. The statistical uncertainties in $\log g$ listed in Table 17 include the uncertainty from each of these factors. All statistical uncertainties include a “softening” factor to guard against unreasonably small uncertainties (10 K in T_{eff} ; 0.05 dex in $\log g$; 0.05 km s^{-1} in v_t ; and 0.02 dex in $[\text{M}/\text{H}]$).

To empirically test the sensitivity of the derived model

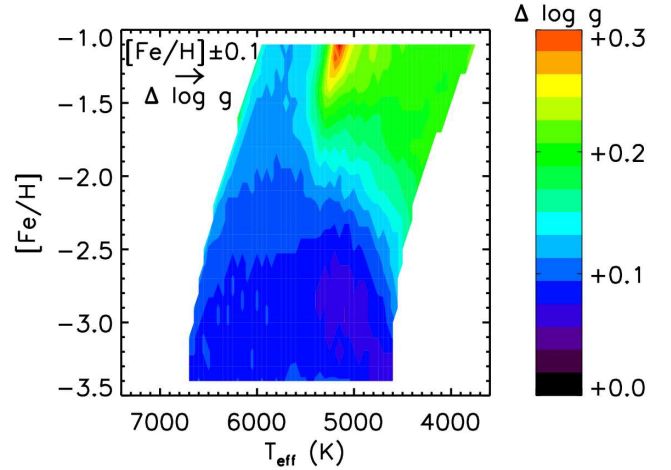


FIG. 9.— Variations in $\log g$ from the Y^2 grid of isochrones corresponding to uncertainties in metallicity. At given values of T_{eff} and $[\text{Fe}/\text{H}]$, the corresponding uncertainty in $\log g$ can be read off from the plot. The color bar on the right indicates the magnitude of the uncertainty in $\log g$ for a change in $[\text{Fe}/\text{H}]$ of 0.1 dex.

parameters to the choice of model grid, we select two subsets of stars from the full sample and rederive model parameters using the ATLAS9 grid of α -enhanced models with convective overshooting turned off. We begin the derivation from the original (unculled) set of EW measurements for each of these stars and follow the same set of procedures. One subset of stars is comprised of 32 subgiants with $5800 \leq T_{\text{eff}} \leq 6000$ K (as derived from the MARCS grid) and $-3.5 \leq [\text{Fe}/\text{H}] \leq -2.5$. The other subset is comprised of 22 giants with $4790 \leq T_{\text{eff}} \leq 5090$ K (as derived from the MARCS grid) and $-3.5 \leq [\text{Fe}/\text{H}] \leq -2.5$. The model parameters derived for the subset of subgiants are nearly identical, with $\Delta T_{\text{eff}} = -8$ K ($\sigma = 29$ K), $\Delta \log g = -0.005$ ($\sigma = 0.027$), $\Delta v_t = +0.002$ km s^{-1} ($\sigma = 0.039$ km s^{-1}), and $\Delta [\text{Fe}/\text{H}] = -0.006$ dex ($\sigma = 0.023$ dex). Differences are in the sense of MARCS minus ATLAS9. The model parameters derived for the subset of giants are similar but not identical, with $\Delta T_{\text{eff}} = +39$ K ($\sigma = 26$ K), $\Delta \log g = +0.11$ ($\sigma = 0.08$), $\Delta v_t = -0.07$ km s^{-1} ($\sigma = 0.03$ km s^{-1}), and $\Delta [\text{Fe}/\text{H}] = +0.04$ dex ($\sigma = 0.03$ dex). Thus, the ATLAS9 grid tends to move stars slightly up the red giant branch to cooler temperatures, lower gravities, higher microturbulence velocities, and lower metallicities. Fortunately, the magnitude of the effect is rather small. The standard deviations derived in each of these tests also provide an estimate of the dispersion in model parameters that could be expected in the convergence routine. These uncertainties are comparable to the size of the statistical uncertainties. We include a model convergence uncertainty of 30 K in T_{eff} , 0.08 dex in $\log g$, and 0.04 km s^{-1} in v_t in the statistical uncertainties listed in Table 17.

8.3. Comparison with Previous Surveys

We compare our model atmosphere parameters with those determined by studies from the last 30 years that analyzed at least six stars in common with us: Luck & Bond (1985), McWilliam et al. (1995b), Ryan et al. (1996), Fulbright (2000), Johnson (2002), Stephens & Boesgaard (2002), Gratton et al. (2003), Cayrel et al.

TABLE 8
COMPARISON OF ATMOSPHERIC PARAMETERS WITH PREVIOUS SURVEYS

Comparison	N	$\Delta T_{\text{eff}} (\sigma)$ (K)	$\Delta \log g (\sigma)$	$\Delta v_t (\sigma)$ (km s ⁻¹)	$\Delta \text{Fe II} (\sigma)$
Luck & Bond (1985) ^b	11	-169 (140)	-0.17 (0.44)	-0.57 (0.46)	-0.49 (0.18)
McWilliam et al. (1995b) ^a	26	-174 (117)	-0.44 (0.50)	-0.56 (0.26)	-0.25 (0.15)
Ryan et al. (1996) ^a	10	-233 (203)	-0.82 (0.41)	-0.22 (0.41)	-0.38 (0.20)
Fulbright (2000) ^b	17	-43 (140)	-0.33 (0.33)	-0.08 (0.28)	-0.14 (0.12)
Johnson (2002) ^b	6	+12 (45)	-0.12 (0.26)	-0.27 (0.28)	-0.16 (0.06)
Stephens & Boesgaard (2002) ^b	6	-44 (218)	-0.17 (0.16)	+0.18 (0.37)	-0.01 (0.19)
Gratton et al. (2003) ^a	6	-210 (98)	-0.41 (0.24)	+0.00 (0.22)	-0.10 (0.15)
Cayrel et al. (2004) ^a	18	-236 (104)	-0.68 (0.41)	-0.22 (0.14)	-0.20 (0.13)
Honda et al. (2004b) ^a	10	-192 (130)	-0.76 (0.29)	-0.20 (0.31)	-0.31 (0.23)
Simmerer et al. (2004) ^a	19	-82 (155)	-0.47 (0.35)	-0.29 (0.43)	-0.22 (0.17)
Preston et al. (2006a) ^b	19	-58 (124)	-0.59 (0.28)	-0.02 (0.27)	-0.15 (0.12)
Lai et al. (2008) ^a	12	-233 (204)	-0.50 (0.39)	-0.10 (0.08)	-0.08 (0.18)
Bonifacio et al. (2009) ^a	9	-184 (198)	-0.56 (0.43)	+0.07 (0.30)	-0.09 (0.13)
Ishigaki et al. (2010) ^b	10	+86 (164)	-0.13 (0.31)	+0.00 (0.35)	+0.00 (0.20)
Roederer et al. (2010) ^b	11	+75 (163)	+0.24 (0.35)	-0.04 (0.14)	+0.10 (0.16)
All Stars					
All	190	-118 (175)	-0.43 (0.44)	-0.20 (0.36)	-0.18 (0.20)
Group (a)	110	-185 (154)	-0.57 (0.42)	-0.26 (0.35)	-0.21 (0.18)
Group (b)	80	-28 (161)	-0.24 (0.41)	-0.11 (0.36)	-0.13 (0.22)
Stars in class "RG"					
All	108	-154 (160)	-0.48 (0.49)	-0.30 (0.35)	-0.25 (0.20)
Group (a)	73	-215 (125)	-0.65 (0.43)	-0.33 (0.31)	-0.27 (0.17)
Group (b)	35	-27 (151)	-0.13 (0.40)	-0.23 (0.41)	-0.21 (0.24)
Stars in class "SG"					
All	40	-94 (211)	-0.30 (0.37)	-0.04 (0.38)	-0.04 (0.18)
Group (a)	24	-144 (199)	-0.41 (0.36)	-0.08 (0.41)	-0.06 (0.15)
Group (b)	16	-18 (211)	-0.14 (0.34)	+0.01 (0.33)	+0.01 (0.22)
Stars in class "HB"					
All	28	-7 (160)	-0.47 (0.42)	-0.11 (0.31)	-0.12 (0.17)
Group (a)	5	+44 (189)	-0.52 (0.47)	-0.38 (0.37)	-0.17 (0.18)
Group (b)	23	-19 (156)	-0.46 (0.42)	-0.05 (0.26)	-0.10 (0.16)
Stars in class "MS"					
All	14	-138 (99)	-0.30 (0.19)	-0.05 (0.25)	-0.15 (0.08)
Group (a)	8	-172 (108)	-0.29 (0.21)	-0.09 (0.22)	-0.14 (0.10)
Group (b)	6	-92 (71)	-0.31 (0.16)	+0.01 (0.30)	-0.15 (0.07)

NOTE. — Differences are in the sense of this study minus other study. Quantities in parenthesis refer to the standard deviation.

^a Studies that do not use Fe I abundance versus E.P. as the primary means of determining T_{eff}

^b Studies that use Fe I abundance versus E.P. as the primary means of determining T_{eff}

(2004), Honda et al. (2004b), Preston et al. (2006a), Lai et al. (2008), Bonifacio et al. (2009), Ishigaki et al. (2010), and Roederer et al. (2010). These studies can be divided into two general categories based on the primary means by which T_{eff} has been determined. One group (group “b” in Table 8) uses the usual spectroscopic technique of determining T_{eff} by minimizing the dependence of Fe I abundance with E.P., as we have done. The other group (group “a” in Table 8) relies on color– T_{eff} relations or fits to the wings of Balmer series lines to calculate T_{eff} . Some of these studies use a hybrid of these techniques, and we have made our best attempt to divide them into one of the two categories for purposes of this comparison.

The differences and standard deviations in T_{eff} , $\log g$, v_t , and metallicity (expressed as $[\text{Fe II}/\text{H}]$; i.e., the iron abundance as derived from Fe II lines) are listed in Table 8 and illustrated in Figure 10. As has long been known (e.g., Luck & Bond 1985), photometric T_{eff} determinations consistently predict warmer temperatures and higher gravities than purely spectroscopic T_{eff} predictions. The values listed in Table 8 reaffirm this situation.

There are no significant temperature differences between our study and previous ones that used the abun-

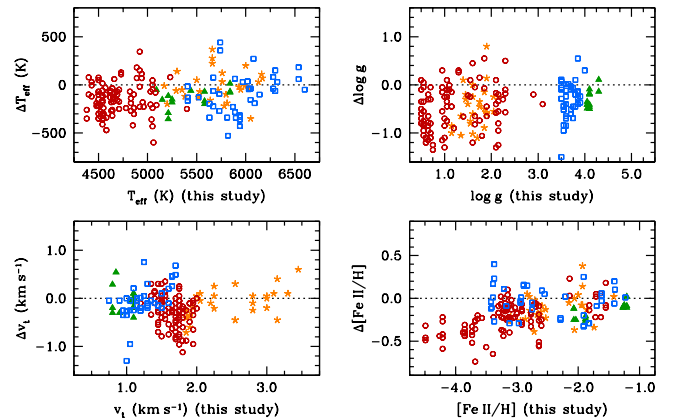


FIG. 10.— Comparison of model atmosphere parameters and derived metallicities between our study and previous work. All differences are in the sense of “this study” minus “previous.” Different evolutionary states are illustrated by different point symbols: open red circles mark stars in class RG, open blue squares mark stars in class SG, orange starred symbols mark stars in class HB, and filled green triangles mark stars in class MS. The dotted lines indicate a difference of zero.

dance versus E.P. approach, with a mean $\Delta T_{\text{eff}} = -28$ K ($\sigma = 161$ K) from 80 stars. Differences in the gravities ($\Delta \log g = -0.24$, $\sigma = 0.41$), microturbulence parameters ($\Delta v_t = -0.11$ km s $^{-1}$, $\sigma = 0.36$ km s $^{-1}$), and derived metallicities ($\Delta [\text{Fe}/\text{H}] = -0.13$, $\sigma = 0.22$ dex) are negative but not statistically significant. These offsets show only slight variations if the stellar evolutionary status is considered.

We find significant differences in the derived stellar parameters when we compare with studies that compute T_{eff} by other methods. For the 110 stars in common, our temperatures are cooler ($\Delta T_{\text{eff}} = -185$ K, $\sigma = 154$ K), our gravities are lower ($\Delta \log g = -0.57$, $\sigma = 0.42$), and our microturbulence parameters are smaller ($\Delta v_t = -0.26$ km s $^{-1}$, $\sigma = 0.35$ km s $^{-1}$). These offsets conspire to lower our derived mean metallicities by 0.21 dex ($\sigma = 0.18$ dex). These offsets show some dependence on evolutionary state. The most pronounced offsets are in red giants, where our mean metallicities are lower by 0.27 dex ($\sigma = 0.17$ dex). Except for v_t , these differences are moderately significant.

Given the present state of modeling of the line-forming regions of stellar atmospheres, it is unclear whether one approach is preferable to another. Both are likely inadequate at some level. Abundance studies often adopt a technique based on the information available about the stellar sample or the quality of the spectra themselves (reliable photometry, knowledge of stellar distance, interstellar reddening, spectral coverage, etc.). Most studies of stars with $[\text{Fe}/\text{H}] < -2.5$ selected from BPS92 have adopted temperatures calculated from color- T_{eff} relations or Balmer line profiles (e.g., McWilliam et al. 1995b, Ryan et al. 1996, Cayrel et al. 2004, Lai et al. 2008, Bonifacio et al. 2009), and so on average our derived metallicities will always be lower than theirs. Nevertheless, despite these differences, Figure 10 demonstrates that the *relative* metallicities are in good agreement for all but the most metal-poor giants. We discuss this point in more detail in Section 8.5.

Lind et al. (2012) have considered how line-by-line departures from LTE on Fe I and Fe II lines can act to influence the derivation of stellar parameters. For all parameter ranges included in our sample, and for the choice of the hydrogen collision parameter adopted by Lind et al., their study finds that LTE calculations of the Fe II abundance reflect that of non-LTE calculations to within 0.02 dex. This principle underlies our decision to adopt the iron abundance derived from Fe II lines as our metallicity indicator. For the metallicity range of our sample, Lind et al. also suggest that temperatures derived by our method will underestimate T_{eff} by less than 30 K for red giants, overestimate T_{eff} by less than 30 K for stars on the subgiant branch and main sequence turn-off, overestimate T_{eff} by 40–120 K for stars on the horizontal branch, and overestimate T_{eff} by less than 20 K for stars on the main sequence. In summary, it seems unlikely that departures from LTE alone can account for the differences between the photometric and spectroscopic temperatures estimated for our stellar sample.

As illustrated in Figure 11, our derived v_t values for the most luminous giants are slightly lower than our initial guesses calculated from the relation given by Gratton et al. (1996). The Gratton et al. relation is shown by the

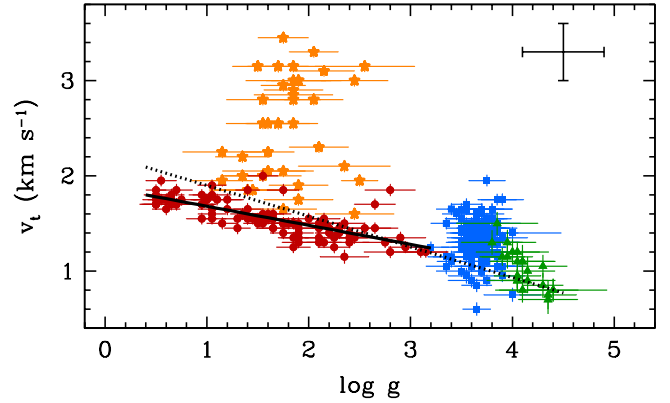


FIG. 11.— Relationship between $\log g$ and v_t . Different evolutionary states are illustrated by different point symbols: red circles mark stars in class RG, blue squares mark stars in class SG, orange starred symbols mark stars in class HB, and green triangles mark stars in class MS. The solid line represents the relationship defined by the RG stars in our sample. The dotted line represents the relationship found by Gratton et al. (1996). Statistical uncertainties are shown on the points, and the black cross in the upper right corner illustrates a typical systematic uncertainty.

dotted line. The solid line shows a linear least-squares fit to the giants in our sample, given by $v_t = -0.20 \log g + 1.88$ ($\sigma = 0.13$). For less luminous giants, the two relations agree well. Despite the shallower slope, $\log g$ and v_t show a tight correlation for the giants in our sample. The difference for the most luminous giants can be attributed mostly to the lower $\log g$ values derived by our methods. Shifting the $\log g$ values for our RG stars an average of 0.65 dex to the right (Table 8, group “a”) would bring the v_t values for the two relations into better agreement overall. No significant relationship appears between $\log g$ and v_t for the stars in our SG, MS, or HB classes.

The standard deviations reported in Table 8 are considerably larger than the statistical uncertainties reported in Table 17, and the difference is likely due to systematic effects. By definition, these are not included in the statistical error budget. Zero-point differences in $[\text{Fe}/\text{H}]$ are generally insignificant considering the magnitude of the dispersions. We address the source of the remaining zero-point differences in Section 8.4, and systematic uncertainties are discussed in Section 8.5.

8.4. The Impact of EW Measurements, Line Lists, Model Grids, and Analysis Codes

We assess the impact that the EW measurements, line list, $\log gf$ values, and general machinery (i.e., grid of model atmospheres and line analysis software) have on the derived metallicities when compared with previous work. To do this, we rederive iron abundances for stars in common with other studies using published EW measurements, line lists, and model atmosphere parameters. Five recent sets of studies have several stars in common with us: Johnson (2002), the “OZ” project (Carretta et al. 2002; Cohen et al. 2006, 2008), the First Stars project (including Cayrel et al. 2004, Spite et al. 2005, François et al. 2007, and others), Honda et al. (2004a,b), and Lai et al. (2008).

The results of several comparisons are listed in Table 9. In comparison “A,” we rederive the iron abundances using published EW measurements, line lists, and model atmosphere parameters from another study, but we use

TABLE 9
COMPARISON OF DERIVED IRON ABUNDANCES USING DIFFERENT EQUIVALENT WIDTHS, LINE
LISTS, AND ANALYSIS TOOLS

Abundance ratio	No. stars in common	$\Delta (\sigma)$ “A”	$\Delta (\sigma)$ “B”	$\Delta (\sigma)$ “C”	$\Delta (\sigma)$ “C”–“A”
Johnson (2002)					
[Fe I/H]	7	-0.114 (0.021)	-0.054 (0.039)	-0.067 (0.032)	+0.047 (0.031)
[Fe II/H]	7	-0.064 (0.028)	-0.063 (0.032)	-0.010 (0.034)	+0.054 (0.034)
OZ: Carretta et al. (2002); Cohen et al. (2006, 2008)					
[Fe I/H]	5	-0.154 (0.055)	+0.066 (0.046)	-0.214 (0.051)	-0.060 (0.070)
[Fe II/H]	5	-0.066 (0.055)	-0.142 (0.207)	+0.042 (0.156)	+0.108 (0.172)
First Stars: Cayrel et al. (2004)					
[Fe I/H]	18	-0.027 (0.008)	+0.016 (0.039)	-0.032 (0.046)	-0.005 (0.046)
[Fe II/H]	18	-0.004 (0.033)	-0.058 (0.068)	+0.039 (0.064)	+0.043 (0.017)
Honda et al. (2004a,b)					
[Fe I/H]	10	-0.260 (0.021)	-0.037 (0.078)	-0.189 (0.090)	+0.071 (0.082)
[Fe II/H]
Lai et al. (2008)					
[Fe I/H]	12	-0.007 (0.016)	+0.022 (0.025)	-0.029 (0.025)	-0.023 (0.023)
[Fe II/H]	12	-0.008 (0.017)	-0.139 (0.075)	+0.125 (0.091)	+0.133 (0.083)

NOTE. — Comparison “A” derives the iron abundances using published EWs and model parameters from the other study and our machinery. Comparison “B” derives the iron abundances using published EWs from the other study, our derived model parameters, and our machinery. Comparison “C” derives the iron abundances using EWs measured by us, stellar parameters derived by the other study, and our machinery. Comparison “C”–“A” is the difference in iron abundances when only the EWs and linelists change. Differences are in the sense of “as derived here” minus “published.” Quantities in parenthesis refer to the standard deviation.

the ATLAS9 grid of model atmospheres and MOOG to perform the calculations. We may think of comparison “A” as representing the differences in [Fe/H] we would have derived if we had used the EW measurements, line lists, and temperature/gravity scales of other studies. In comparison “B,” we rederive the iron abundances using the published EW measurements and line lists from other studies, our grid of MARCS models, and MOOG. We may think of comparison “B” as representing the differences in [Fe/H] we would have derived if we had adopted other EW measurements and line lists for our analysis. In comparison “C,” we rederive the iron abundances using our EW measurements and line list, the model atmosphere parameters from other studies, the ATLAS9 model grid, and MOOG. We may think of comparison “C” as representing the differences in [Fe/H] that would have been derived by other studies using our EW measurements and line list.

The final column in Table 9 (“C”–“A”) lists the differences in derived iron abundances when using stellar parameters from other studies if only the EW measurements and line list are changed. We calculate that the $\log gf$ values for Fe I and Fe II lines in common are different by < 0.03 dex on average. Thus any residual differences in the final column in Table 9 are the result of which lines are actually used in the analysis.

These comparisons are imperfect. For example, some of these other studies used Turbospectrum, SPTOOL, or employed earlier versions of MOOG that did not include Rayleigh scattering in the source function. When appropriate, we have reverted to the earlier version of MOOG when making these calculations for comparison. The OSMARCS and earlier ATLAS grids of model atmospheres were used in some other studies, and the interpolation codes for the ATLAS9 grid are also different. The adopted solar iron abundance varies from $\log \epsilon (\text{Fe}) = 7.50$ to 7.52 among these studies, and the

scaled solar compositions adopted vary from one model grid to another. Finally, we simply adopt published model atmosphere parameters without rederiving them from scratch before determining the iron abundances.

Nevertheless, Table 9 indicates that the differences in the iron abundances are often small or not significant. It is beyond the scope of the present study to identify the source of the remaining discrepancies. Using the comparison with the First Stars sample as an example, we conclude based on comparison “A” that our analysis would have derived Fe I abundances lower by 0.027 dex using their methods. The differences in the EW measurements and lines used for analysis are negligible, as demonstrated by comparisons “B,” “C,” “C”–“A,” and Figure 4. These comparisons should give some guidance to investigators attempting to place our study in the context of others.

8.5. Systematic Uncertainties

The true magnitude of systematic uncertainties is more difficult to quantify. The scatter observed when comparing our model parameters to those in previous studies of stars in common may give some guidance here. For stars in the evolutionary classes RG/SG/HB/MS, when comparing with studies where model parameters were derived by similar techniques, these comparisons yield standard deviations of 151/211/156/71 K in T_{eff} , 0.40/0.34/0.42/0.16 in $\log g$, 0.41/0.33/0.26/0.30 km s^{-1} in v_t , and 0.24/0.22/0.16/0.07 dex in [Fe II/H]. In most cases these uncertainties dominate the statistical uncertainties.

We may further investigate the scale of systematic uncertainties by comparing our model parameters with those derived by alternative techniques. We compare our spectroscopically-derived temperatures with ones derived from color– T_{eff} relations (hereafter “photometric” temperatures). We compute photometric temperatures

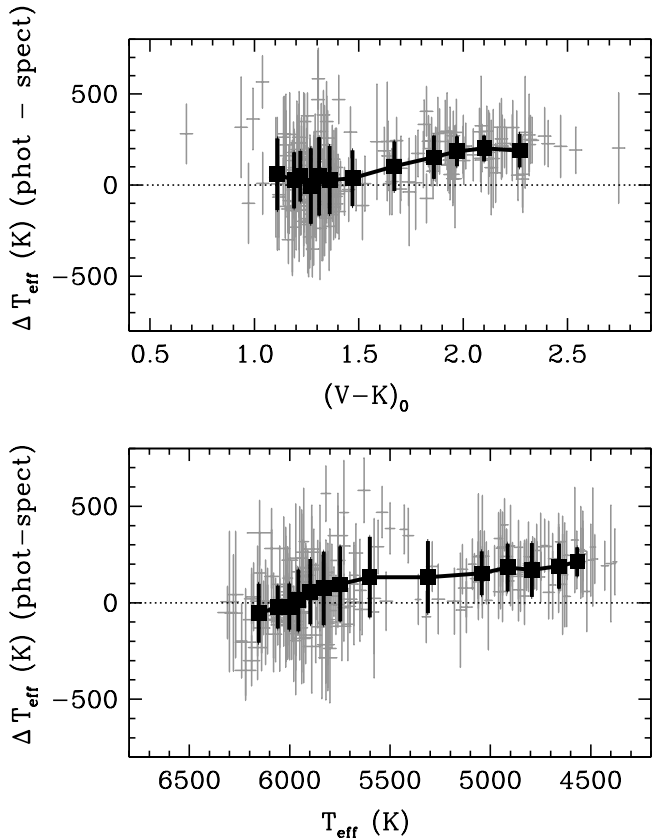


FIG. 12.— Difference in photometric and spectroscopic T_{eff} as a function of $(V - K)_0$ (top) and spectroscopic T_{eff} (bottom). The photometric T_{eff} values are predicted from the Alonso et al. (1999b) ($J - H$) and ($J - K$) relations, using the methods described in Section 6. Stars with discrepant photometry are ignored. Only stars evolved beyond the MSTO but not yet on the HB are shown. Gray crosses indicate individual stars, and the large black points mark the weighted average and standard deviation computed by passing a box of 30 stars with an overlap of 15 stars through the data. The dotted line indicates a difference of zero.

from the $J - H$ and $J - K$ relations of Alonso et al. (1999b). This is illustrated in Figure 12, where we show the difference in photometric and spectroscopic temperature for 219 stars in our sample. There is a large amount of scatter at any given temperature, but there is a significant offset (approaching 200 K on average) for stars cooler than ~ 5100 K and $(V - K)_0 > 1.8$. This finding echoes that of many previous studies, including Johnson (2002), Cayrel et al. (2004), Aoki et al. (2007), Cohen et al. (2008), and Lai et al. (2008). The underlying physical cause of this discrepancy is not fully understood, but it likely stems at least in part from the inability of one-dimensional hydrostatic LTE model atmospheres to capture the essential physics of convection, radiative transfer, and so on. This naturally affects the predicted colors and line formation. Frebel et al. (2013) discuss this issue at length and propose an empirical calibration based on seven well-studied nearby stars to bring the two scales into agreement. The relationship between the T_{eff} differences and T_{eff} shown in their Figure 2 agrees nearly perfectly with the mean offsets shown in our Figure 10. Frebel et al. also note that the discrepancy between the two scales becomes even more exaggerated for stars with $[\text{Fe}/\text{H}] < -3.5$. We see a similar outcome: for the 27 stars

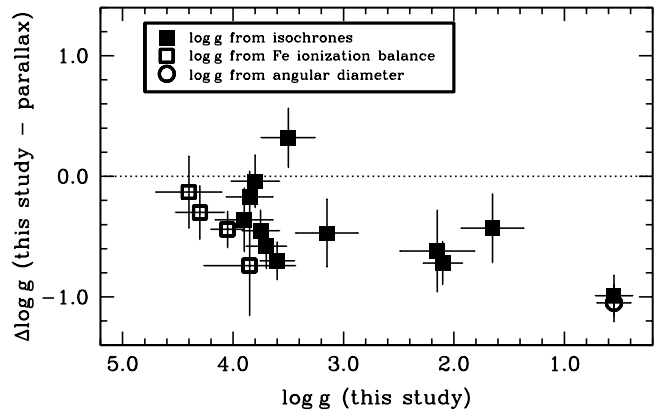


FIG. 13.— Comparison of $\log g$ derived in this study with those computed from Hipparcos parallaxes. Only the 16 stars with $E(B - V) < 0.12$ and Hipparcos uncertainties smaller than 20% are considered. The fill and shape of the points indicates the method by which the $\log g$ was obtained. For display purposes, the difference in the “angular diameter” measurement is plotted alongside the “parallax” measurements, but these are really two separate methods to derive $\log g$. The dotted line indicates a difference of zero.

(counting repeat analyses) with $[\text{Fe}/\text{H}] < -3.5$ in common between our sample and previous ones (Figure 10), our T_{eff} values are lower by 323 K ($\sigma = 90$ K) on average. This demonstrates that the cooler temperature scale in our study relative to previous studies that used color- T_{eff} relations is a consequence to the method used to derive T_{eff} , as discussed previously in Section 8.3.

For a few nearby stars, we compare our gravities with those calculated from parallaxes measured by the Hipparcos mission (Perryman 1997), using the data from the reduction by van Leeuwen (2007). We restrict this comparison to stars with Hipparcos parallax precisions better than 20% and $E(B - V) < 0.12$; only 16 stars in our sample meet these criteria. Using the parallax, apparent magnitude, reddening, bolometric corrections (BC; Alonso et al. 1999a), temperature, metallicity, mass (assumed to be $0.8 M_{\odot}$), and the solar constants $M_{\text{bol},\odot} = 4.74$, $T_{\text{eff},\odot} = 5780$ K, and $\log g_{\odot} = 4.44$, we can calculate $\log g$ by means of the relation

$$\log g = 0.4(M_{K,\star} + BC_K - M_{\text{bol},\odot}) + \log g_{\odot} + 4 \log(T_{\text{eff},\star}/T_{\text{eff},\odot}) + \log(m_{\star}/m_{\odot}). \quad (1)$$

Figure 13 compares these “physical” $\log g$ values with our derived $\log g$ values for these 16 stars. We also compare our gravity for HD 122563 with that derived from the recent measurement of its angular diameter by Creevey et al. (2012). Our $\log g$ values are systematically lower than the physical ones by 0.49 dex ($\sigma = 0.32$ dex), independent of the method we have used to derive $\log g$. This offset is similar to that found (-0.57 , $\sigma = 0.42$) when comparing our $\log g$ values with those calculated from color- T_{eff} relations by other investigators (Section 8.3).

We use the T_{eff} predicted by $(V - K)_0$ instead of a spectroscopically-derived T_{eff} as an alternative method to calculate $\log g$ from isochrones. For the 11 stars to which we can apply both the parallax method and the isochrone method, the photometric temperatures give $\log g$ values greater by only 0.15 dex than the physical ones. This would be encouraging if not for the fact that the dispersion in $\log g$ for the photometric T_{eff} input is

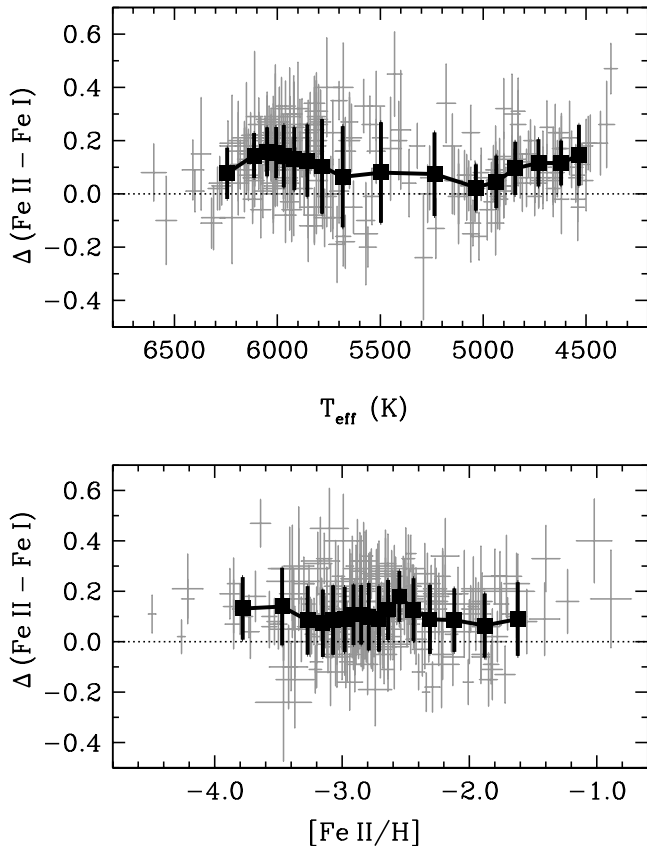


FIG. 14.— Difference in iron abundance derived from Fe II and Fe I as a function of T_{eff} and $[\text{Fe II}/\text{H}]$. Only stars in the SG and RG classes are shown. Gray crosses indicate individual stars, and the large black points mark the weighted average and standard deviation computed by passing a box of 30 stars with an overlap of 15 stars through the data. The dotted line indicates a difference of zero.

substantially larger ($\sigma = 0.63$ dex) than that using the spectroscopic T_{eff} input ($\sigma = 0.36$ dex).

Figure 14 shows the difference in the derived iron abundances using Fe II or Fe I lines. Differences are mostly found in the range $-0.1 < [\text{Fe II}/\text{Fe I}] < +0.3$ dex, with a mean difference of 0.10 dex ($\sigma = 0.13$ dex). These differences do not show a strong dependence on metallicity, but they are slightly larger for the warmest (≈ 6100 K) and coolest (≈ 4600 K) stars in the sample. The differences are comparable to what is expected if overionization of Fe I is responsible (e.g., Thévenin & Idiart 1999).

We suggest that the statistical uncertainties, listed in Table 17, should be considered when comparing abundance ratios of stars with similar parameters. The total uncertainties, which are more difficult to assess, should be used when absolute abundances are considered. The values listed at the beginning of this section may be considered representative of the total uncertainties.

8.6. The Impact of $\log g$ on Metallicity

Our $\log g$ values are systematically lower than those implied by several other derivation methods. As demonstrated in Section 9.1, ionized species are more sensitive to $\log g$ than neutral species are. Our metallicities are based on the iron abundance derived from Fe II lines, so this difference does have an impact.

Tables 8 and 9 can be used to quantify this impact on the iron abundances. Two of the sets of comparisons listed, the 0Z studies and the Lai et al. (2008) study, calculated photometric T_{eff} values and used these to calculate $\log g$ from isochrones. Their values of T_{eff} and $\log g$ are equivalent to what we would have calculated using this approach. Note that the 0Z set of studies listed in Table 9 did not have enough stars in common to merit inclusion in Table 8, so we perform an identical comparison separately and list the results here. For the five stars in common, the mean differences are -227 K ($\sigma = 169$ K) in T_{eff} , -0.48 dex ($\sigma = 0.42$ dex) in $\log g$, -0.55 km s^{-1} ($\sigma = 0.22$ km s^{-1}) in v_t , and -0.15 dex ($\sigma = 0.22$ dex) in $[\text{Fe II}/\text{H}]$.

These results suggest that our metallicities are lower by 0.15 dex (0Z) or 0.08 dex (Lai et al. 2008) in a straight-up comparison. Comparison “C” in Table 9 lists the $[\text{Fe I}/\text{H}]$ and $[\text{Fe II}/\text{H}]$ abundances that we would have derived for our sample using others’ photometric T_{eff} and $\log g$ values with our EW measurements, linelist, model grid, and MOOG. These corrections must be applied to the values above. Thus, we conclude that our metallicities are lower by 0.19 dex (0Z) or 0.20 dex (Lai et al.) because we have used spectroscopic T_{eff} values to predict $\log g$ using the Y^2 isochrones.

For the stars in common with the 0Z and Lai et al. (2008) studies, using our approach the mean $[\text{Fe II}/\text{Fe I}]$ ratio is $+0.16 \pm 0.04$ dex ($\sigma = 0.15$ dex). Using the alternate approach the mean is $+0.12 \pm 0.02$ dex ($\sigma = 0.08$ dex). We also divide these stars into classes of giants or subgiants. For the giants, using the alternate approach would reduce the mean difference from $+0.20 \pm 0.04$ ($\sigma = 0.14$) to $+0.14 \pm 0.02$ ($\sigma = 0.07$). For the subgiants, the differences are even smaller, $+0.10 \pm 0.07$ ($\sigma = 0.17$) using our approach and $+0.09 \pm 0.04$ ($\sigma = 0.10$) using the alternate approach. These results suggest that our approach may slightly overestimate the amount of overionization occurring for Fe I in the giants.

8.7. Iron Abundance Trends with Wavelength

Roederer et al. (2012) identified a relationship between wavelength and iron abundance derived from Fe I lines in four metal-poor giants, and Lawler et al. (2013) found a similar effect in a metal-poor turnoff star. This effect is characterized as a decrease in the average abundance by ≈ 0.05 to 0.20 dex at short wavelengths (mainly $2280 < \lambda < 4000$ Å) compared to long wavelengths ($\lambda > 4400$ Å). Roederer et al. investigated several explanations for this effect and favored an unidentified extra source of continuous opacity at short wavelengths that was not accounted for. Ultimately that study only adopted an empirical correction to the abundances derived from lines at short wavelengths so as to match the abundances derived from longer wavelengths. The four stars in that study are also in our study (HD 108317, HD 122563, HD 126238, and HD 128279). Our derived temperatures are different by 30 to 70 K because of the different techniques used to derive the model atmosphere parameters. We do not find a similar effect for these four stars, although the number of Fe I lines studied at short wavelengths is considerably smaller than the sample examined by Roederer et al.

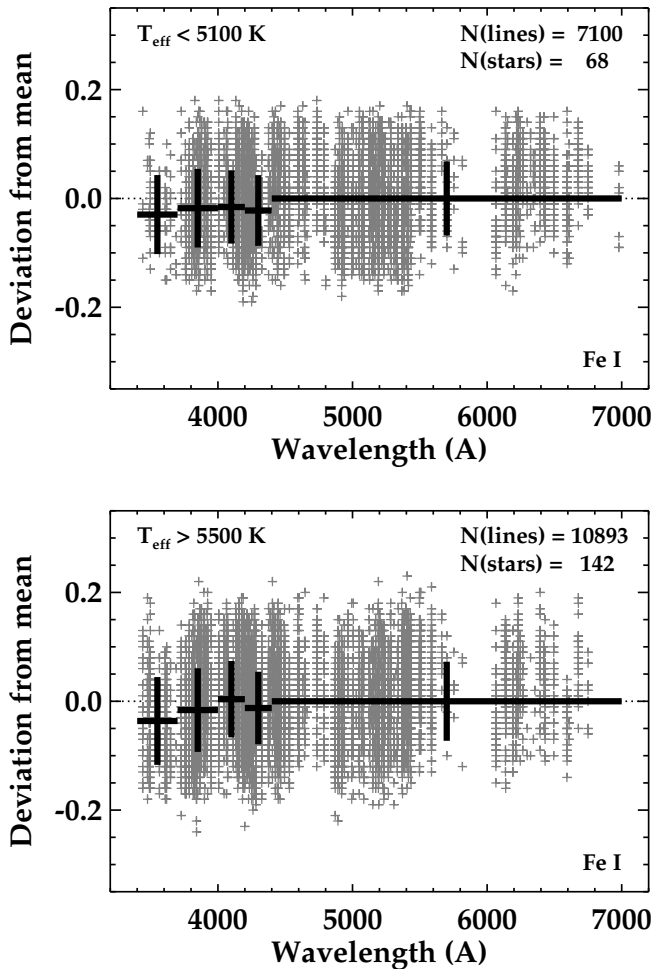


FIG. 15.— Line-by-line abundances derived from Fe I lines as a function of wavelength. The top panel shows lines in stars on the upper giant branch with $T_{\text{eff}} < 5100$ K, and the bottom panel shows lines in stars with $T_{\text{eff}} > 5500$ K and cooler than the MSTO. Small gray crosses mark individual lines, and bold black crosses mark the mean and standard deviation in each of several wavelength bins. All abundances are normalized to the mean abundance for each star derived from lines with $\lambda > 4400$ Å, which is marked by the dotted black line.

We take advantage of our large sample of stars to improve the statistics at short wavelengths. Figure 15 illustrates the wavelength dependence of abundances derived from Fe I lines in our study for 68 giants and 142 subgiants. Abundances derived from Fe I lines at short wavelengths are, on average, lower by 0.04 dex or less than lines at long wavelengths. The results do not change when comparing smaller subsets of stars with similar T_{eff} and metallicity. This is a very small difference compared to what Roederer et al. (2012) found, and the difference may be related to the methods used to derive model parameters. Roederer et al. derived model parameters mainly using lines at long wavelengths, only considering the abundances from lines at short wavelengths once the model parameters had been set. In the present study, we have included all Fe I lines when deriving the model parameters. This choice was necessary because a substantial part of our sample is warmer and more metal-poor than the stars considered by Roederer et al., hence fewer lines at long wavelengths are available to us. If lines at

short wavelength yield systematically lower abundances, they will preferentially be culled by our 2σ -clipping algorithm described in Section 8.1. Our experience suggests that this is a possibility, so the results shown in Figure 15 should be taken as lower limits to the differences at short wavelengths.

Lines of other species are not affected by the 2σ -clipping algorithm but would be affected if there is a physical origin of this effect, like missing continuous opacity. We devote our attention in Section 9.3 to finding other evidence of such an effect.

8.8. Other Considerations

McWilliam et al. (1995b) noted that the first (uppermost) levels of the grids of model atmospheres available at the time, those of Bell et al. (1976) and Kurucz⁶, began at different atmosphere layers. For a typical metal-poor giant (BD-18 5550), these models began at column masses (“RHOX”) near 13 and 0.2 g cm^{-2} , respectively. In the Bell et al. model, the optical depth at line center of lines stronger than $\log(\text{EW}/\lambda) > -4.7$ was nonzero in the first layer, indicating that a significant portion of the line was formed above this layer. While the Kurucz models covered the entire line-forming region, they too failed to include the temperature inversion expected in the low density layers of the chromosphere. This introduced a different set of problems since the cores of strong lines may be formed in these layers. Models of BD-18 5550 from the current MARCS and ATLAS9 grids extend to 1.3 and 0.02 g cm^{-2} , respectively. This covers the line-forming region for lines up to $\log(\text{EW}/\lambda) \gg -4.0$ in the ATLAS9 models and $\log(\text{EW}/\lambda) = -4.45$ in the MARCS models. Fortuitously, $\log(\text{EW}/\lambda) = -4.45$ is also the typical upper bound for the EWs we have measured in giants, so both model grids treat the lines in our dataset comparably in this regard. Tests by McWilliam et al. (1995b) to account for the presence of a chromosphere indicate a zero-point uncertainty of approximately 0.1 dex for Fe I lines with $\log(\text{EW}/\lambda) > -4.7$ in metal-poor giants. This issue is not resolved by the updated models and will affect our results for the giants. For typical metal-poor dwarf or subgiant models we obtain similar results, in that the MARCS models do not encompass the entire line-forming region for $\log(\text{EW}/\lambda) > -4.50$. Fe I lines with $\log(\text{EW}/\lambda) > -4.50$ (-4.45) comprise less than 2.0% (0.7%) of the total Fe I lines in our sample and are unlikely to skew the derived atmospheric parameters significantly. This could, however, impact species whose abundance can only be deduced from strong lines. In Section 9.3 we consider systematic abundance offsets associated with different lines of the same species.

Using spherically-symmetric model atmospheres with an analysis code that treats the line-forming layers as parallel slabs can lead to systematic errors in the derived abundances. The spherical models have a slightly lower temperature structure in the uppermost layers due to dilution of the radiation field from lower layers (Gustafsson et al. 2008). We find that the magnitude of this effect is small, less than a few percent in the most extreme cases (i.e., stars with very low surface gravity), where the main

⁶ Cited by McWilliam et al. (1995b) as Kurucz, R. L., 1992, private communication

difference lies in optically-thin layers with $\log \tau < -1$. We therefore make no corrections for this effect.

The current version of MOOG includes Rayleigh scattering from neutral H atoms in the source function (Sobeck et al. 2011). Our calculations indicate that opacity from Rayleigh scattering contributes 14% of the total continuous opacity at 3700 Å in typical metal-poor red giants at $\tau = 1$. To the extent that the Rayleigh scattering contribution is being properly computed, it should be included. (The other dominant contribution to the continuous opacity in these stars comes from bound-free absorption by H^- .) In typical metal-poor subgiants, the contribution from Rayleigh scattering is much less than 1% at all wavelengths considered.

The classical technique of deriving the microturbulence velocity from Fe I lines, which we have used, may systematically overestimate v_t because of correlated errors in the measured EWs and derived abundances (Magain 1984). Theoretical EWs computed from the stellar model could eliminate this particular bias. Mucciarelli (2011) has reexamined the situation, finding that the two methods produce equivalent results when moderately high S/N data are used ($S/N \gtrsim 70/1$). Our data generally fall in this regime since we are not typically measuring weak lines (i.e., those most prone to the bias) at blue wavelengths where the S/N is lower. Even in our HET spectra, where the S/N is lowest, no more than 4% of our Fe I lines would be susceptible to this bias. We do not pursue the matter further.

Distances calculated from absolute magnitudes computed from spectroscopically-derived T_{eff} or $\log g$ will be systematically overestimated relative to distances calculated from photometric determinations of T_{eff} or $\log g$. Any analysis that makes use of these distances to examine the kinematic properties of our sample will be affected. A proper analysis of the stellar kinematics is deferred for future work.

9. ABUNDANCE ANALYSIS

On average, we derive abundances or upper limits from 216 ($\sigma = 48$) of the 474 lines considered in each star. For all lines with an EW measurement listed in Table 5, we use MOOG to compute theoretical EWs that are forced to match the measured EWs by adjusting the input abundance. For lines denoted “synth” in Table 5, we use MOOG to generate a series of synthetic spectra where the abundance of the element producing the line of interest is varied to match the observed spectrum. Each synthesis spans ± 3 Å on either side of this line. We generate the line lists used in the synthesis using the Kurucz & Bell (1995) line lists as a starting point. We then replace the $\log gf$ values of the line of interest and any other lines with data from laboratory or more detailed theoretical studies, where available. Occasionally, especially for lines in the blue regions of the spectrum, we are forced to alter the theoretical $\log gf$ values to produce a reasonable fit to the observed spectrum. These lists are then employed, unchanged, for syntheses of all stars in the sample. We do allow for abundance variations of elements other than the one of interest based on our EW analysis for each star. Abundances derived from lines of Li I, CH, CN, NH, Al I, Sc II, V I, V II, Mn I, Mn II, Co I, Cu I, and elements with $Z > 30$ are determined via the synthesis method. All others are derived using EWs.

TABLE 10
ABUNDANCES DERIVED FROM INDIVIDUAL LINES

Star	Species	Wavelength (Å)	$\log \epsilon$	σ
CS 22166-016	Li I	6707.80	< 0.44	...
CS 22166-016	Mg I	4057.51	5.02	0.17
CS 22166-016	Mg I	4167.27	5.07	0.18
CS 22166-016	Mg I	5172.68	5.15	0.39
CS 22166-016	Mg I	5183.60	5.02	0.37
CS 22166-016	Mg I	5528.40	5.13	0.19

NOTE. — The complete version of Table 10 is available online only. A short version is shown here to illustrate its form and content.

We estimate an upper limit on the abundance for lines not detected in our spectra. The 3σ upper limits are calculated from a version of the formula presented on p. 590 of Frebel et al. (2008a), which itself is derived from equation A8 of Bohlin et al. (1983). When multiple lines of the same species are not detected, we adopt the upper limit that provides the strongest constraint on the abundance.

The presence of multiple isotopes of some lines of interest may lead to small energy shifts in the transition wavelength, and our syntheses account for the IS for Ba II, Nd II, Sm II, Eu II, Yb II, Ir I, and Pb I. In all cases we adopt the r -process isotopic ratios presented in Sneden et al. (2008) unless our analysis reveals a substantial contribution of s -process material. In that case, we adopt an appropriate mix of r - and s -process isotopes based on our derived abundances.

Abundances and uncertainties for each line in each star are reported in Table 10. The mean abundances and uncertainties are presented in Table 11. The full versions of Tables 10 and 11 are available in the online edition of the journal. The meanings of the different uncertainty estimates in Table 11 are discussed in Section 9.1. The ratios relative to the Solar values, $[X/H]$ or $[X/Fe]$, where X stands for any metal, are computed relative to the Asplund et al. (2009) Solar photospheric abundances, listed in Table 12. In cases where the photospheric value is poorly known, we adopt the abundance measured in CI-type carbonaceous meteorites instead. These cases are noted in Table 12. We remind readers that $[X/Fe]$ ratios are constructed using the abundances derived from species in the same ionization state; i.e., neutrals to neutrals and ions to ions. Only $\log \epsilon$ abundances or upper limits, not $[X/Fe]$ ratios, are presented for lithium and technetium.

Molecular abundances are derived by spectrum synthesis. For the NH lines near 3360 Å, we adopt the Kurucz & Bell (1995) line list with $\log gf$ values reduced by a factor of two and a dissociation potential of 3.45 eV, as recommended by Johnson et al. (2007). For the CN lines near 3880 Å, we adopt the Kurucz & Bell line lists without change and a dissociation potential of 7.65 eV. For the CH lines near 4310 Å, we adopt the line list of B. Plez (2007, private communication) and a dissociation potential of 3.47 eV. We adopt a default fitting uncertainty of 0.15 dex for the CH lines, 0.20 dex for the CN lines, and 0.30 dex for the NH lines. The final abundances listed in Table 11 reflect the CH and NH abundances, when possible, otherwise the nitrogen abundance is de-

TABLE 11
 MEAN ABUNDANCES

Star	Species	N_{lines}	$\log \epsilon$	$[\text{X}/\text{Fe}]^{\text{a}}$	$\sigma_{\text{statistical}}$	σ_{total}	σ_{neutrals}	σ_{ions}
CS 22166-016	Fe I	96	4.28	-3.22	0.06	0.15	0.00	0.00
CS 22166-016	Fe II	11	4.41	-3.09	0.07	0.15	0.00	0.00
CS 22166-016	Li I	1	< 0.52
CS 22166-016	C (CH)	1	5.35	0.01	0.15	0.25	0.19	0.19
CS 22166-016	N (NH)	1	5.34	0.60	0.30	0.36	0.32	0.32
CS 22166-016	O I	0
CS 22166-016	Na I	0
CS 22166-016	Mg I	5	5.07	0.69	0.05	0.15	0.08	0.18
CS 22166-016	Al I	1	2.56	-0.67	0.09	0.29	0.24	0.30
CS 22166-016	Si I	0
CS 22166-016	K I	0
CS 22166-016	Ca I	11	3.73	0.62	0.11	0.17	0.12	0.20
CS 22166-016	Sc II	6	0.01	-0.05	0.06	0.15	0.17	0.10
CS 22166-016	Ti I	15	2.01	0.29	0.07	0.15	0.09	0.18
CS 22166-016	Ti II	22	2.08	0.22	0.06	0.15	0.17	0.09
CS 22166-016	V I	1	0.68	-0.03	0.14	0.19	0.15	0.22
CS 22166-016	V II	2	0.99	0.15	0.20	0.24	0.26	0.21
CS 22166-016	Cr I	6	2.27	-0.15	0.06	0.14	0.08	0.18
CS 22166-016	Cr II	2	2.63	0.08	0.11	0.18	0.20	0.13
CS 22166-016	Mn I	4	1.78	-0.42	0.08	0.16	0.10	0.20
CS 22166-016	Mn II	4	1.74	-0.60	0.15	0.21	0.23	0.17
CS 22166-016	Co I	5	1.77	0.00	0.14	0.20	0.15	0.23
CS 22166-016	Ni I	6	3.07	0.07	0.11	0.21	0.16	0.23
CS 22166-016	Cu I	0
CS 22166-016	Zn I	0
CS 22166-016	Ga I	0
CS 22166-016	Rb I	0
CS 22166-016	Sr II	2	-0.50	-0.28	0.04	0.25	0.25	0.25
CS 22166-016	Y II	1	-1.41	-0.53	0.10	0.17	0.20	0.12
CS 22166-016	Zr II	3	-0.57	-0.06	0.12	0.18	0.21	0.14
CS 22166-016	Nb II	1	< 0.12	1.75
CS 22166-016	Mo I	1	<-0.41	0.93
CS 22166-016	Tc I	1	<-0.11
CS 22166-016	Ru I	0
CS 22166-016	Sn I	1	< 0.95	2.10
CS 22166-016	Ba II	3	-1.35	-0.44	0.05	0.15	0.17	0.09
CS 22166-016	La II	1	-2.07	-0.08	0.18	0.22	0.24	0.19
CS 22166-016	Ce II	5	<-1.62	-0.11
CS 22166-016	Pr II	1	-1.84	0.53	0.17	0.22	0.24	0.18
CS 22166-016	Nd II	1	-1.85	-0.18	0.11	0.18	0.20	0.13
CS 22166-016	Sm II	0
CS 22166-016	Eu II	3	-2.37	0.19	0.13	0.19	0.21	0.15
CS 22166-016	Gd II	2	<-1.21	0.81
CS 22166-016	Tb II	0
CS 22166-016	Dy II	1	-1.70	0.29	0.14	0.20	0.22	0.15
CS 22166-016	Ho II	0
CS 22166-016	Er II	1	-1.70	0.47	0.40	0.43	0.44	0.41
CS 22166-016	Tm II	0
CS 22166-016	Yb II	1	-2.10	0.07	0.12	0.19	0.21	0.14
CS 22166-016	Hf II	2	<-0.94	1.30
CS 22166-016	Ir I	0
CS 22166-016	Pb I	1	< 0.53	1.71
CS 22166-016	Th II	3	<-1.95	1.08

NOTE. — The complete version of Table 11 is available online only. A short version illustrating the results for one star is shown here to illustrate its form and content.

^a $[\text{Fe}/\text{H}]$ is indicated for Fe I and Fe II

rived from the CN abundance after carbon has been set using the CH lines. Molecular formation in cool stellar atmospheres is sensitive to the temperature and density, especially the presence and degree of granulation found in three-dimensional hydrodynamical models (e.g., Collet et al. 2007). These effects are difficult to quantify. Our one-dimensional LTE results should be treated with due caution when using them for anything besides gross discriminants of carbon and nitrogen enrichment.

For all lines with $\lambda > 5670 \text{ \AA}$, we examine the stellar spectrum simultaneously with a telluric spectrum of earth's atmosphere (Hinkle et al. 2000). In general, we

did not observe hot telluric standards during our observing program, so any lines that appear to be compromised by telluric absorption are discarded from further consideration. Furthermore, the Na I D lines are sometimes blended with interstellar sodium absorption. We do not attempt to derive abundances from these lines when they appear asymmetric, broadened beyond the typical stellar line widths, or when the telluric spectrum suggests that they may be compromised.

Several stars in our sample have low $[\alpha/\text{Fe}]$ ratios, so using the α -enhanced grid of models may not, in principle, be appropriate. To test how much of an effect this may have on our analysis, we have performed the

TABLE 12
ADOPTED SOLAR
ABUNDANCES

Element	Z	log ϵ
Li	3	...
C	6	8.43
N	7	7.83
O	8	8.69
Na	11	6.24
Mg	12	7.60
Al	13	6.45
Si	14	7.51
K	19	5.03
Ca	20	6.34
Sc	21	3.15
Ti	22	4.95
V	23	3.93
Cr	24	5.64
Mn	25	5.43
Fe	26	7.50
Co	27	4.99
Ni	28	6.22
Cu	29	4.19
Zn	30	4.56
Ga	31	3.04
Rb	37	2.52
Sr	38	2.87
Y	39	2.21
Zr	40	2.58
Nb	41	1.46
Mo	42	1.88
Tc	43	...
Ru	44	1.75
Sn	50	2.07 ^a
Ba	56	2.18
La	57	1.10
Ce	58	1.58
Pr	59	0.72
Nd	60	1.42
Sm	62	0.96
Eu	63	0.52
Gd	64	1.07
Tb	65	0.30
Dy	66	1.10
Ho	67	0.48
Er	68	0.92
Tm	69	0.10
Yb	70	0.92 ^a
Hf	72	0.85
Ir	77	1.38
Pb	82	2.04 ^a
Th	90	0.06 ^a

^a Meteoritic abundance

abundance analysis for several key species using an α -enhanced model and an α -normal model for the two most α -poor stars in our sample, G004-036 and BD+80 245. The results of this test are listed in Table 13. For G004-036, a subgiant, the differences in derived log ϵ are all smaller than 0.007 dex, and ratios constructed among abundances derived from like ionization states differ by 0.002 dex or less. For BD+80 245, the differences in derived log ϵ are larger than 0.002 dex only for ionized species, for which the differences are as large as 0.019 dex. Ratios constructed among abundances derived from like ionization states differ by 0.005 dex or less. Differences among abundances derived from unlike ionization states, e.g., [Fe I/Fe II], are 0.021 dex or smaller, and we (again) advise against constructing abundance ratios this way. For stars with intermediate $[\alpha/\text{Fe}]$ ratios, these differences will be smaller. On the basis of this test, we con-

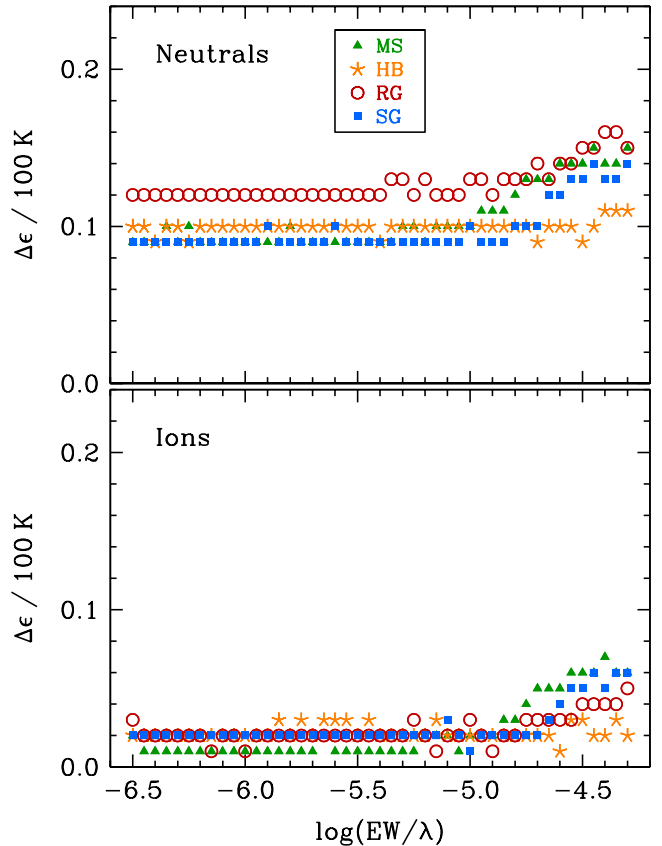


FIG. 16.— Change in derived abundances of neutral lines (top) and singly-ionized lines (bottom) resulting from a change in T_{eff} of 100 K.

clude that using the α -enhanced models for all stars in the sample will have, at most, a minimal effect on the derived abundance ratios.

9.1. Uncertainties

We estimate abundance uncertainties following the formalism presented in McWilliam et al. (1995b). The standard deviation of a single line is calculated according to equation A5 of McWilliam et al. To evaluate the partial derivatives, we have selected model atmospheres representing stars in our sample on the red giant branch, subgiant branch, horizontal branch, and main sequence. Then, following McWilliam et al., we alter the model parameters one by one to estimate the change in the abundance that results in fictitious iron lines whose strength spans the full range of line strengths considered in our sample. We repeat this exercise for both neutral lines and singly-ionized lines.

The results of this exercise are illustrated in Figures 16 through 18. As expected, lines of neutral atoms are more sensitive to T_{eff} than lines of ionized atoms are, and the opposite is true for pressure sensitivity (log g). For strong lines, the microturbulence velocity parameter dominates the uncertainties. In practice, we fit the relationships shown in Figures 16 through 18 by polynomial functions (often just constants over much of the range of line strength) and use these in our calculations. The uncertainty in abundance resulting from uncertainty in the EW measurement is estimated in a similar manner by al-

TABLE 13
ABUNDANCE DIFFERENCES DERIVED FROM α -ENHANCED AND α -NORMAL
MODELS

Species or Ratio	G004-036			BD+80 245		
	Δ	σ	N_{lines}	Δ	σ	N_{lines}
$\log \epsilon(\text{Mg I})$	+0.004	0.005	7	+0.010	0.012	4
$\log \epsilon(\text{Ca I})$	+0.004	0.005	10	+0.001	0.005	11
$\log \epsilon(\text{Ti I})$	+0.005	0.005	15	-0.002	0.004	13
$\log \epsilon(\text{Ti II})$	+0.007	0.005	19	+0.019	0.003	17
$\log \epsilon(\text{Cr I})$	+0.003	0.005	9	+0.000	0.004	11
$\log \epsilon(\text{Cr II})$	+0.007	0.006	3	+0.013	0.006	3
$\log \epsilon(\text{Fe I})$	+0.003	0.005	87	+0.002	0.006	66
$\log \epsilon(\text{Fe II})$	+0.006	0.005	10	+0.017	0.005	10
$\log \epsilon(\text{Ni I})$	+0.006	0.005	7	+0.001	0.004	8
$[\text{Mg I}/\text{Fe I}]$	+0.001	0.007	...	+0.008	0.013	...
$[\text{Ca I}/\text{Fe I}]$	+0.001	0.007	...	-0.002	0.008	...
$[\text{Ti I}/\text{Fe I}]$	+0.001	0.007	...	-0.005	0.007	...
$[\text{Ti II}/\text{Fe II}]$	+0.001	0.007	...	+0.002	0.006	...
$[\text{Cr I}/\text{Fe I}]$	+0.000	0.007	...	-0.002	0.007	...
$[\text{Cr II}/\text{Fe II}]$	+0.001	0.008	...	-0.004	0.008	...
$[\text{Ni I}/\text{Fe I}]$	+0.002	0.007	...	-0.001	0.007	...
$[\text{Ti I}/\text{Ti II}]$	-0.003	0.007	...	-0.021	0.006	...
$[\text{Cr I}/\text{Cr II}]$	-0.003	0.008	...	-0.013	0.007	...
$[\text{Fe I}/\text{Fe II}]$	-0.003	0.007	...	-0.015	0.008	...

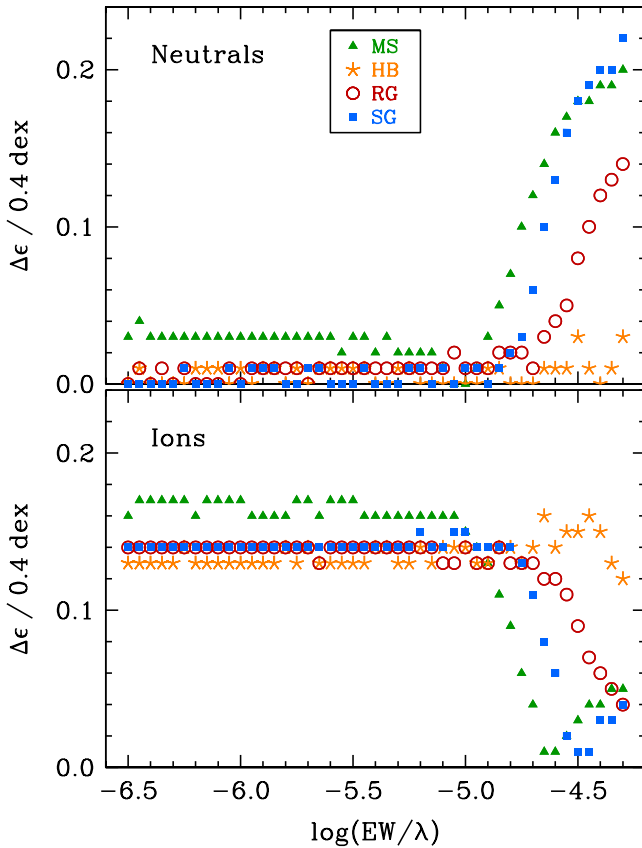


FIG. 17.— Change in derived abundances of neutral lines (top) and singly-ionized lines (bottom) resulting from a change in $\log g$ of 0.4 dex. Symbols are the same as in Figure 16.

tering the line strength by $1 \text{ m}\text{\AA}$, as shown in Figure 19. As expected, this corresponds to a proportionally larger uncertainty for weaker lines. In practice, we adopt a wavelength-dependent uncertainty for the EW based on the median S/N ratios.

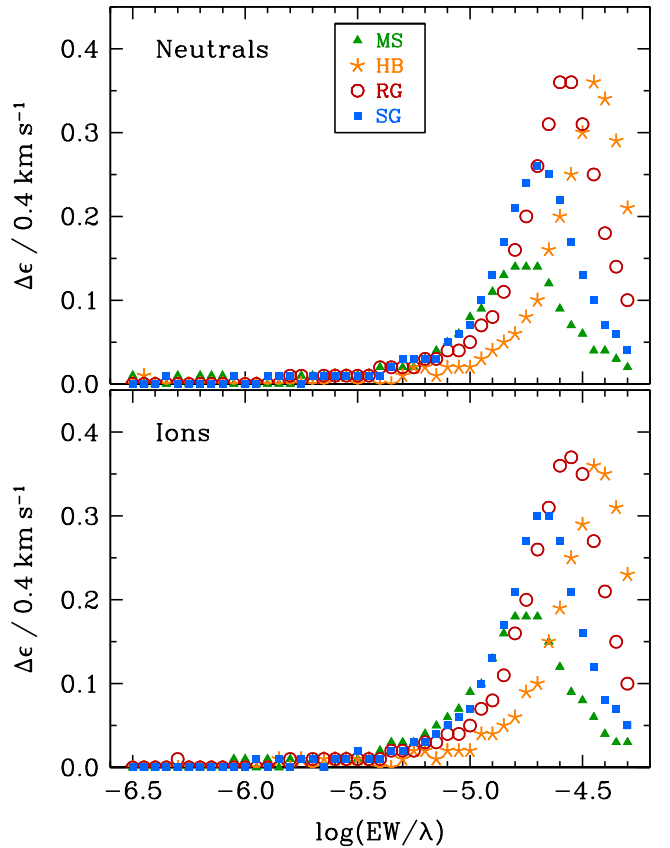


FIG. 18.— Change in derived abundances of neutral lines (top) and singly-ionized lines (bottom) resulting from a change in v_t of 0.4 km s^{-1} . Symbols are the same as in Figure 16.

The cross term for T_{eff} and $\log g$ in equation A5 of McWilliam et al. (1995b) is evaluated using the procedure outlined by Johnson (2002). For each of our model atmospheres of representative stars, we compare the $\log g$ parameters derived when altering the input T_{eff} by an

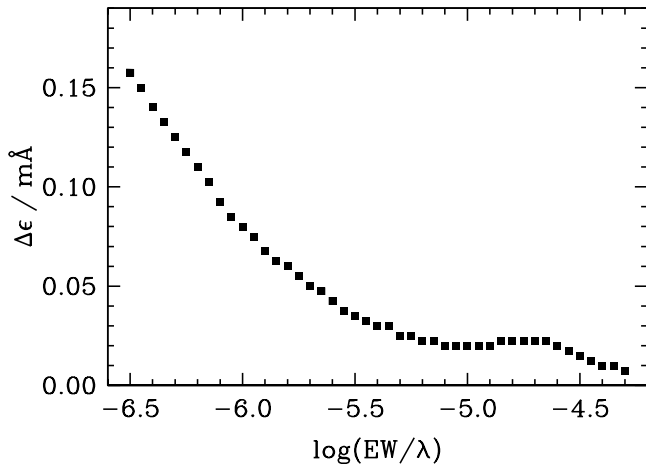


FIG. 19.— Change in derived abundances of lines of various strength resulting from a change in EW of 1 mÅ.

amount corresponding to a random draw of T_{eff} from a normal distribution with $\sigma = \sigma_{T_{\text{eff}}}$, where $\sigma_{T_{\text{eff}}}$ is typical for stars in each evolutionary state. We repeat this exercise 10 times for each covariance for a representative case for each evolutionary state. The covariance, $\sigma_{T \log g}$, is then estimated according to equation 3 of Johnson (2002). For stars in the RG, SG, HB, and MS classes, $\sigma_{T \log g}$ is 5.1, 1.2, 2.8, and 2.2; $\sigma_{\log g v_t}$ is -0.04 , -0.02 , -0.03 , and -0.01 ; and $\sigma_{v_t T}$ is 44, 38, 45, and 16. The 1σ uncertainties are listed for each line in each star in Table 10.

We compute mean abundances weighted by the uncertainty given by equation A5 of McWilliam et al. (1995b). These abundances are reported in Table 11. Several sets of uncertainties are listed in this table. The statistical uncertainty, $\sigma_{\text{statistical}}$, is that given by equation A17 of McWilliam et al., which includes uncertainties in the EW measurement and $\log gf$ values. This uncertainty generally decreases as the number of lines examined increases, although we have forced an artificial minimum uncertainty of 0.02 dex to guard against unreasonably small values. The total uncertainty, σ_{total} , is that given by equation A16 of McWilliam et al. This includes the statistical uncertainty and uncertainties in the model atmosphere parameters and does not decrease appreciably as the number of lines increases. For this calculation, we adopt the estimates of the systematic uncertainties in the model atmosphere parameters given in Section 8.5. The remaining two uncertainties listed in Table 11 are approximations to the abundance ratio uncertainties given by equations A19 and A20 of McWilliam et al. Rather than calculating and presenting this uncertainty for every possible element pair, we have computed these uncertainties using Fe I and Fe II as representative cases. We suggest that σ_{neutrals} for element A should be added in quadrature with $\sigma_{\text{statistical}}$ for element B when computing the ratio [A/B] when B is derived from neutral lines. Similarly, we suggest that σ_{ions} for element A should be added in quadrature with $\sigma_{\text{statistical}}$ for element B when element B is derived from ionized lines. (The uncertainty in the ratio [B/A] may not necessarily equal that for [A/B], but in general they are comparable.)

9.2. Corrections for Departures from LTE in the Line Formation Calculations

Great effort in recent years has been dedicated to identifying transitions that are not well represented by the assumptions of LTE in late-type stellar atmospheres. We adopt non-LTE corrections for the abundances derived from lines of Li I, O I, Na I, and K I. Grids of non-LTE calculations spanning a range of stellar parameters and metallicities have been presented for various lines of these species, as discussed below. The abundances presented in Tables 10 and 11 reflect these corrections on Li I, O I, Na I, and K I. For investigators who wish to make use of our uncorrected LTE abundances of these species, we list the corrections in Table 14. The complete version of this table is available only in the online edition of the journal. Lines of other species may not be formed in LTE, but grids of non-LTE abundance calculations for these species in late-type stars are not readily available.

For the Li I 6707 Å line, we use the corrections computed by Lind et al. (2009). For the few stars with parameters outside the grid of their calculations ($4000 \leq T_{\text{eff}} \leq 8000$ K, $1.0 \leq \log g \leq 5.0$, $1.0 \leq v_t \leq 5.0$ km s $^{-1}$, $-5.0 \leq [\text{Fe}/\text{H}] \leq 0$), we use the value at the nearest point on the grid. The corrections are generally positive for cool stars and negative for warm stars. The corrections for upper limits are calculated based on the 3σ EW estimated from the S/N measurements, so they should be treated with caution. Most corrections are small, $< \pm 0.05$ dex, but a few are as large as ± 0.13 dex for lines detected. We include an additional 0.05 dex statistical uncertainty in our error estimates to account for uncertainties in the corrections.

The O I triplet at 7771, 7774, and 7775 Å is not formed in LTE, and we adopt the corrections presented by Fabian et al. (2009). For the few stars with parameters outside the grid of their calculations ($4500 \leq T_{\text{eff}} \leq 6500$ K, $2.0 \leq \log g \leq 5.0$, $-3.0 \leq [\text{Fe}/\text{H}] \leq 0$), we use the value at the nearest point on the grid. We include an additional 0.1 dex statistical uncertainty in our error estimates to account for uncertainties in the corrections. After correcting these abundances, however, the resulting oxygen abundances are, on average, 0.50 ± 0.06 dex ($\sigma = 0.25$ dex) higher than those derived from the [O I] 6300 Å line in the seven stars where both abundance indicators could be reliably measured. The [O I] 6300 Å line is generally considered to be a reliable abundance indicator formed under conditions of LTE (Kiselman 2001). The offset between abundances derived from [O I] and O I is reminiscent of the result found by García Pérez et al. (2006) in metal-poor giants. We apply a correction for this offset as discussed in Section 9.3.

The lines of the Na I D resonance doublet at 5898 and 5895 Å are not formed under conditions of LTE. We adopt corrections to our LTE abundances using the grid presented by Lind et al. (2011). The corrections are always negative, in the sense that LTE underestimates the line strength and overestimates the abundance. Lind et al. also present corrections for the higher excitation Na I 5682 and 5688 Å lines. We also include these corrections, which are generally small (< 0.1 dex) for consistency. For the few stars with parameters outside the grid of their calculations ($4000 \leq T_{\text{eff}} \leq 8000$ K, $1.0 \leq \log g \leq 5.0$,

TABLE 14
NON-LTE ABUNDANCE CORRECTIONS

Star	Li I	O I			Na I				K I	
	6707	7771	7774	7775	5682	5688	5889	5895	7664	7698
CS 22166–016	+0.08
CS 22169–008	−0.03	−0.22	−0.22
CS 22169–035	+0.14	−0.05	−0.05	−0.05	−0.27
CS 22171–031	−0.04	−0.26	−0.26	−0.25
CS 22171–037	−0.03	−0.46	−0.45	−0.45	−0.05	−0.05

NOTE. — The complete version of Table 14 is available online only. A short version is shown here to illustrate its form and content.

$1.0 \leq v_t \leq 5.0 \text{ km s}^{-1}$, $-5.0 \leq [\text{Fe}/\text{H}] \leq +0.5$), we use the value at the nearest point on the grid. We include an additional 0.1 dex statistical uncertainty in our error estimates to account for uncertainties in the corrections.

Observational challenges have limited studies of potassium in metal-poor stars. Only two K I lines are routinely detectable in late-type metal-poor stars, the 7664 and 7698 Å K I resonance doublet. These stellar lines are often contaminated with atmospheric O₂ lines. Our spectra extend redward enough to observe these lines. As in the case of the Na I resonance doublet discussed in Section 9, we only measure EWs of these lines when one or both appears well separated from the model telluric absorption spectrum. These resonance lines are likely formed out of LTE, and we adopt corrections for the 7698 Å line from the grid of Takeda et al. (2002). Corrections for the 7664 Å line are made from an analogous grid kindly sent by Y. Takeda (2007, private communication). The corrections are almost always negative, in the sense that LTE underestimates the line strength and overestimates the abundance. For stars with parameters outside the grid of their calculations ($4500 \leq T_{\text{eff}} \leq 6500 \text{ K}$, $1.0 \leq \log g \leq 5.0$, $1.0 \leq v_t \leq 3.0 \text{ km s}^{-1}$, $-3.0 \leq [\text{Fe}/\text{H}] \leq 0$), we use the value at the nearest point on the grid. We report detections of the K I 7664 and 7698 Å lines in 41 stars and 72 stars, respectively, for a total of 98 stars with potassium abundance derivations. Both lines are detected in 15 stars, and the corrected abundances agree well in these stars: $\Delta = -0.019 \pm 0.024$ ($\sigma = 0.093$). We include an additional 0.1 dex statistical uncertainty in our error estimates to account for uncertainties in the corrections.

9.3. Line-by-line Abundance Offsets and Corrections

One challenge in producing a homogeneous abundance dataset for stars spanning several dex in metallicity is that the set of useful lines for analysis changes from metal-poor to metal-rich stars. If systematic line-to-line differences in the derived abundances persist, they will masquerade as subtle changes in the abundance trends. While observers are generally aware of this effect (e.g., Cohen et al. 2004 discuss it in detail for the case of Mg I lines⁷), limitations in the size of the stellar sample of-

ten preclude attempts to characterize it reliably for large numbers of elements. This is of little consolation to those wishing to make use of abundance tables to constrain chemical evolution models. We attempt to account for these effects by leveraging our large dataset to identify and correct for lines that are systematically discrepant. In this section we discuss the process we use to identify those lines and the empirical corrections that we apply to the abundances.

These differences may originate from inaccurate $\log gf$ values or damping constants, departures from LTE in the line-forming layers, poor estimates of the continuous opacity, misidentification of the continuum, or unidentified blends. We can estimate which effects may dominate. The line density is highest in the blue region of the spectrum. If unidentified blends are the dominant source, the abundances we derive from blue lines should be higher on average than abundances derived from red lines, so the corrections would preferentially skew negative for blue lines. The corrections are both positive and negative in the blue region of the spectrum. This indicates that unidentified blends are not the main source of systematic uncertainty here. The magnitude of the corrections is higher in the blue than in the red, however. This suggests that higher line density and lower S/N ratios are rendering the continuum placement more uncertain. Simply adopting different analysis techniques—for example, using spectrum synthesis in place of a traditional EW analysis—does not offer a panacea. The dominant effects are likely to be uncertain continuum placement in the blue region of the spectrum and the deficiencies of using LTE to model the line formation.

For most species, we determine the corrections using the following process. We separate the stars into groups of different evolutionary classes (the RG, SG, HB, MS, and BS categories presented in Section 8.1). For each star in each group, using only stars with large numbers of lines of a given species measured, we compute the difference between each line’s resulting abundance and the mean abundance in that star. Within each evolutionary group, we then compute the mean and standard deviation of these differences. Finally, we correct all abundances from a given line in all stars of a given evolutionary group by subtracting these mean differences. These corrections are listed in Table 18. For example, we find that the Mg I 5183 Å line in the SG class yields abundances higher than the mean by 0.09 dex ($\sigma = 0.08$, $N = 49$ stars). Therefore we reduce the abundance derived from the 5183 Å line by 0.09 dex for all stars in the SG class. As a penalty incurred for making this statistical correction, we add in

⁷ The line-by-line differences for five Mg I lines listed in Table 12 of Cohen et al. (2004) agree in sign but not magnitude with ours in Table 18 after correcting for the different $\log gf$ values and number of lines examined. Their corrections would range from +0.16 dex for the 4057 Å line to −0.23 dex for the 5183 Å line if computed on the same $\log gf$ scale and in the same manner as ours. We cannot trace the source of this difference.

quadrature the standard deviation, in this case 0.08 dex, with the statistical uncertainty. Typically these uncertainties are not the dominant component of the statistical error budget. We apply all corrections, even if some are not statistically meaningful, to preserve the overall mean abundance of the sample. Some evolutionary groups do not contain enough measurements of a particular line to make a reliable assessment of the mean offset, in which case no correction is made. These cases are denoted by blanks in Table 18. A few species present unique challenges that require minor modifications to this process, as discussed below.

We use four sodium abundance indicators in our analysis, the Na I resonance doublet at 5889 and 5895 Å and the higher excitation doublet at 5682 and 5688 Å. After correcting for non-LTE effects, the two lines within each doublet yield abundances in excellent agreement with each other on average: $\Delta_{5889-5895} = -0.02 \pm 0.02$ ($\sigma = 0.06$) and $\Delta_{5688-5682} = -0.01 \pm 0.03$ ($\sigma = 0.13$). There are only two stars where three or four of these lines could be measured reliably, so we are unable to assess whether they differ systematically. Furthermore, there are insufficient data to assess systematic differences among stars of different evolutionary state, so we adopt a single set of corrections for all stars.

Previous studies (e.g., Preston et al. 2006a) have revealed relationships between [Si/Fe] and T_{eff} when the silicon abundance is derived from the Si I 3905 Å line. When possible, we avoid using this line as an abundance indicator and instead prefer the high excitation ($4.90 \leq EP \leq 5.06$ eV) Si I lines at 5665, 5701, 5708, and 5772 Å. Our analysis reveals that the low excitation Si I 3905 and 4102 Å lines ($EP = 1.91$ eV) give consistent results in the three stars where both can be reliably measured ($\Delta = 0.00 \pm 0.04$, $\sigma = 0.07$). In the nine stars with at least one high excitation line and at least one low excitation line used as abundance indicators, the high excitation lines yield abundances higher by 0.14 ± 0.05 dex ($\sigma = 0.15$) on average. Here, we adopt the convention to correct the abundances of the low excitation lines in all stars by +0.14 dex to match the average abundance of the high excitation lines. We do not include the low excitation lines in the reported mean silicon abundance for the 12 stars where at least one high excitation line is also used. This correction accounts for the higher silicon abundances reported for the more metal-poor stars in our sample when compared with other recent investigations.

Previous studies of Mn I lines in late-type stars have demonstrated that the three Mn I resonance lines at 4030, 4033, and 4034 Å yield abundances in LTE that are several tenths of a dex lower than the high-excitation neutral or singly-ionized lines (e.g., Cayrel et al. 2004; Roederer et al. 2010). We thus take the following approach to identifying line-by-line systematic offsets in our dataset. First, we identify any offsets among the high-excitation neutral lines from the mean of all high-excitation neutral lines within a given star. Then, we recompute the mean manganese abundance derived from the corrected high-excitation lines for each star. Finally, we identify any offsets among the neutral resonance lines relative to the corrected mean. This forces the resonance lines, on average, to have the same mean abundance as the high-excitation lines. Fortunately, the mean [Mn/Fe] ratio

derived from neutral lines shows only a small difference from the mean [Mn/Fe] ratio derived from the ionized lines, with a mean difference (ion minus neutral) of only -0.038 ± 0.011 ($\sigma = 0.14$). This level of agreement, not enforced by our method, is encouraging.

For Cu I, Tb II, Tm II, Ir I, and Th II, there are not enough stars with two or more lines measured to assess systematic offsets. For Co I, Y II, Ba II, and La II, there are not enough stars with two or more lines measured to assess systematic offsets in the MS class; in these cases, we adopt the corrections from stars in the SG class for the stars in the MS class. For Co I, a similar situation exists for stars in the HB class, and we also adopt the corrections from the stars in the SG class for stars in the HB class. For K I, Ce II, Pr II, Nd II, Sm II, Eu II, Gd II, Dy II, and Er II we adopt a single correction for stars in all evolutionary states. There are never enough stars in the BS class to define a separate set of corrections, so the abundances in these stars are corrected by adopting the offsets found for the stars in the SG class.

9.4. Comparison with Previous Studies

9.4.1. Differences in the [X/Fe] Ratios

We compare our derived [X/Fe] ratios, where X is a given element, with those derived by previous studies. In particular, we focus on the 18 red giants in common with the First Stars analysis. To keep the comparisons manageable when comparing with other studies, we limit ourselves to two other studies that also examined large numbers of stars in common with the First Stars analysis, those of McWilliam et al. (1995b) and Yong et al. (2013). Note that Yong et al. rederived abundances of these stars from published EW values. We also compare with the Bonifacio et al. (2009) sample of dwarfs. We perform a straight comparison of the results without accounting for differences in, e.g., the set of lines used or the transition probabilities.

The results of this comparison are listed in Table 15. The [X/Fe] ratios, many derived from transitions in neutral atoms, are generally overabundant in our analysis. This can easily be traced to the fact that our iron abundances derived from Fe I lines are ~ 0.1 dex lower than the iron abundance derived from Fe II (Figure 14), which are themselves lower than published [Fe/H] values by 0.27 dex, on average, for red giants (Table 8). A lower [Fe/H] value increases [X/Fe] if element X is not also derived from lines of similar excitation potential and strength. Ratios of neutral elements with the largest positive discrepancies, [Mg/Fe] and [Si/Fe], are often derived from (only) strong Mg I and Si I lines that are sensitive to the microturbulent velocity, and our derived v_t values are lower than those derived by previous studies (Table 8). This drives the [Mg/Fe] and [Si/Fe] ratios to even higher values. Our line-by-line corrections (Table 18) further increase [Si/Fe] when the 3905 Å Si I line is considered. The underabundances of [Sc/Fe] and [Co/Fe] with respect to Cayrel et al. (2004) can be accounted for by our inclusion of the hyperfine structure for Co I and Sc II lines, which desaturate the lines and lower the derived abundances. In principle, additional discrepancies may arise from differences in the transition probabilities, although we have not checked this explicitly since doing so would require examining which sets of

TABLE 15
COMPARISON OF $[X/Fe]$ RATIOS WITH PREVIOUS STUDIES

Ratio	McWilliam et al. (1995b) ^a	Cayrel et al. (2004) ^b	Yong et al. (2013)	Bonifacio et al. (2009)
$[C/Fe]$	-0.05 (0.18, 12)	-0.14 (0.20, 17)	...	+0.22 (0.15, 5)
$[N/Fe]$...	-0.12 (0.23, 13)
$[Na/Fe]$	+0.15 (0.13, 5)	+0.08 (0.19, 6)	-0.07 (0.21, 6)	...
$[Mg/Fe]$	+0.23 (0.18, 14)	+0.26 (0.14, 18)	+0.28 (0.13, 18)	+0.17 (0.08, 9)
$[Al/Fe]$	+0.01 (0.25, 14)	+0.16 (0.14, 18)	+0.08 (0.15, 18)	...
$[Si/Fe]$	+0.33 (0.29, 11)	+0.48 (0.20, 15)	...	+0.26 (0.12, 9)
$[Ca/Fe]$	+0.04 (0.10, 14)	+0.15 (0.09, 18)	+0.16 (0.07, 18)	+0.14 (0.05, 9)
$[Sc/Fe]$	-0.28 (0.25, 14)	-0.19 (0.08, 18)	-0.30 (0.11, 18)	-0.25 (0.20, 9)
$[Ti\ I/Fe]$	-0.11 (0.21, 12)	-0.05 (0.07, 18)	-0.10 (0.08, 18)	...
$[Ti\ II/Fe]$	-0.16 (0.13, 14)	-0.07 (0.10, 18)	-0.11 (0.18, 18)	-0.23 (0.18, 9)
$[Cr\ I/Fe]$	+0.12 (0.15, 14)	+0.11 (0.08, 18)	+0.11 (0.10, 18)	+0.01 (0.10, 9)
$[Mn\ I/Fe]$	+0.22 (0.30, 13)	-0.08 (0.12, 18)	+0.05 (0.21, 8)	+0.22 (0.11, 8)
$[Fe\ I/H]$	-0.41 (0.14, 14)	-0.31 (0.12, 18)	-0.31 (0.13, 18)	-0.27 (0.15, 9)
$[Fe\ II/H]$	-0.27 (0.14, 14)	-0.20 (0.13, 18)	-0.21 (0.13, 18)	-0.10 (0.13, 9)
$[Co/Fe]$	-0.28 (0.11, 14)	-0.29 (0.13, 18)	-0.16 (0.09, 18)	-0.15 (0.12, 7)
$[Ni/Fe]$	-0.23 (0.31, 13)	+0.12 (0.10, 18)	+0.07 (0.11, 18)	+0.05 (0.11, 9)
$[Zn/Fe]$...	+0.21 (0.12, 16)
$[Sr/Fe]$	-0.06 (0.25, 14)	-0.03 (0.20, 17)	+0.07 (0.45, 7)	-0.32 (0.45, 9)
$[Ba/Fe]$	+0.04 (0.25, 11)	-0.24 (0.18, 16)	...	+0.01 (0.52, 3)

NOTE. — Differences are in the sense of this study *minus* other. Each entry represents the mean difference, standard deviation, and number of stars: $\langle \Delta \rangle (\sigma, N)$.

^a Includes $[Ba/Fe]$ from McWilliam (1998)

^b Includes $[C/Fe]$ and $[N/Fe]$ from Spite et al. (2005) and $[Sr/Fe]$ and $[Ba/Fe]$ from François et al. (2007)

lines of each species were employed in each star by each analysis.

9.4.2. Dispersion in the $[X/Fe]$ Ratios

We can also compare the standard deviation of the $[X/Fe]$ ratios for stars in common with the First Stars, McWilliam et al. (1995b), and Yong et al. (2013) samples. In the absence of cosmic dispersion, this comparison offers an independent quantitative measure of the precision of the derived abundances. In practice, many of these abundance ratios do exhibit at least a small amount of cosmic dispersion, so the standard deviations are useful in a comparative sense. Table 16 lists the standard deviation in each ratio and the number of stars used to compute it for each of the four surveys.

The First Stars survey used higher quality spectroscopic observations than our survey or that of McWilliam et al. (1995a). The typical spectral resolution and S/N ratios are also listed in Table 16 for the stars in common among these three surveys. The First Stars observations correspond to an increase of a factor of ≈ 10 in total photons \AA^{-1} over our data and a factor of > 70 over the data of McWilliam et al.

Figure 20 illustrates these results for the $[Mg/Fe]$ through $[Zn/Fe]$ ratios, which are measured in most stars in each of these four surveys. The naive expectation would be that the abundance precision should roughly correlate with the data quality, and the dispersions generally support this expectation. The dispersions are generally smallest for the First Stars sample, followed by the Yong et al. (2013) rederivation and our sample, followed by the McWilliam et al. (1995b) sample. We do not achieve the same internal precision as the First Stars survey does for the giants; however, we have achieved reasonable precision on a photon budget roughly 10 times lower per star.

9.4.3. Detailed Comparisons of $[X/Fe]$ for Individual Stars

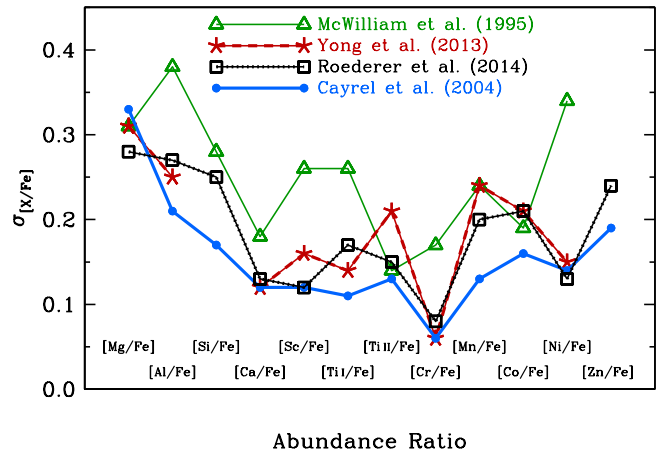


FIG. 20.— Dispersion in the derived abundance ratios of stars in common between our survey (“Roederer et al. 2014”), McWilliam et al. (1995b), Yong et al. (2013), and Cayrel et al. (2004). The number of stars used to compute each dispersion is listed in Table 16.

We also compare the detailed abundance patterns of two well-studied stars. CS 22892-052 is a well-studied giant with a high level of *r*-process enhancement. CS 22949-037 is another well-studied giant with substantial enhancement of carbon, nitrogen, and other light elements. The abundance pattern of each of these stars has been subject to close scrutiny by investigators over the last two decades, and we limit our comparison to a few extensive studies of each. Figure 21 illustrates these comparisons, and references are given in the figure caption.

In general the agreement is superb, but a couple of features stand out. Our $[Si/Fe]$ ratios are higher than found by previous work, as discussed above. The other prominent difference is that the $[X/Fe]$ ratios, where X represents one of the neutron-capture elements detected

TABLE 16
DATA QUALITY AND DISPERSIONS IN ABUNDANCE RATIOS FOR 18 STARS IN COMMON AMONG FOUR
LARGE SURVEYS

	This study	First Stars	Yong et al. (2013)	McWilliam et al. (1995a,b)
Resolution $\equiv \lambda/\Delta\lambda$	41,000	47,000	...	22,000
λ of S/N estimate	3950 Å	4000 Å	...	4800 Å
median S/N pix ⁻¹	72	150	...	35
median S/N RE ⁻¹	112	335	...	67
median photons Å ⁻¹	1.3×10^5	1.3×10^6	...	2.0×10^4
	σ (N)	σ (N)	σ (N)	σ (N)
[C/Fe]	0.54 (17)	0.49 (17)	...	0.48 (12)
[N/Fe]	0.78 (12)	0.70 (15)
[Na/Fe]	0.15 (6)	0.44 (14)	0.55 (15)	0.64 (13)
[Mg/Fe]	0.28 (18)	0.33 (18)	0.31 (18)	0.31 (14)
[Al/Fe]	0.27 (18)	0.21 (18)	0.25 (18)	0.38 (14)
[Si/Fe]	0.25 (15)	0.17 (18)	...	0.28 (14)
[Ca/Fe]	0.13 (18)	0.12 (18)	0.12 (18)	0.18 (14)
[Sc/Fe]	0.12 (18)	0.12 (18)	0.16 (18)	0.26 (14)
[Ti I/Fe]	0.17 (18)	0.11 (18)	0.14 (18)	0.26 (12)
[Ti II/Fe]	0.15 (18)	0.13 (18)	0.21 (18)	0.14 (14)
[Cr/Fe]	0.08 (18)	0.06 (18)	0.06 (18)	0.17 (14)
[Mn/Fe]	0.20 (18)	0.13 (18)	0.24 (8)	0.24 (13)
[Co/Fe]	0.21 (18)	0.16 (18)	0.21 (18)	0.19 (14)
[Ni/Fe]	0.13 (18)	0.14 (18)	0.15 (18)	0.34 (13)
[Zn/Fe]	0.24 (16)	0.19 (18)
[Sr/Fe]	0.83 (18)	0.72 (17)	0.47 (7)	0.80 (14)
[Ba/Fe] ^a	0.85 (17)	0.81 (17)	...	0.71 (11)

^a Includes [Ba/Fe] from McWilliam (1998)

in its ionized state, are lower in CS 22892–052 when compared with previous results (Sneden et al. 1994, 1996, 2003, 2009; McWilliam et al. 1995b; Honda et al. 2004b; Barklem et al. 2005; François et al. 2007). For example, our derived [Eu/Fe] ratios are lower by 0.20 dex ($\sigma = 0.07$) on average. Figure 21 illustrates that our derived ratios among the neutron-capture elements in CS 22892–052 are in very good agreement with the previous studies. In other words, there is generally a constant offset between our [X/Fe] ratios and those of Sneden et al. and François et al. (The [X/Fe] ratios derived by François et al. are also systematically lower than those derived by Sneden et al. by about half as much as ours.) Our results for CS 31082–001, another giant with a high level of r -process enrichment, exhibit a similar offset with respect to Hill et al. (2002), Sneden et al. (2009), and others. Our derived abundance ratios for well-studied giants with sub-solar [Eu/Fe] ratios, like HD 122563 and HD 128279, are similarly low (cf., e.g., Johnson 2002).

The explanation for this offset is the cumulative effect of several differences between our study and previous ones, and we demonstrate this using the Sneden et al. (2003) analysis of CS 22892–052. For this test, we adopt the model preferred by Sneden et al., their Fe II EW measurements, their $\log gf$ values, their solar abundances, and we only consider the four Eu II lines in common with our study. Using the appropriate earlier version of MOOG, we derive $[\text{Fe}/\text{H}] = -3.09$ from Fe II lines (identical to Sneden et al.) and $[\text{Eu}/\text{Fe}] = +1.57$ from our spectrum. This is 0.22 dex higher than our result, and it is in much better agreement with the value derived by Sneden et al., +1.64. The remaining difference must be attributed to their higher-quality spectrum of CS 22892–052.

In summary, the abundance differences can be attributed to different, but reasonable, choices made during

the course of the each analysis.

9.5. Abundance Trends with Effective Temperature

Figures 22 through 51 illustrate the relationship between the derived abundances and T_{eff} for most species examined. Each of these figures is subdivided into four panels, one each for the four classes of stars in our study. Similar comparisons for Ga I, Rb I, Nb II, Mo I, Tc I, Ru I, Sn I, Ir I, and Pb I are generally comprised of uninteresting upper limits. Similar comparisons for most of the rare earth elements, Hf II, and Th II closely resemble the La II and Eu II abundances shown in Figures 49 and 50.

Many of these species show no [X/Fe] trends with T_{eff} (where X stands for the element of interest). The [Ca/Fe] ratios shown in Figure 31, for example, demonstrate this scenario. Other species show a false trend in that lines of species of low abundance can only be detected in the coolest stars. The [Eu/Fe] ratios shown in Figure 50, for example, demonstrate this scenario. Other species show a real trend that relates to internal mixing during the course of normal stellar evolution. The lithium abundances and [C/Fe] ratios shown in Figures 22 and 23, for example, demonstrate this scenario.

Other species show genuine abundance trends with T_{eff} , including Si I, Ti I, Cr I, Co I, and—to a lesser degree—O I, Sc II, V I, V II, Mn I, and Mn II. Several of these trends are apparent in stars along the subgiant and red giant branches as well as the horizontal branch, suggesting it is not related to internal mixing or processing. Preston et al. (2006a) identified such an effect for Si I. Lai et al. (2008) also identified these trends in Si I, Ti I, and Cr I, although their study also found that Ti I and Ti II both show a trend with T_{eff} , while our Ti II abundances show no such trend.

The silicon abundance trend is characterized as show-

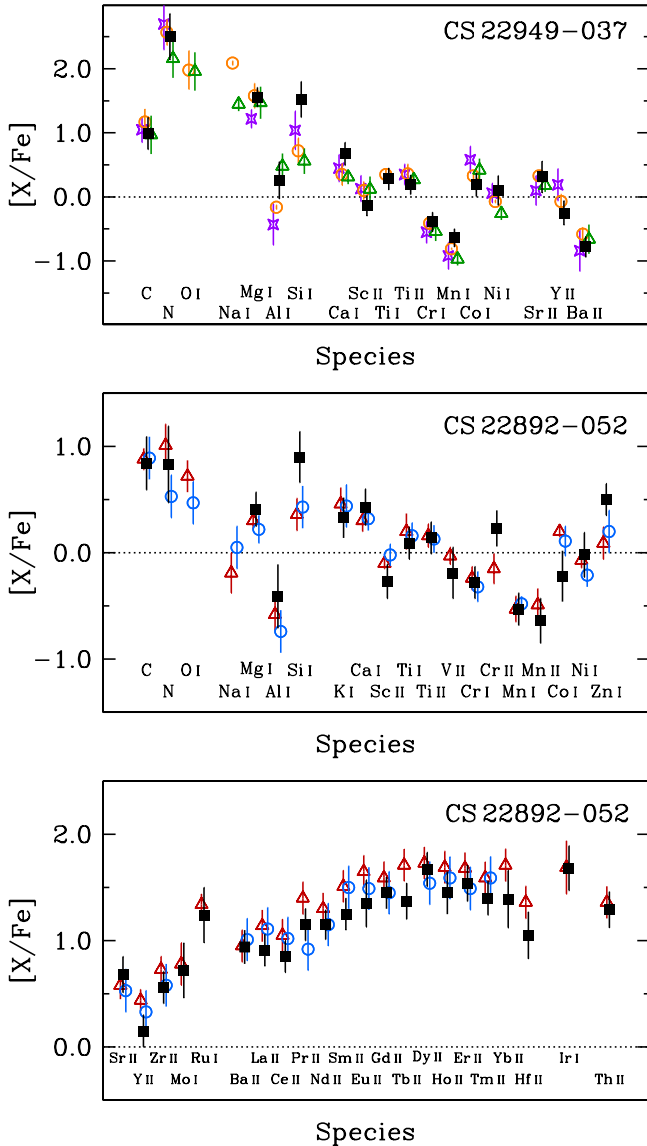


FIG. 21.— Comparison of our derived $[X/Fe]$ ratios with previous work for two well-studied stars, CS 22949–037 and CS 22892–052. In the top panel, our results (black squares) are compared with those of Norris et al. (2001) (purple stars), Depagne et al. (2002) (orange circles), and Cohen et al. (2008) (green triangles). In the middle and bottom panels, our results are compared with those of Sneden et al. (2003, 2009) and Cowan et al. (2005) (red triangles) as well as Cayrel et al. (2004) and François et al. (2007) (blue circles).

ing higher abundances at lower temperatures. The silicon abundance is derived mostly from a single Si I line at 3905 Å, so an unidentified blend that grows stronger in cooler stars could, in principle, explain this effect. Preston et al. (2006a) examined whether known CH molecular features could account for this extra absorption and concluded that this could bias the silicon abundance by a few percent at most, which is far insufficient to explain the observations. The non-LTE calculations of Shi et al. (2009) suggest that the use of LTE could account for part of the discrepancy when using the Si I 3905 Å line, but this matter is not fully resolved at present.

The oxygen trend with T_{eff} goes in the same direction, but the oxygen abundance is usually derived from the

O I triplet at 7771, 7774, and 7775 Å. At these wavelengths, line contamination is unlikely. We have corrected our O I triplet abundances for departures from LTE according to the prescriptions of Fabbian et al. (2009). These corrections, while certainly better than a pure LTE analysis, may still be imperfect, and in a few cases our stars span a wider parameter range than their grid ($4500 \leq T_{\text{eff}} \leq 6500$ K, $2.0 \leq \log g \leq 5.0$, $-3.0 \leq [Fe/H] \leq 0$). Given that the trend is mostly seen for warm subgiants that do fall within the grid, this explanation alone hardly seems adequate.

The Sc II, Ti I, V I, V II, Cr I, Mn I, Mn II, and Co I trends all run in the opposite sense from the Si I and O I trends. Most of these species are derived from many lines: the median number of lines used in the analysis for Ti I, Cr I, Mn I, Mn II, and Co I is eight, five, three, three, and three, respectively. V I and V II are each derived from one or two lines. For a trend of decreasing average abundance with decreasing T_{eff} , however, contamination by a molecular feature can be excluded. Thus it seems that the cause of the correlation in these cases is not unidentified blends.

We have included hfs components in our syntheses for all odd- Z iron group species except V II, for which we are unable to locate published values for the hyperfine A and B constants for the levels of interest. In principle, this could lead to an overestimate of the V II abundance, especially for stars with stronger absorption lines. We have simulated possible ranges of broadening for the V II lines up to 0.03 Å, which is larger than the broadening found for Sc II or Mn II. In a cool red giant star with EWs in the 80th percentile of strongest V II lines for our sample, where neglecting the hfs might affect the abundance most significantly, we could potentially underestimate the vanadium abundance by < 0.1 dex. Regardless, this correction goes in the wrong direction. Cooler stars with stronger absorption lines should yield higher abundances when neglecting hfs. Therefore neglecting the hfs for ^{51}V is not the source of the V II trend with T_{eff} .

In Figures 52 through 55 we show the $[\text{Ti II}/\text{Ti I}]$, $[\text{V II}/\text{V I}]$, $[\text{Cr II}/\text{Cr I}]$, and $[\text{Mn II}/\text{Mn I}]$ ratios plotted as functions of T_{eff} . We remind readers that these ratios denote the average total abundance of each element as derived from the ionized or neutral species after ionization corrections assuming LTE have been applied. None shows any trend with T_{eff} .

$[\text{Ti II}/\text{Ti I}]$ and $[\text{V II}/\text{V I}]$ show a significant trend when plotted as a function of metallicity, as shown in Figures 56 and 57. These ratios increase with increasing metallicity. This trend is present in stars in each of the different evolutionary classes, though the magnitude of the slope differs. One possible explanation is that Saha equilibrium is an inadequate description of the ionization distribution for stars in our sample. $[\text{Cr II}/\text{Cr I}]$ shows no correlation with metallicity (Figure 58), and $[\text{Mn II}/\text{Mn I}]$ shows, at most, a weak trend among the SG class only (Figure 59).

In conclusion, we cannot offer explanations for all of the non-conclusion abundance trends with T_{eff} . We urge those who wish to make use of our abundances to be careful with the species discussed in this section. One approach to mitigate the influence of these effects is to consider abundances of stars in only a limited range of T_{eff} , $[Fe/H]$,

and evolutionary state. Our sample of 313 stars is large enough that sampling narrow ranges of parameter space still provides satisfactory numbers for statistical comparison in most cases.

10. SUMMARY

This paper presents the technical details of our analysis to measure equivalent widths, radial velocities, derive model atmosphere parameters, and derive chemical abundances from hundreds of individual high resolution spectroscopic observations of metal-poor halo stars. Abundances or upper limits are reported for 53 species of 48 elements in 313 metal-poor stars. Our analysis finds 19 stars with metallicities $[\text{Fe}/\text{H}] \leq -3.5$, 84 stars with $[\text{Fe}/\text{H}] \leq -3.0$, and 210 stars with $[\text{Fe}/\text{H}] \leq -2.5$. For the stars selected from the HK Survey, the numbers of stars below these three metallicity thresholds are 15, 67, and 173, respectively. In subsequent papers, we will discuss the interpretation of these abundances regarding the chemical evolution of the Galactic halo and stellar nucleosynthesis in the early Universe. We welcome other investigators to make use of these results in their own work; a few words of caution, however, are appropriate.

First, our analysis is performed assuming that LTE holds in the line-forming layers of the photosphere. We employ static, 1D, plane-parallel model atmospheres constructed assuming LTE for a fixed set of abundances. To relax these assumptions would require substantial increases in computing power and relevant atomic data, and it is currently not practical to do so for a survey of this scale. Our results will differ, of course, from those computed using such techniques for individual stars.

Second, as discussed in detail in Section 8.3, our metallicity scale is slightly lower than that found by previous investigations of stars in common. We have derived most model atmosphere parameters by spectroscopic methods, whereas recent abundance studies of extremely metal-poor stars use a combination of photometric and spectroscopic methods to derive these quantities. A natural consequence of this approach is that our derived metallicities are, on average, lower by ≈ 0.25 dex for red giants and ≈ 0.04 dex for subgiants in common with previous studies. The mean metallicity differences are a function of the evolutionary state, as reported in Table 8.

Third, this is a biased sample, and the biases are not easily quantified. We have drawn our targets from a variety of sources, and even those selected from the HK Survey are a heterogeneous sample where stars we deem to be chemically interesting (based on previous studies) are overrepresented. Efforts to reconstruct the metallicity distribution function or estimate the frequency of carbon-enhanced stars, for example, using these data alone are not advised. Our data can be used, however, to calibrate other samples whose biases are well quantified.

Finally, some elemental ratios show a dependence on the stellar evolutionary state. For this reason, we

strongly urge users to avoid plotting abundances of all 313 stars on the same diagram when detailed comparisons are intended. Instead, the size of this sample may be exploited to minimize systematic errors arising from the analysis techniques. For example, it is possible to select stars spanning a small range of effective temperature, surface gravity, and metallicity and still obtain statistically meaningful samples. We intend to employ this strategy in our own analyses.

It is a pleasure to thank so many of our friends and colleagues for encouragement and advice throughout the course of this project, especially T. Beers and A. McWilliam. We appreciate the patience of the Magellan and McDonald TAC members. I.U.R. also thanks D. Fabbian, K. Lind, A. McWilliam, and Y. Takeda for providing their interpolation codes, J. Lawler and M. Wood for sending results in advance of publication, J. Sobek for assistance with abundance comparisons and MOOG installations, the referees for their diligent readings of the manuscript, and T. Beers for commenting on portions of an earlier version of the manuscript. We also thank G. Schwarz for generating the machine-readable tables included with this arXiv submission.

This research has made use of NASA's Astrophysics Data System Bibliographic Services, the arXiv preprint server operated by Cornell University, the SIMBAD and VizieR databases hosted by the Strasbourg Astronomical Data Center, and the Atomic Spectra Database hosted by the National Institute of Standards and Technology. Our appreciation for the reliability of these data archives cannot be understated. IRAF is distributed by the National Optical Astronomy Observatories, which are operated by the Association of Universities for Research in Astronomy, Inc., under cooperative agreement with the National Science Foundation. This publication makes use of data products from the Two Micron All Sky Survey, which is a joint project of the University of Massachusetts and the Infrared Processing and Analysis Center/California Institute of Technology, funded by the National Aeronautics and Space Administration and the National Science Foundation. The HET is a joint project of the University of Texas at Austin, the Pennsylvania State University, Stanford University, Ludwig-Maximilians-Universität München, and Georg-August-Universität Göttingen. The HET is named in honor of its principal benefactors, William P. Hobby and Robert E. Eberly.

I.U.R. acknowledges support by the Barbara McClintock Fellowship from the Carnegie Institution for Science. C.S. acknowledges support by the U.S. National Science Foundation (grants AST 06-07708, AST 09-08978, and AST 12-11585).

Facilities: HET (HRS), Magellan:Baade (MIKE), Magellan:Clay (MIKE), Smith (Tull)

APPENDIX

REFERENCES

- Aldenius, M., Tanner, J. D., Johansson, S., Lundberg, H., & Ryan, S. G. 2007, *A&A*, 461, 767
- Aldenius, M., Lundberg, H., & Blackwell-Whitehead, R. 2009, *A&A*, 502, 989

- Alonso, A., Arribas, S., & Martínez-Roger, C. 1999a, *A&AS*, 139, 335
- Alonso, A., Arribas, S., & Martínez-Roger, C. 1999b, *A&AS*, 140, 261
- Aoki, W., Norris, J. E., Ryan, S. G., Beers, T. C., & Ando, H. 2002a, *ApJ*, 567, 1166
- Aoki, W., Norris, J. E., Ryan, S. G., Beers, T. C., & Ando, H. 2002b, *ApJ*, 576, L141
- Aoki, W., Ryan, S. G., Norris, J. E., et al. 2002c, *ApJ*, 580, 1149
- Aoki, W., Honda, S., Beers, T. C., et al. 2005, *ApJ*, 632, 611
- Aoki, W., Beers, T. C., Christlieb, N., Norris, J. E., Ryan, S. G., & Tsangarides, S. 2007, *ApJ*, 655, 492
- Aoki, W., Beers, T. C., Sivarani, T., et al. 2008, *ApJ*, 678, 1351
- Aoki, W., Barklem, P. S., Beers, T. C., Christlieb, N., Inoue, S., García Pérez, A. E., Norris, J. E., & Carollo, D. 2009, *ApJ*, 698, 1803
- Aoki, W., Beers, T. C., Lee, Y. S., et al. 2013, *AJ*, 145, 13
- Asplund, M. 2005, *ARA&A*, 43, 481
- Asplund, M., Grevesse, N., Sauval, A. J., & Scott, P. 2009, *ARA&A*, 47, 481
- Babcock, H. D., & Herzberg, L. 1948, *ApJ*, 108, 167
- Barklem, P. S., Piskunov, N., & O'Mara, B. J. 2000, *A&AS*, 142, 467
- Barklem, P. S., & Asplund-Johansson, J. 2005, *A&A*, 435, 373
- Barklem, P. S., Christlieb, N., Beers, T. C., et al. 2005, *A&A*, 439, 129
- Beers, T. C., Preston, G. W., & Shectman, S. A. 1985, *AJ*, 90, 2089
- Beers, T. C., Kage, J. A., Preston, G. W., & Shectman, S. A. 1990, *AJ*, 100, 849
- Beers, T. C., Preston, G. W., & Shectman, S. A. 1992, *AJ*, 103, 1987 (BPS92)
- Beers, T. C., & Sommer-Larsen, J. 1995, *ApJS*, 96, 175
- Beers, T. C., Chiba, M., Yoshii, Y., Platais, I., Hanson, R. B., Fuchs, B., & Rossi, S. 2000, *AJ*, 119, 2866
- Beers, T. C., & Christlieb, N. 2005, *ARA&A*, 43, 531
- Beers, T. C., Flynn, C., Rossi, S., et al. 2007, *ApJS*, 168, 128
- Beers, T. C. 2013, "CTIO 50th Anniversary Symposium," ASP Conf. Ser., in press
- Bell, R. A., Eriksson, K., Gustafsson, B., & Nordlund, A. 1976, *A&AS*, 23, 37
- Bernstein, R., Shectman, S. A., Gunnels, S. M., Mochnacki, S., & Athey, A. E. 2003, *Proc. SPIE*, 4841, 1694
- Bidelman, W. P., & MacConnell, D. J. 1973, *AJ*, 78, 687
- Biémont, E., Grevesse, N., Faires, L. M., Marsden, G., & Lawler, J. E. 1989, *A&A*, 209, 391
- Biémont, E., Garnir, H. P., Palmeri, P., Li, Z. S., & Svanberg, S. 2000, *MNRAS*, 312, 116
- Biémont, É., Blagoev, K., Engström, L., et al. 2011, *MNRAS*, 414, 3350
- Bohlin, R. C., Hill, J. K., Jenkins, E. B., et al. 1983, *ApJS*, 51, 277
- Bond, H. E. 1970, *ApJS*, 22, 117
- Bond, H. E. 1980, *ApJS*, 44, 517
- Bonifacio, P., Molaro, P., Beers, T. C., & Vladilo, G. 1998, *A&A*, 332, 672
- Bonifacio, P., Centurion, M., & Molaro, P. 1999, *MNRAS*, 309, 533
- Bonifacio, P., Monai, S., & Beers, T. C. 2000, *AJ*, 120, 2065
- Bonifacio, P., Molaro, P., Sivarani, T., et al. 2007, *A&A*, 462, 851
- Bonifacio, P., Spite, M., Cayrel, R., et al. 2009, *A&A*, 501, 519
- Bonifacio, P., Sbordone, L., Caffau, E., et al. 2012, *A&A*, 542, A87
- Bouwens, R. J., Illingworth, G. D., Franx, M., & Ford, H. 2007, *ApJ*, 670, 928
- Caffau, E., Bonifacio, P., François, P., et al. 2011, *A&A*, 534, A4
- Cardelli, J. A., Clayton, G. C., & Mathis, J. S. 1989, *ApJ*, 345, 245
- Cardon, B. L., Smith, P. L., Scalo, J. M., & Testerman, L. 1982, *ApJ*, 260, 395
- Carney, B. W. 1979, *ApJ*, 233, 211
- Carney, B. W., & Aaronson, M. 1979, *AJ*, 84, 867
- Carney, B. W. 1983, *AJ*, 88, 610
- Carney, B. W., & Latham, D. W. 1986, *AJ*, 92, 60
- Carney, B. W., Latham, D. W., Laird, J. B., & Aguilar, L. A. 1994, *AJ*, 107, 2240
- Carney, B. W., Latham, D. W., Stefanik, R. P., Laird, J. B., & Morse, J. A. 2003, *AJ*, 125, 293
- Carney, B. W., Latham, D. W., Stefanik, R. P., & Laird, J. B. 2008, *AJ*, 135, 196
- Carretta, E., Gratton, R., Cohen, J. G., Beers, T. C., & Christlieb, N. 2002, *AJ*, 124, 481
- Castelli, F., & Kurucz, R. L. *Proc. IAU Symp. No 210, Modelling of Stellar Atmospheres*, eds. N. Piskunov et al. 2003, A20 (arXiv:0405087)
- Cayrel, R., Hill, V., Beers, T. C., et al. 2001, *Nature*, 409, 691
- Cayrel, R., Depagne, E., Spite, M., et al. 2004, *A&A*, 416, 1117
- Chang, T. N., & Tang, X. 1990, *J. Quant. Spec. Radiat. Transf.*, 43, 207
- Christlieb, N., Schörck, T., Frebel, A., Beers, T. C., Wisotzki, L., & Reimers, D. 2008, *A&A*, 484, 721
- Cohen, J. G., Christlieb, N., Beers, T. C., Gratton, R., & Carretta, E. 2002, *AJ*, 124, 470
- Cohen, J. G., Christlieb, N., McWilliam, A., et al. 2004, *ApJ*, 612, 1107
- Cohen, J. G., McWilliam, A., Shectman, S., et al. 2006, *AJ*, 132, 137
- Cohen, J. G., Christlieb, N., McWilliam, A., et al. 2008, *ApJ*, 672, 320
- Collet, R., Asplund, M., & Trampedach, R. 2007, *A&A*, 469, 687
- Cooke, R., Pettini, M., Steidel, C. C., Rudie, G. C., & Nissen, P. E. 2011, *MNRAS*, 417, 1534
- Cowan, J. J., Sneden, C., Beers, T. C., et al. 2005, *ApJ*, 627, 238
- Creevey, O. L., Thévenin, F., Boyajian, T. S., et al. 2012, *A&A*, 545, A17
- Demarque, P., Woo, J.-H., Kim, Y.-C., & Yi, S. K. 2004, *ApJS*, 155, 667
- Den Hartog, E. A., Lawler, J. E., Sneden, C., & Cowan, J. J. 2003, *ApJS*, 148, 543
- Den Hartog, E. A., Lawler, J. E., Sneden, C., & Cowan, J. J. 2006, *ApJS*, 167, 292
- Den Hartog, E. A., Lawler, J. E., Sobek, J. S., Sneden, C., & Cowan, J. J. 2011, *ApJS*, 194, 35
- Deng, L.-C., Newberg, H. J., Liu, C., et al. 2012, *Research in Astronomy and Astrophysics*, 12, 735
- Depagne, E., Hill, V., Spite, M., et al. 2002, *A&A*, 390, 187
- Doerr, A., Kock, M., Kwiatkowski, M., & Werner, K. 1985, *J. Quant. Spec. Radiat. Transf.*, 33, 55
- Dotter, A., Sarajedini, A., Anderson, J., et al. 2010, *ApJ*, 708, 698
- Fabbian, D., Asplund, M., Barklem, P. S., Carlsson, M., Kiselman, D. 2009, *A&A*, 500, 1221
- Fitzpatrick, M. J., & Sneden, C. 1987, *BAAS*, 19, 1129
- François, P., Depagne, E., Hill, V., et al. 2007, *A&A*, 476, 935
- Frebel, A., Collet, R., Eriksson, K., Christlieb, N., Aoki, W. 2008a, *ApJ*, 684, 588
- Frebel, A., Allende Prieto, C., Roederer, I. U., et al. 2008b, *New Horizons in Astronomy*, 393, 203
- Frebel, A., Casey, A. R., Jacobson, H. R., & Yu, Q. 2013, *ApJ*, 769, 57
- Fuhr, J. R. & Wiese, W. L. 2009, *Atomic Transition Probabilities*, published in the CRC Handbook of Chemistry and Physics, 90th Edition, ed. Lide, D. R., CRC Press, Inc., Boca Raton, FL, 10-93
- Fulbright, J. P. 2000, *AJ*, 120, 1841
- Fulbright, J. P. 2002, *AJ*, 123, 404
- Fulbright, J. P., Wyse, R. F. G., Ruchti, G. R., et al. 2010, *ApJ*, 724, L104
- García Pérez, A. E., Asplund, M., Primas, F., Nissen, P. E., Gustaffson, B. 2006, *A&A*, 451, 621
- Giclas, H. L., Burnham, R., & Thomas, N. G. 1971, "Lowell proper motion survey Northern Hemisphere. The G numbered stars. 8991 stars fainter than magnitude 8 with motions $\dot{\alpha}$ 0".26/year." Flagstaff, Arizona: Lowell Observatory
- Giclas, H. L., Burnham, R., Jr., & Thomas, N. G. 1978, *Lowell Observatory Bulletin*, 8, 89
- Gilroy, K. K., Sneden, C., Pilachowski, C. A., & Cowan, J. J. 1988, *ApJ*, 327, 298
- Giridhar, S., Lambert, D. L., Gonzalez, G., & Pandey, G. 2001, *PASP*, 113, 519
- González Hernández, J. I., & Bonifacio, P. 2009, *A&A*, 497, 497
- Gratton, R. G., & Sneden, C. 1988, *A&A*, 204, 193
- Gratton, R. G., & Sneden, C. 1991, *A&A*, 241, 501
- Gratton, R. G., & Sneden, C. 1994, *A&A*, 287, 927

- Gratton, R. G., Carretta, E., & Castelli, F. 1996, *A&A*, 314, 191
- Gratton, R. G., Carretta, E., Desidera, S., et al. 2003, *A&A*, 406, 131
- Griffin, R., & Griffin, R. 1973, *MNRAS*, 162, 255
- Gustafsson, B., Edvardsson, B., Eriksson, K., Jørgensen, U. G., Nordlund, Å., & Plez, B. 2008, *A&A*, 486, 951
- Harris, D. L., III, & Uggren, A. R. 1964, *ApJ*, 140, 151
- Hartmann, K., & Gehren, T. 1988, *A&A*, 199, 269
- Hill, V., Plez, B., Cayrel, R., et al. 2002, *A&A*, 387, 560
- Hinkle, K., Wallace, L., Valenti, J., & Harmer, D. 2000, *Visible and Near Infrared Atlas of the Arcturus Spectrum 3727-9300 Å*, ed. K. Hinkle, L. Wallace, J. Valenti, D. Harmer. (San Francisco: ASP)
- Hollek, J. K., Frebel, A., Roederer, I. U., et al. 2011, *ApJ*, 742, 54
- Honda, S., Aoki, W., Ando, H., et al. 2004a, *ApJS*, 152, 113
- Honda, S., Aoki, W., Kajino, T., Ando, H., Beers, T. C., Izumiura, H., Sadakane, K., & Takada-Hidai, M. 2004b, *ApJ*, 607, 474
- Ishigaki, M., Chiba, M., & Aoki, W. 2010, *PASJ*, 62, 143
- Ito, H., Aoki, W., Beers, T. C., et al. 2013, *ApJ*, 773, 33
- Ivans, I. I., Sneden, C., James, C. R., Preston, G. W., Fulbright, J. P., Höflich, P. A., Carney, B. W., & Wheeler, J. C. 2003, *ApJ*, 592, 906
- Ivans, I. I., Sneden, C., Gallino, R., Cowan, J. J., & Preston, G. W. 2005, *ApJ*, 627, L145
- Ivans, I. I., Simmerer, J., Sneden, C., Lawler, J. E., Cowan, J. J., Gallino, R., & Bisterzo, S. 2006, *ApJ*, 645, 613
- Ivarsson, S., Andersen, J., Nordström, B., et al. 2003, *A&A*, 409, 1141
- Johnson, J. A. 2002, *ApJS*, 139, 219
- Johnson, J. A., Herwig, F., Beers, T. C., & Christlieb, N. 2007, *ApJ*, 658, 1203
- Keller, S. C., SkyMapper Team, & Aegis Team. 2012, “Galactic Archaeology: Near-Field Cosmology and the Formation of the Milky Way,” 458, 409
- Kelson, D. D. 2003, *PASP*, 115, 688
- Kiselman, D. 2001, *New Astronomy Reviews*, 45, 559
- Kurucz, R. L., & Bell, B. 1995, *Kurucz CD-ROM*, Cambridge, MA: Smithsonian Astrophysical Observatory
- Lai, D. K., Bolte, M., Johnson, J. A., & Lucatello, S. 2004, *AJ*, 128, 2402
- Lai, D. K., Bolte, M., Johnson, J. A., Lucatello, S., Heger, A., & Woosley, S. E. 2008, *ApJ*, 681, 1524
- Latham, D. W., Davis, R. J., Stefanik, R. P., Mazeh, T., & Abt, H. A. 1991, *AJ*, 101, 625
- Latham, D. W., Stefanik, R. P., Torres, G., Davis, R. J., Mazeh, T., Carney, B. W., Laird, J. B., & Morse, J. A. 2002, *AJ*, 124, 1144
- Lawler, J. E., & Dakin, J. T. 1989, *Journal of the Optical Society of America B Optical Physics*, 6, 1457
- Lawler, J. E., Bonvallet, G., & Sneden, C. 2001a, *ApJ*, 556, 452
- Lawler, J. E., Wickliffe, M. E., den Hartog, E. A., & Sneden, C. 2001b, *ApJ*, 563, 1075
- Lawler, J. E., Wickliffe, M. E., Cowley, C. R., & Sneden, C. 2001c, *ApJS*, 137, 341
- Lawler, J. E., Wyart, J.-F., & Blaise, J. 2001d, *ApJS*, 137, 351
- Lawler, J. E., Sneden, C., & Cowan, J. J. 2004, *ApJ*, 604, 850
- Lawler, J. E., Den Hartog, E. A., Sneden, C., & Cowan, J. J. 2006, *ApJS*, 162, 227
- Lawler, J. E., Den Hartog, E. A., Labby, Z. E., Sneden, C., Cowan, J. J., & Ivans, I. I. 2007, *ApJS*, 169, 120
- Lawler, J. E., Sneden, C., Cowan, J. J., Wyart, J.-F., Ivans, I. I., Sobek, J. S., Stockett, M. H., & Den Hartog, E. A. 2008, *ApJS*, 178, 71
- Lawler, J. E., Sneden, C., Cowan, J. J., Ivans, I. I., & Den Hartog, E. A. 2009, *ApJS*, 182, 51
- Lawler, J. E., Guzman, A., Wood, M. P., Sneden, C., & Cowan, J. J. 2013, *ApJS*, 205, 11
- Lazauskaite, R., & Tautvaisiene, G. 1990, *Vilnius Astronomijos Observatorijos Biuletenis*, 85, 30
- Lee, Y. S., Beers, T. C., Sivarani, T., et al. 2008, *AJ*, 136, 2022
- Li, R., Chatelain, R., Holt, R. A., Rehse, S. J., Rosner, S. D., & Scholl, T. J. 2007, *Phys. Scr*, 76, 577
- Lind, K., Asplund, M., & Barklem, P. S. 2009, *A&A*, 503, 541
- Lind, K., Asplund, M., Barklem, P. S., & Belyaev, A. K. 2011, *A&A*, 528, A103
- Lind, K., Bergemann, M., & Asplund, M. 2012, *MNRAS*, 427, 50
- Ljung, G., Nilsson, H., Asplund, M., & Johansson, S. 2006, *A&A*, 456, 1181
- Lucatello, S., Tsangarides, S., Beers, T. C., Carretta, E., Gratton, R. G., & Ryan, S. G. 2005, *ApJ*, 625, 825
- Luck, R. E., & Bond, H. E. 1981, *ApJ*, 244, 919
- Luck, R. E., & Bond, H. E. 1985, *ApJ*, 292, 559
- Luyten, W. J. 1979, *NLT Catalogue: Volume I. +90 to +30, Volume II. +30 to 0 (Minneapolis: Univ. Minnesota)*
- Magain, P. 1984, *A&A*, 134, 189
- Magain, P. 1989, *A&A*, 209, 211
- Matejek, M. S., & Simcoe, R. A. 2012, *ApJ*, 761, 112
- Masseron, T., Johnson, J. A., Plez, B., et al. 2010, *A&A*, 509, A93
- Masseron, T., Johnson, J. A., Lucatello, S., et al. 2012, *ApJ*, 751, 14
- McWilliam, A., Preston, G. W., Sneden, C., & Sheckman, S. 1995a, *AJ*, 109, 2736
- McWilliam, A., Preston, G. W., Sneden, C., & Searle, L. 1995b, *AJ*, 109, 2757
- McWilliam, A. 1998, *AJ*, 115, 1640
- Meléndez, J., & Barbuy, B. 2009, *A&A*, 497, 611
- Molaro, P., & Bonifacio, P. 1990, *A&A*, 236, L5
- Molaro, P., & Castelli, F. 1990, *A&A*, 228, 426
- Mucciarelli, A. 2011, *A&A*, 58, A44
- Nicolet, B. 1978, *A&AS*, 34, 1
- Nilsson, H., Zhang, Z. G., Lundberg, H., Johansson, S., & Nordström, B. 2002, *A&A*, 382, 368
- Nilsson, H., Ljung, G., Lundberg, H., & Nielsen, K. E. 2006, *A&A*, 445, 1165
- Nilsson, H., Hartman, H., Engström, L., et al. 2010, *A&A*, 511, A16
- Nitz, D. E., Kunau, A. E., Wilson, K. L., & Lentz, L. R. 1999, *ApJS*, 122, 557
- Nordström, B., et al. 2004, *A&A*, 418, 989
- Norris, J., Bessell, M. S., & Pickles, A. J. 1985, *ApJS*, 58, 463
- Norris, J. 1986, *ApJS*, 61, 667
- Norris, J. E., Peterson, R. C., & Beers, T. C. 1993, *ApJ*, 415, 797
- Norris, J. E., Ryan, S. G., & Beers, T. C. 1996, *ApJS*, 107, 391
- Norris, J. E., Ryan, S. G., & Beers, T. C. 1997, *ApJ*, 489, L169
- Norris, J. E., Ryan, S. G., & Beers, T. C. 1999, *ApJS*, 123, 639
- Norris, J. E., Ryan, S. G., & Beers, T. C. 2001, *ApJ*, 561, 1034
- Norris, J. E., Bessell, M. S., Yong, D., et al. 2013, *ApJ*, 762, 25
- O’Brian, T. R., Wickliffe, M. E., Lawler, J. E., Whaling, W., & Brault, J. W. 1991, *J. Opt. Soc. Am. B Optical Physics*, 8, 1185
- Palmeri, P., Fischer, C. F., Wyart, J.-F., & Godefroid, M. R. 2005, *MNRAS*, 363, 452
- Perryman, M. A. C., & ESA 1997, *ESA Special Publication Series*, vol. 1200
- Peterson, R. C., Kurucz, R. L., & Carney, B. W. 1990, *ApJ*, 350, 173
- Pickering, J. C., Thorne, A. P., & Perez, R. 2001, *ApJS*, 132, 403
- Pickering, J. C., Thorne, A. P., & Perez, R. 2002, *ApJS*, 138, 247
- Piskunov, N. E., & Valenti, J. A. 2002, *A&A*, 385, 1095
- Pourbaix, D., Tokovinin, A. A., Batten, A. H., et al. 2004, *A&A*, 424, 727
- Preston, G. W., Sheckman, S. A., & Beers, T. C. 1991, *ApJS*, 76, 1001
- Preston, G. W., Beers, T. C., & Sheckman, S. A. 1994, *AJ*, 108, 538
- Preston, G. W., & Sneden, C. 2000, *AJ*, 120, 1014
- Preston, G. W., & Sneden, C. 2001, *AJ*, 122, 1545
- Preston, G. W., Sneden, C., Thompson, I. B., Sheckman, S. A., & Burley, G. S. 2006a, *AJ*, 132, 85
- Preston, G. W., Thompson, I. B., Sneden, C., Stachowski, G., & Sheckman, S. A. 2006b, *AJ*, 132, 1714
- Preston, G. W. 2009, *Pub. Astron. Soc. Australia*, 26, 372
- Primas, F., Molaro, P., & Castelli, F. 1994, *A&A*, 290, 885
- Ramírez, I., & Meléndez, J. 2005, *ApJ*, 626, 446
- Ramsey, L. W., Adams, M. T., Barnes, T. G., et al. 1998, *Proc. SPIE*, 3352, 34
- Rhee, J. 2001, *PASP*, 113, 1569
- Rockosi, C. M. 2012, *BAAS*, 219, 205.01
- Roederer, I. U., Lawler, J. E., Sneden, C., et al. 2008a, *ApJ*, 675, 723
- Roederer, I. U., Frebel, A., Shetrone, M. D., et al. 2008b, *ApJ*, 679, 1549
- Roederer, I. U., Kratz, K.-L., Frebel, A., et al. 2009, *ApJ*, 698, 1963

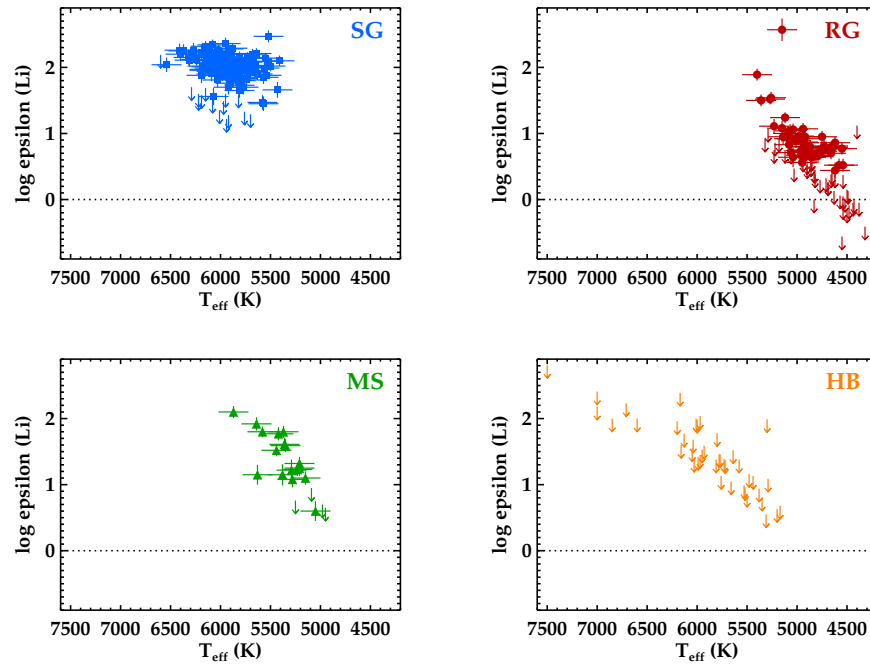


FIG. 22.— Derived lithium abundances as a function of T_{eff} . Each panel illustrates a different class of stars, and the three stars in class “BS” are included in the plot for stars in class “HB.” The 1σ uncertainties are indicated. Downward arrows indicate 3σ upper limits, and the actual value is marked by the end with no arrow head.

- Roederer, I. U., Sneden, C., Thompson, I. B., Preston, G. W., & Shectman, S. A. 2010, *ApJ*, 711, 573
- Roederer, I. U., & Lawler, J. E. 2012, *ApJ*, 750, 76
- Roederer, I. U., Lawler, J. E., Sobeck, J. S., et al. 2012, *ApJS*, 203, 27
- Roederer, I. U., Preston, G. W., Thompson, I. B., Shectman, S. A., Sneden, C. 2014, *ApJ*, 784, 158
- Rossi, S., Beers, T. C., Sneden, C., Sevastyanenko, T., Rhee, J., & Marsteller, B. 2005, *AJ*, 130, 2804
- Ryan, S. G. 1989, *AJ*, 98, 1693
- Ryan, S. G., & Norris, J. E. 1991, *AJ*, 101, 1835
- Ryan, S. G., Norris, J. E., & Bessell, M. S. 1991, *AJ*, 102, 303
- Ryan, S. G., Norris, J. E., & Beers, T. C. 1996, *ApJ*, 471, 254
- Saha, M. N. 1921, *Royal Society of London Proceedings Series A*, 99, 135
- Sandage, A. 1969, *ApJ*, 158, 1115
- Sandage, A., & Kowal, C. 1986, *AJ*, 91, 1140
- Sargent, W. L. W., Bokserberg, A., & Steidel, C. C. 1988, *ApJS*, 68, 539
- Sbordone, L., Bonifacio, P., Caffau, E., et al. 2010, *A&A*, 522, A26
- Schlegel, D. J., Finkbeiner, D. P., & Davis, M. 1998, *ApJ*, 500, 525
- Schuster, W. J., Beers, T. C., Michel, R., Nissen, P. E., & García, G. 2004, *A&A*, 422, 527
- Shetrone, M., Cornell, M. E., Fowler, J. R., et al. 2007, *PASP*, 119, 556
- Shi, J. R., Gehren, T., Mashonkina, L., & Zhao, G. 2009, *A&A*, 503, 533
- Simmerer, J., Sneden, C., Cowan, J. J., et al. 2004, *ApJ*, 617, 1091
- Sivarani, T., Beers, T. C., Bonifacio, P., et al. 2006, *A&A*, 459, 125
- Skrutskie, M. F., Cutri, R. M., Stiening, R., et al. 2006, *AJ*, 131, 1163
- Smith, V. V., Lambert, D. L., & Nissen, P. E. 1998, *ApJ*, 506, 405
- Sneden, C. A. 1973, Ph.D. Thesis, Univ. of Texas at Austin
- Sneden, C., Preston, G. W., McWilliam, A., & Searle, L. 1994, *ApJ*, 431, L27
- Sneden, C., McWilliam, A., Preston, G. W., et al. 1996, *ApJ*, 467, 819
- Sneden, C., Cowan, J. J., Lawler, J. E., et al. 2003, *ApJ*, 591, 936
- Sneden, C., Preston, G. W., & Cowan, J. J. 2003, *ApJ*, 592, 504
- Sneden, C., Cowan, J. J., Gallino, R. 2008, *ARA&A*, 46, 241
- Sneden, C., Lawler, J. E., Cowan, J. J., Ivans, I. I., & Den Hartog, E. A. 2009, *ApJS*, 182, 80
- Sobeck, J. S., Lawler, J. E., & Sneden, C. 2007, *ApJ*, 667, 1267
- Sobeck, J. S., Kraft, R. P., Sneden, C., et al. 2011, *AJ*, 141, 175
- Spite, M., Depagne, E., Nordström, B., et al. 2000, *A&A*, 360, 1077
- Spite, M., Cayrel, R., Plez, B., et al. 2005, *A&A*, 430, 655
- Stephens, A., & Boesgaard, A. M. 2002, *AJ*, 123, 1647
- Takeda, Y., Zhao, G., Chen, Y.-Q., Qiu, H.-M., & Takada-Hidai, M. 2002, *PASJ*, 54, 275
- Thévenin, F., & Idiart, T. P. 1999, *ApJ*, 521, 753
- Thompson, I. B., Ivans, I. I., Bisterzo, S., et al. 2008, *ApJ*, 677, 556
- Tsangarides, S., Ryan, S. G., & Beers, T. C. 2004, *Mem. Soc. Astron. Italiana*, 75, 772
- Tull, R. G., MacQueen, P. J., Sneden, C., & Lambert, D. L. 1995, *PASP*, 107, 251
- Tull, R. G. 1998, *Proc. SPIE*, 3355, 387
- Unsöld, A., *Physik der Sternatmosphären*, Springer-Verlag, Berlin, 1955, p. 332
- Van Eck, S., Goriely, S., Jorissen, A., & Plez, B. 2003, *A&A*, 404, 291
- van Leeuwen, F. 2007, *A&A*, 474, 653
- Whaling, W., & Brault, J. W. 1988, *Phys. Scr*, 38, 707
- Wickliffe, M. E., Salih, S., & Lawler, J. E. 1994, *J. Quant. Spec. Radiat. Transf.*, 51, 545
- Wickliffe, M. E., & Lawler, J. E. 1997, *J. Opt. Soc. Am. B Optical Physics*, 14, 737
- Wickliffe, M. E., Lawler, J. E., & Nave, G. 2000, *J. Quant. Spec. Radiat. Transf.*, 66, 363
- Wisotzki, L., Christlieb, N., Bade, N., et al. 2000, *A&A*, 358, 77
- Wood, M. P., Lawler, J. E., Sneden, C., Cowan, J. J. 2013, *ApJS*, 208, 27
- Yanny, B., Rockosi, C., Newberg, H. J., et al. 2009, *AJ*, 137, 4377
- Yong, D., Norris, J. E., Bessell, M. S., et al. 2013, *ApJ*, 762, 26
- Zhang, L., Ishigaki, M., Aoki, W., Zhao, G., & Chiba, M. 2009, *ApJ*, 706, 1095
- Zhao, G., & Magain, P. 1990, *A&A*, 238, 242

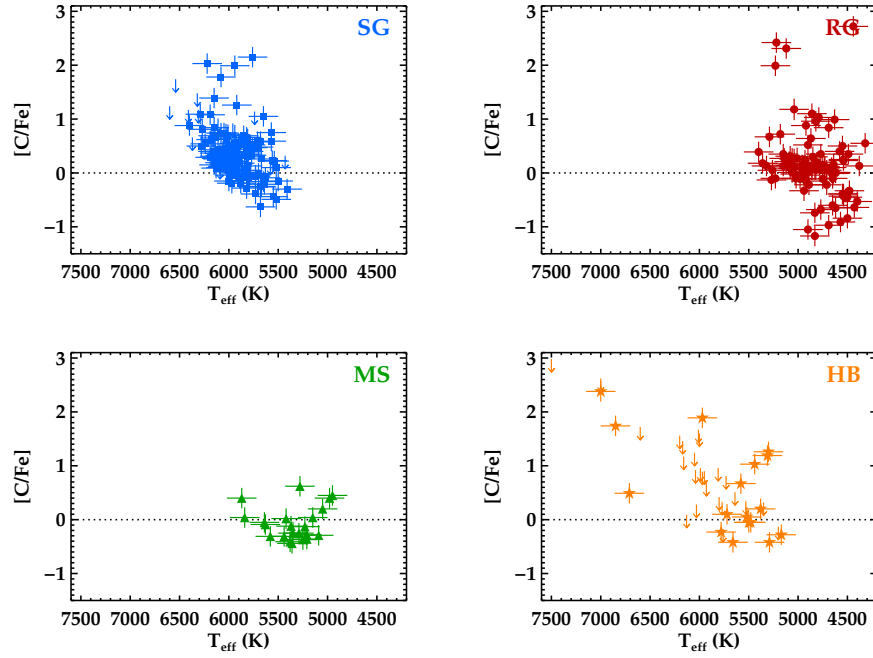


FIG. 23.— Derived $[C/Fe]$ ratios as a function of T_{eff} . The carbon abundance is derived from the CH $A^2\Delta - X^2\Pi$ G band. The dotted lines indicate the Solar ratio. All other symbols are the same as in Figure 22.

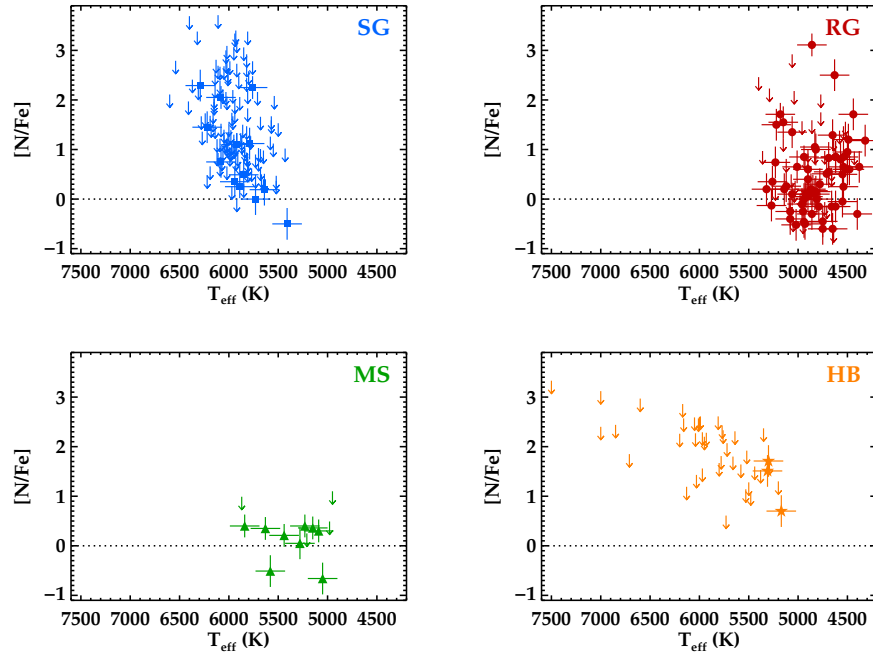


FIG. 24.— Derived $[N/Fe]$ ratios as a function of T_{eff} . The nitrogen abundance is derived from the NH $A^3\Pi - X^3\Sigma$ band or the CN $B^2\Sigma - X^2\Sigma$ band. Symbols are the same as in Figures 22 and 23.

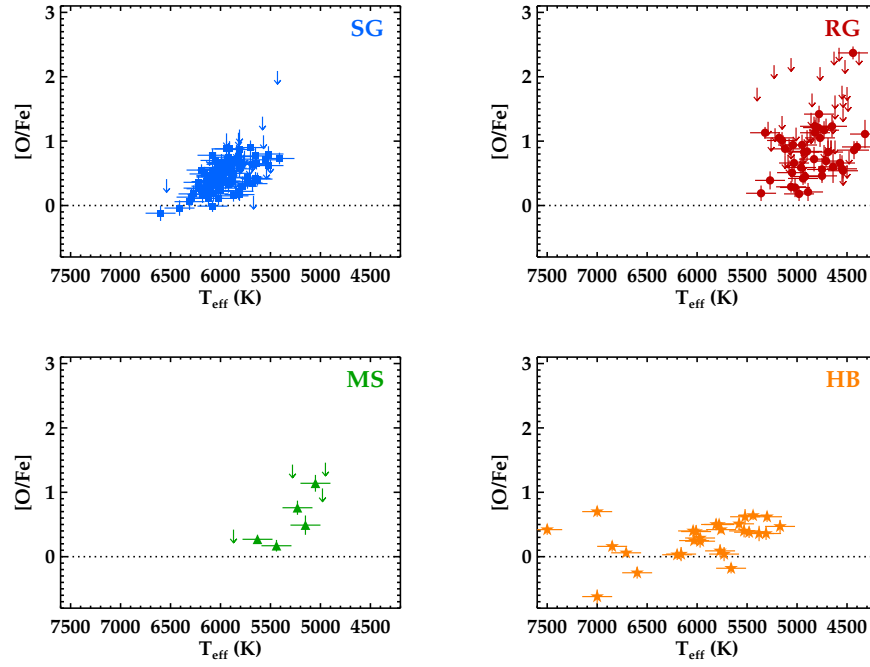


FIG. 25.— Derived $[O/Fe]$ ratios as a function of T_{eff} . Symbols are the same as in Figures 22 and 23.

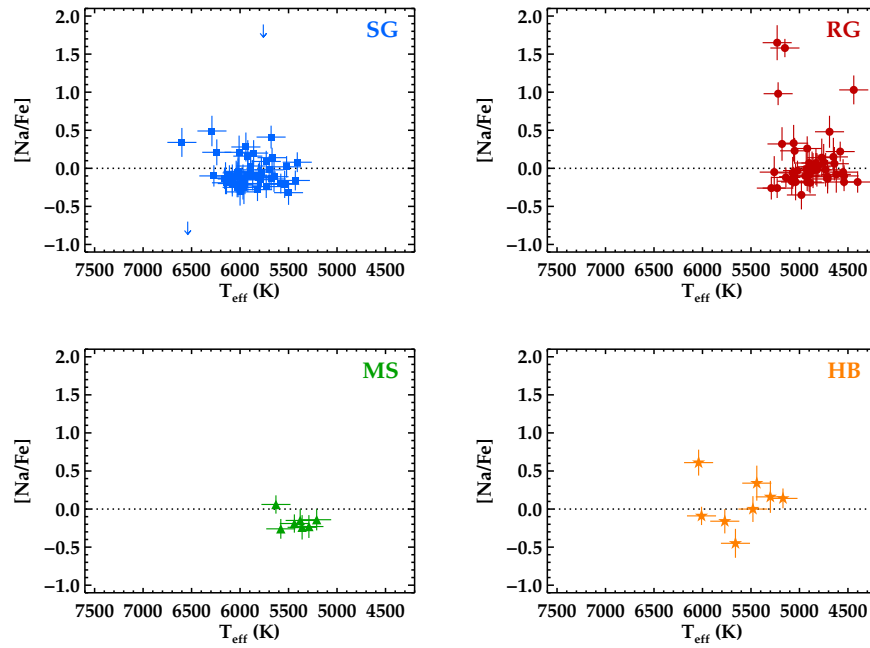


FIG. 26.— Derived $[Na/Fe]$ ratios as a function of T_{eff} . Symbols are the same as in Figures 22 and 23.

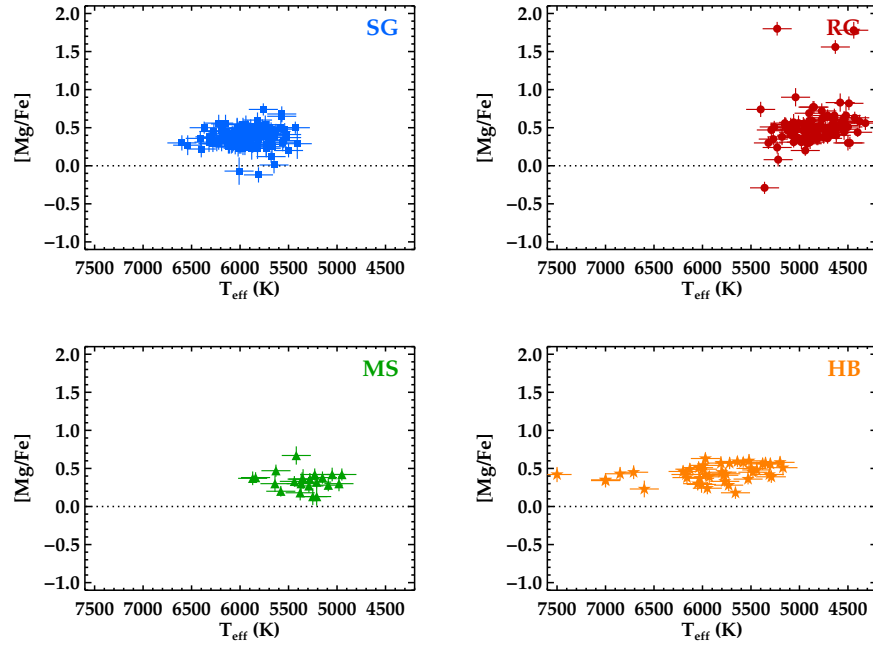


FIG. 27.— Derived $[\text{Mg}/\text{Fe}]$ ratios as a function of T_{eff} . Symbols are the same as in Figures 22 and 23.

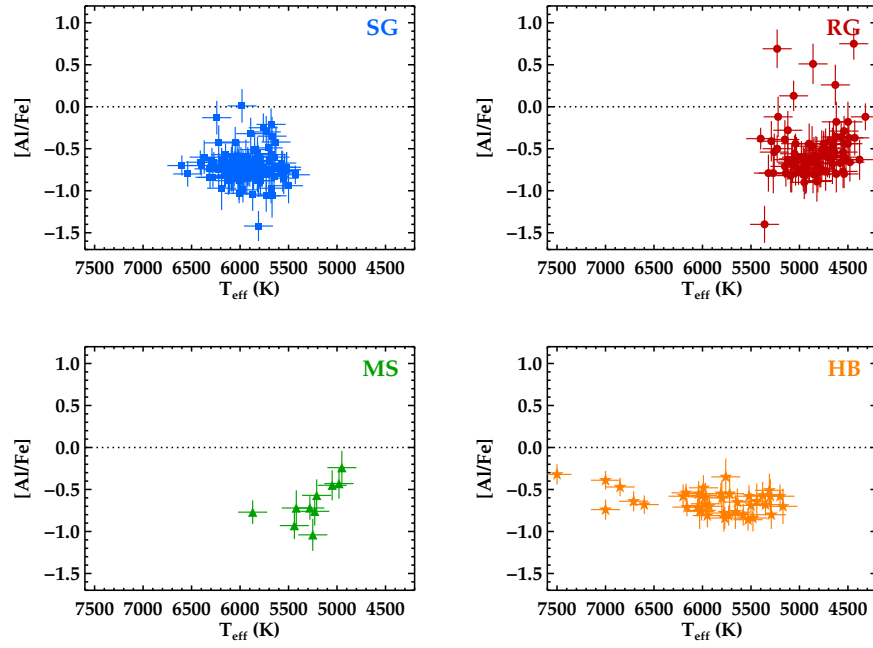


FIG. 28.— Derived $[\text{Al}/\text{Fe}]$ ratios as a function of T_{eff} . Symbols are the same as in Figures 22 and 23.

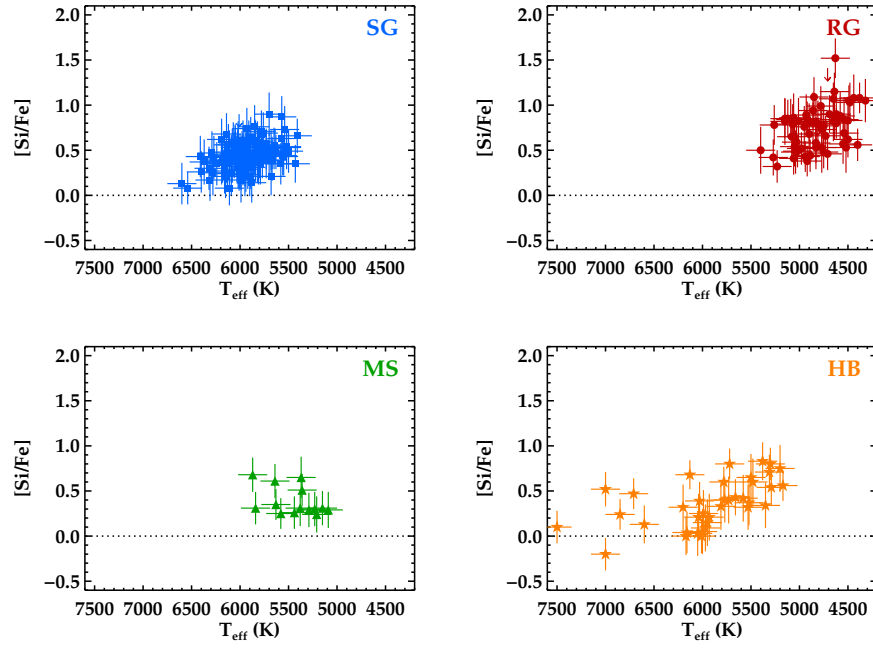


FIG. 29.— Derived $[\text{Si}/\text{Fe}]$ ratios as a function of T_{eff} . Symbols are the same as in Figures 22 and 23.

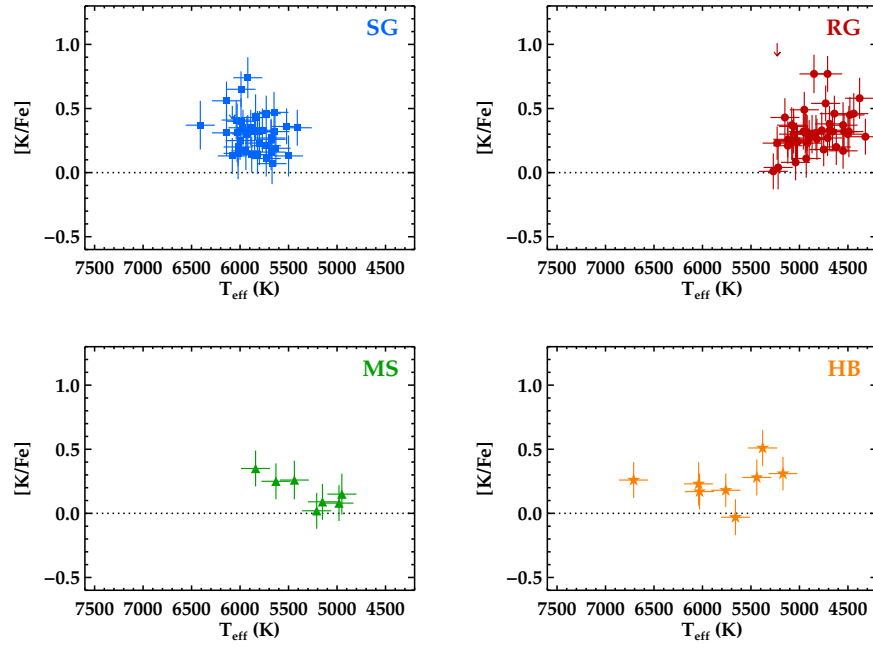


FIG. 30.— Derived $[\text{K}/\text{Fe}]$ ratios as a function of T_{eff} . Symbols are the same as in Figures 22 and 23.

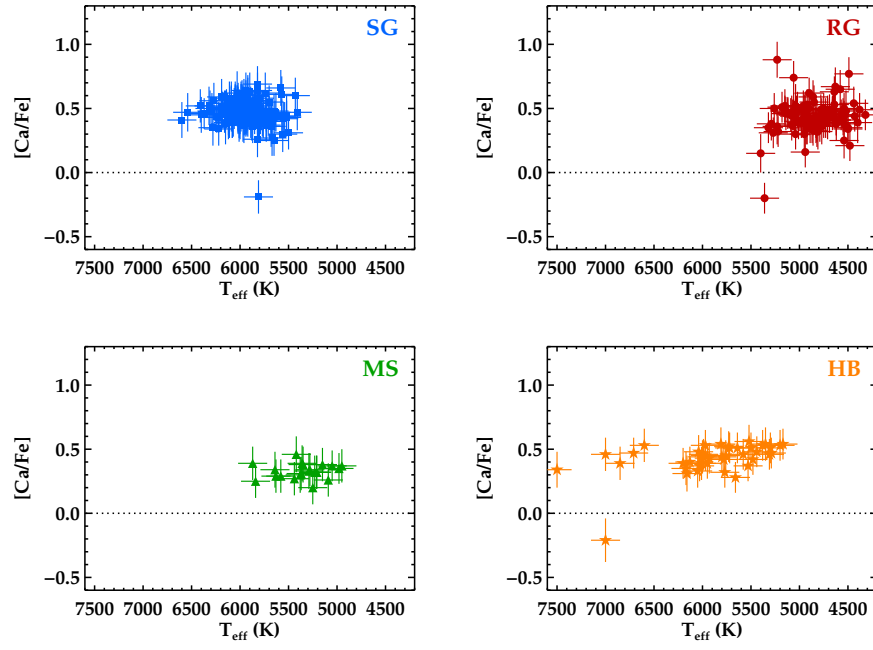


FIG. 31.— Derived $[\text{Ca}/\text{Fe}]$ ratios as a function of T_{eff} . Symbols are the same as in Figures 22 and 23.

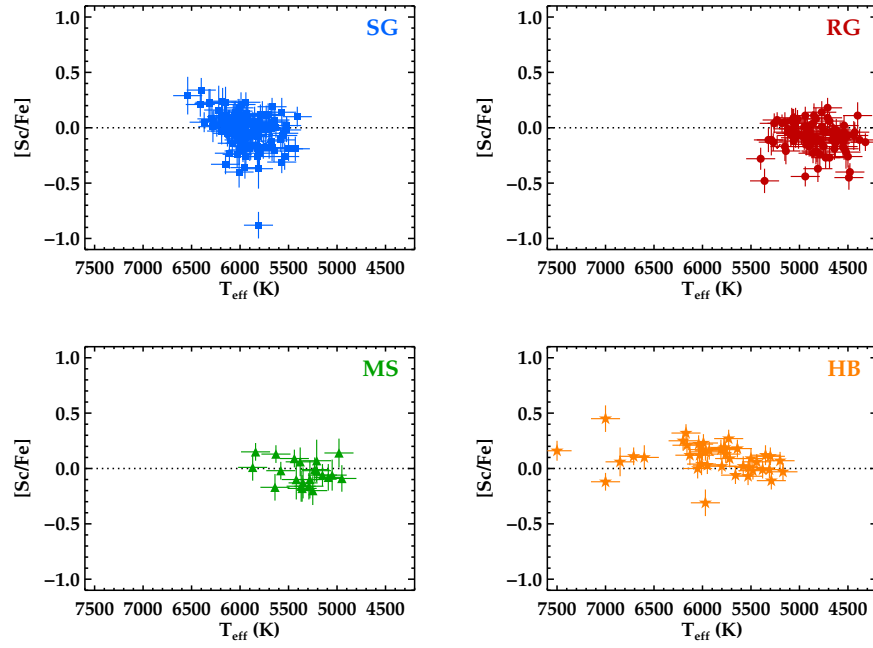


FIG. 32.— Derived $[\text{Sc}/\text{Fe}]$ ratios as a function of T_{eff} . Symbols are the same as in Figures 22 and 23.

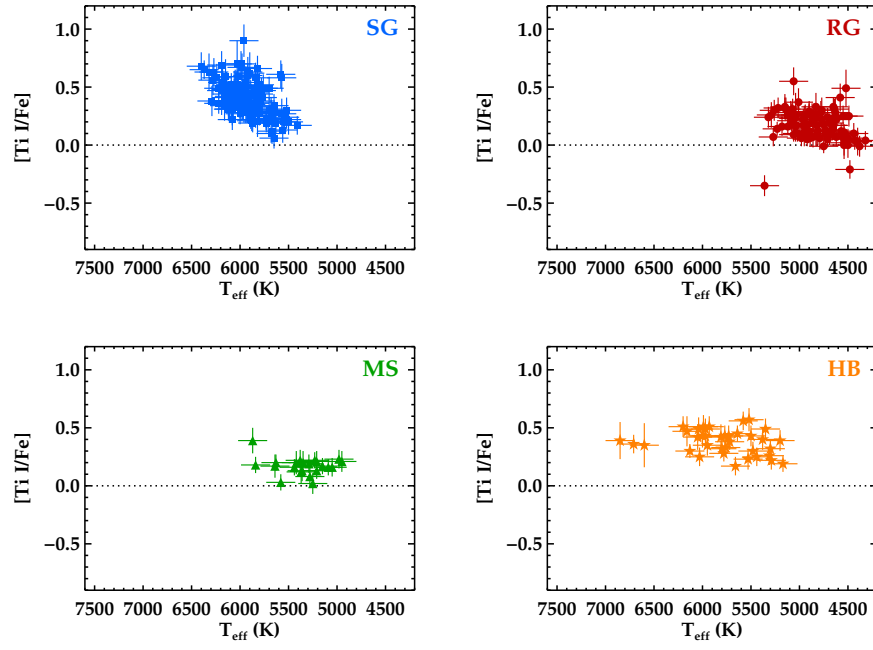


FIG. 33.— Derived $[\text{Ti I}/\text{Fe}]$ ratios for neutral lines as a function of T_{eff} . Symbols are the same as in Figures 22 and 23.

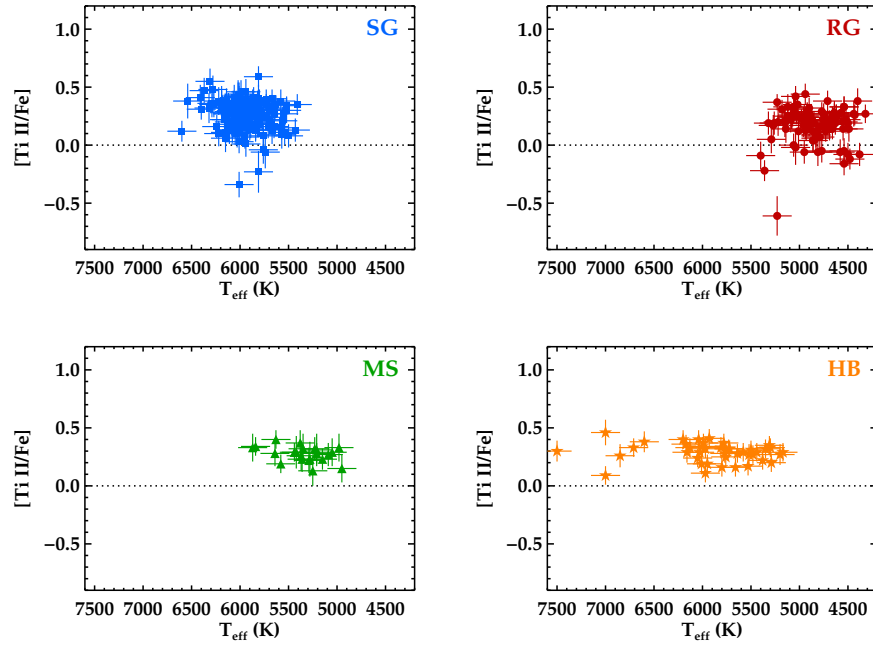


FIG. 34.— Derived $[\text{Ti II}/\text{Fe}]$ ratios for ionized lines as a function of T_{eff} . Symbols are the same as in Figures 22 and 23.

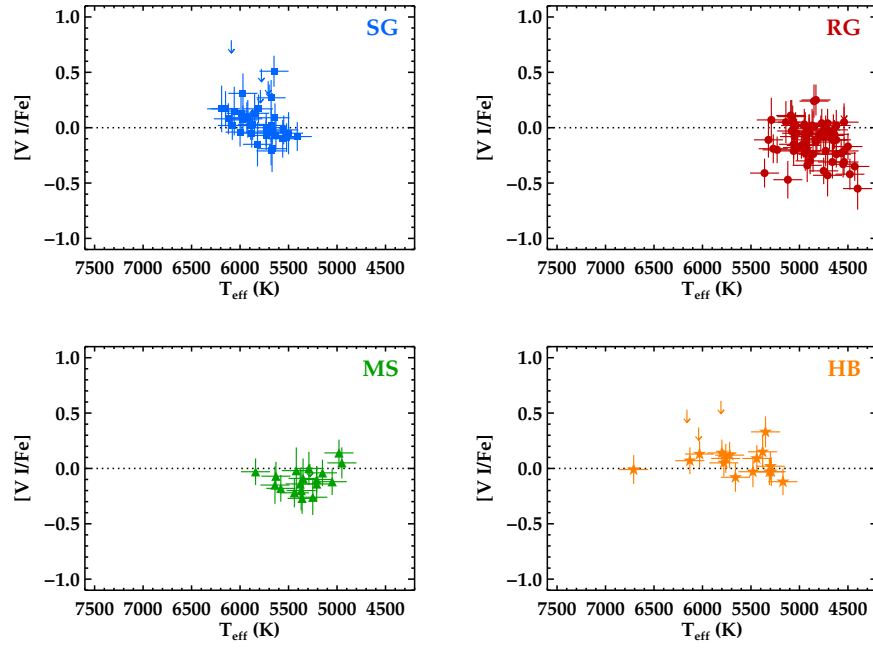


FIG. 35.— Derived $[V\ I/Fe]$ ratios for neutral lines as a function of T_{eff} . Symbols are the same as in Figures 22 and 23.

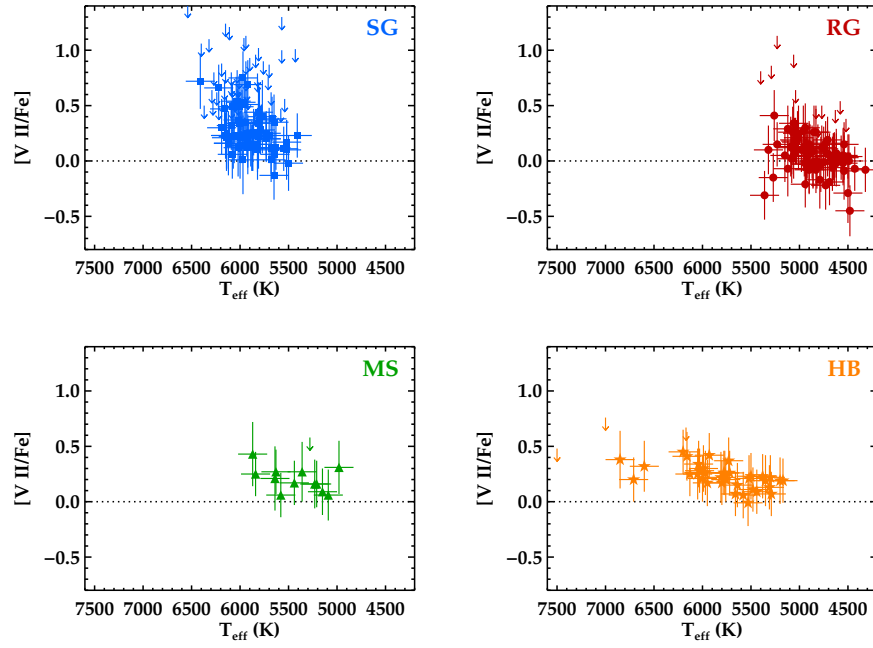


FIG. 36.— Derived $[V\ II/Fe]$ ratios for ionized lines as a function of T_{eff} . Symbols are the same as in Figures 22 and 23.

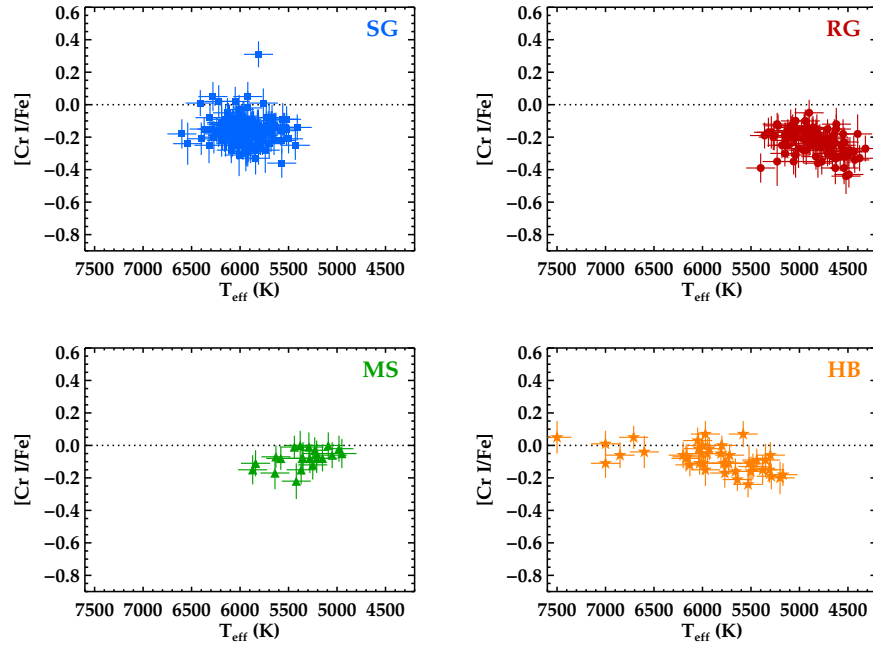


FIG. 37.— Derived $[\text{Cr I}/\text{Fe}]$ ratios for neutral lines as a function of T_{eff} . Symbols are the same as in Figures 22 and 23.

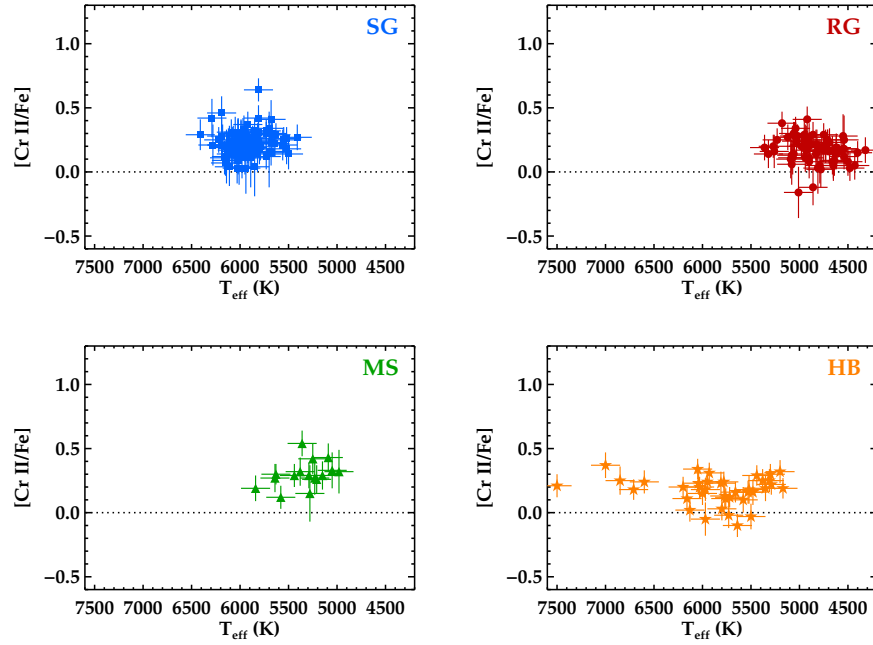


FIG. 38.— Derived $[\text{Cr II}/\text{Fe}]$ ratios for ionized lines as a function of T_{eff} . Symbols are the same as in Figures 22 and 23.

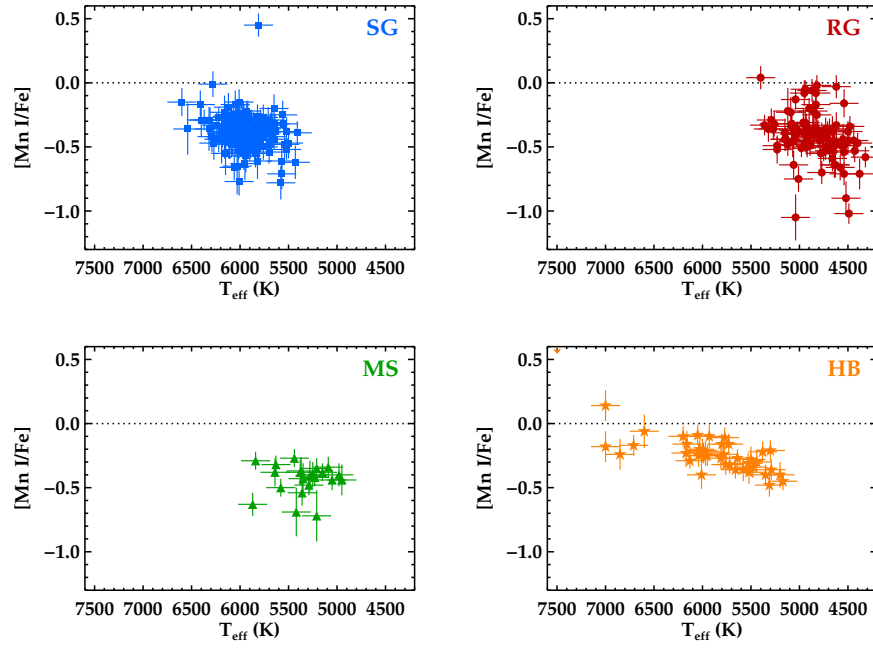


FIG. 39.— Derived $[\text{Mn I}/\text{Fe}]$ ratios for neutral lines as a function of T_{eff} . Symbols are the same as in Figures 22 and 23.

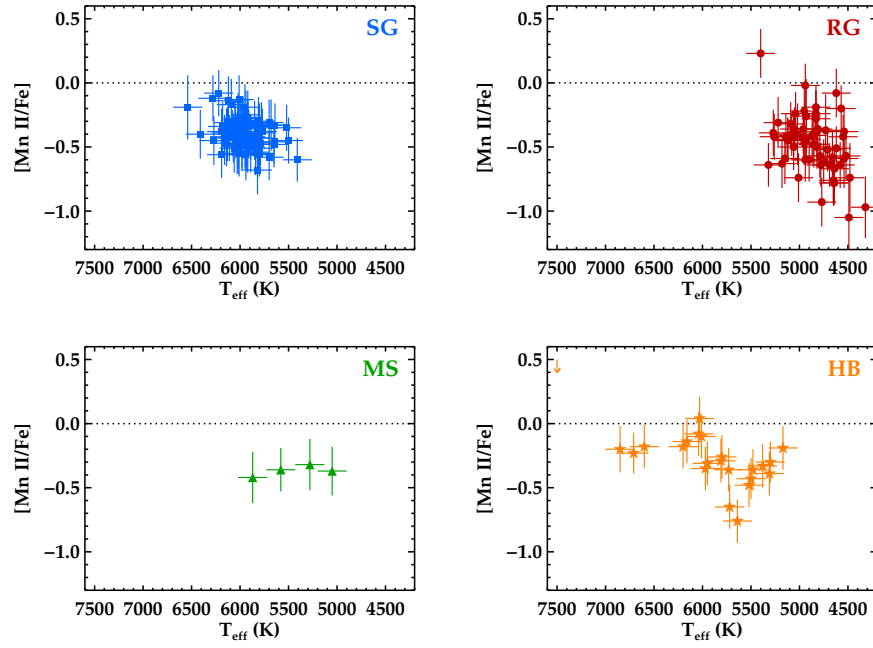


FIG. 40.— Derived $[\text{Mn II}/\text{Fe}]$ ratios for ionized lines as a function of T_{eff} . Symbols are the same as in Figures 22 and 23.

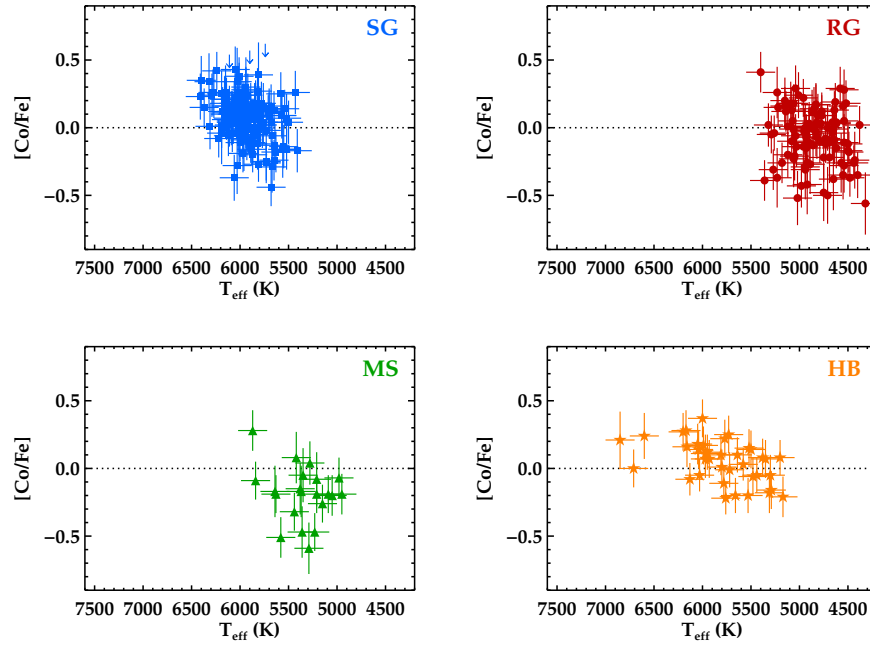


FIG. 41.— Derived $[\text{Co}/\text{Fe}]$ ratios as a function of T_{eff} . Symbols are the same as in Figures 22 and 23.

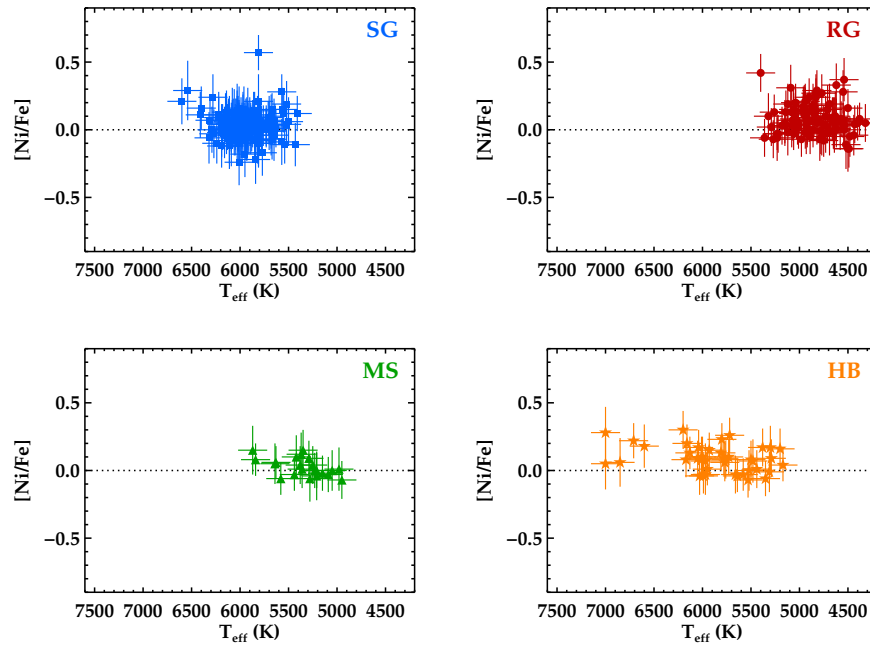


FIG. 42.— Derived $[\text{Ni}/\text{Fe}]$ ratios as a function of T_{eff} . Symbols are the same as in Figures 22 and 23.

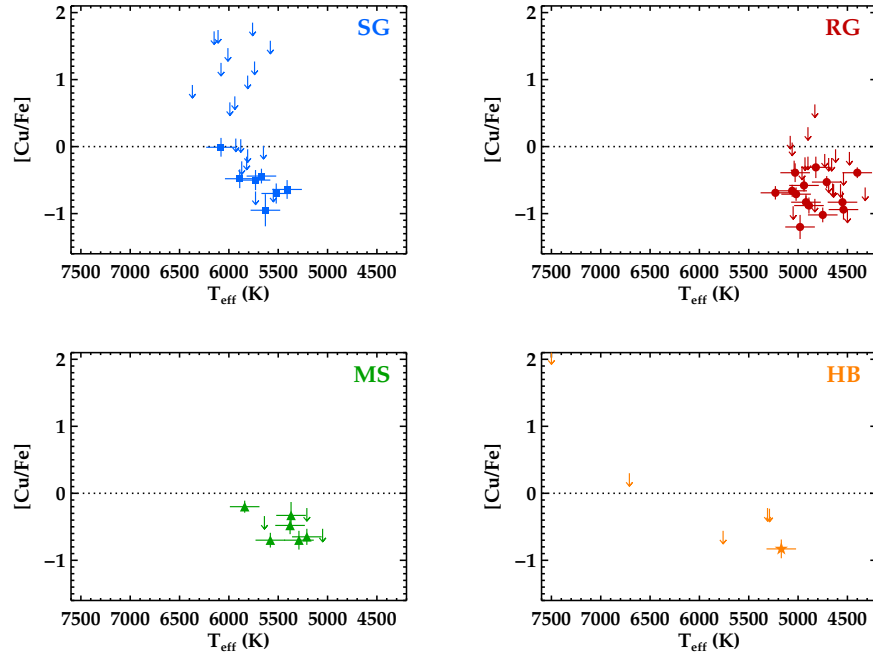


FIG. 43.— Derived $[\text{Cu}/\text{Fe}]$ ratios as a function of T_{eff} . Symbols are the same as in Figures 22 and 23.

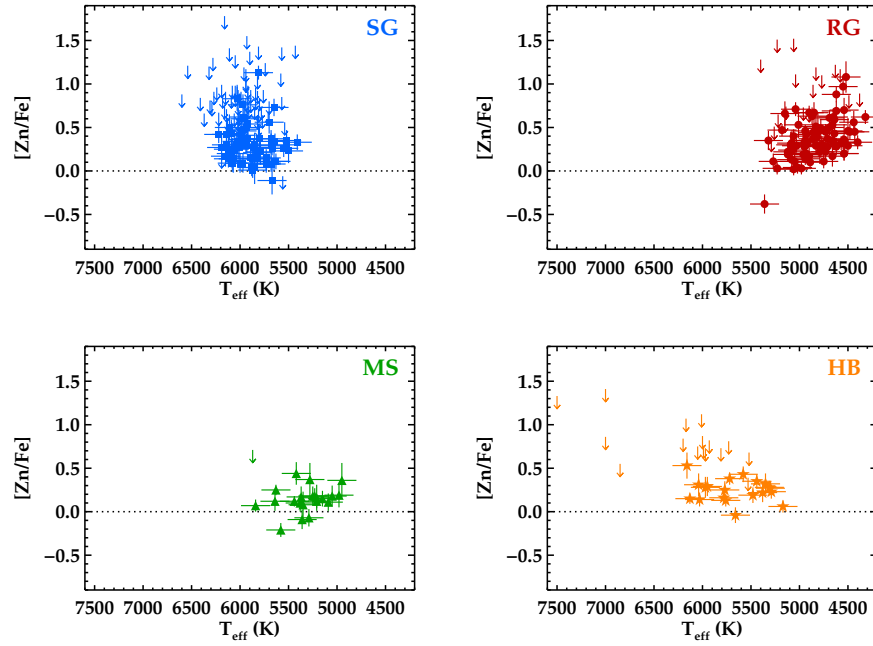


FIG. 44.— Derived $[\text{Zn}/\text{Fe}]$ ratios as a function of T_{eff} . Symbols are the same as in Figures 22 and 23.

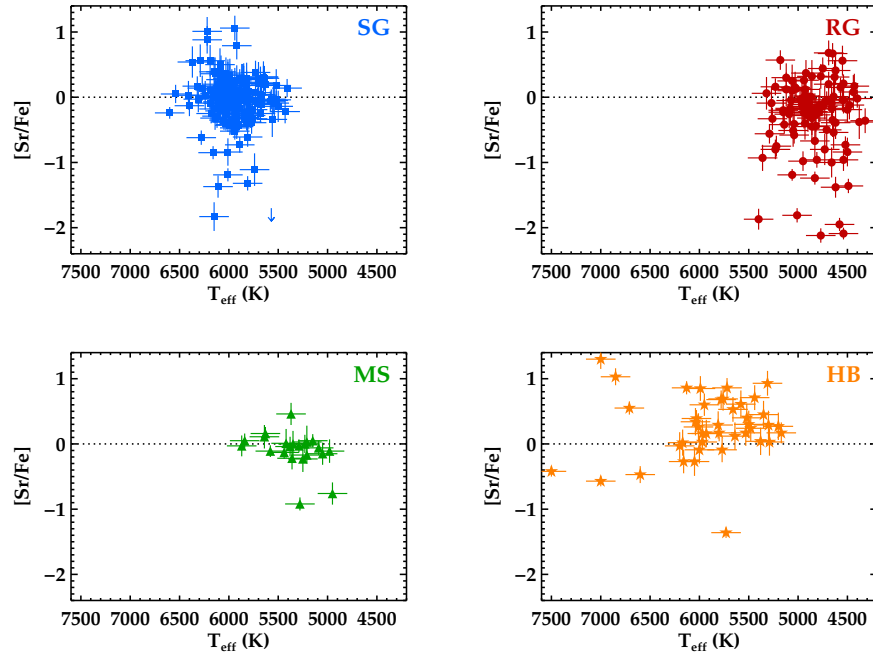


FIG. 45.— Derived $[\text{Sr}/\text{Fe}]$ ratios as a function of T_{eff} . Symbols are the same as in Figures 22 and 23.

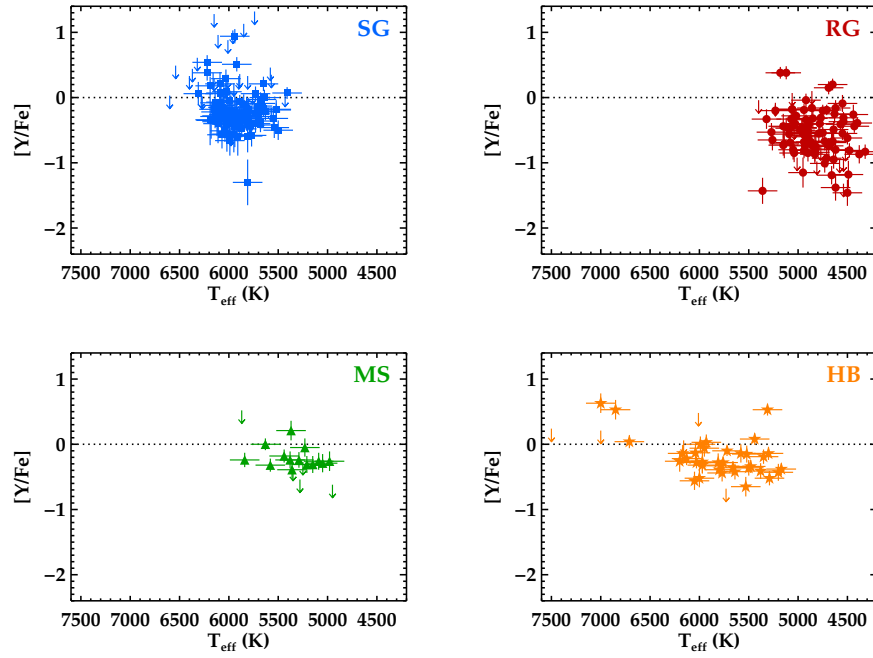


FIG. 46.— Derived $[\text{Y}/\text{Fe}]$ ratios as a function of T_{eff} . Symbols are the same as in Figures 22 and 23.

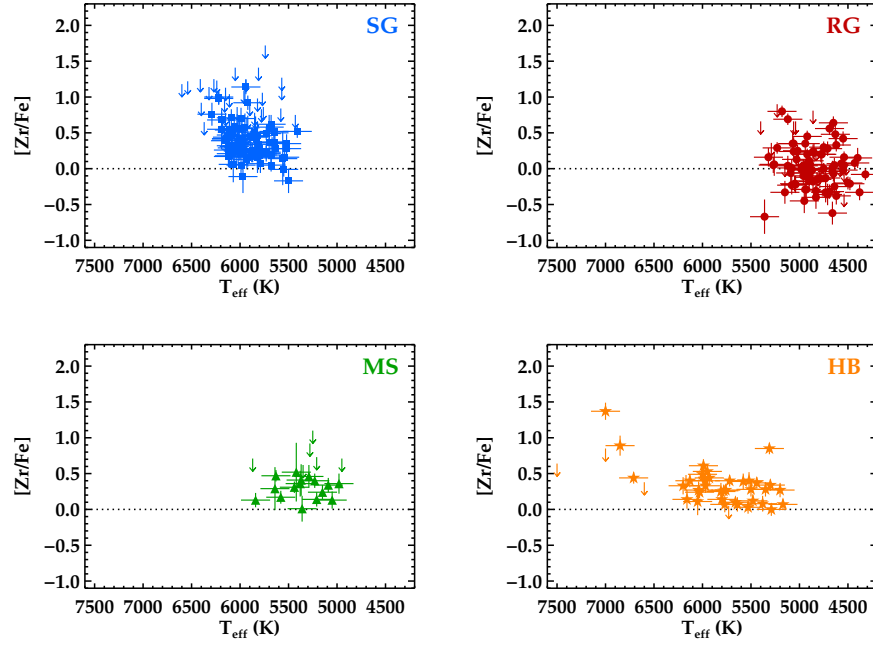


FIG. 47.— Derived $[Zr/Fe]$ ratios as a function of T_{eff} . Symbols are the same as in Figures 22 and 23.

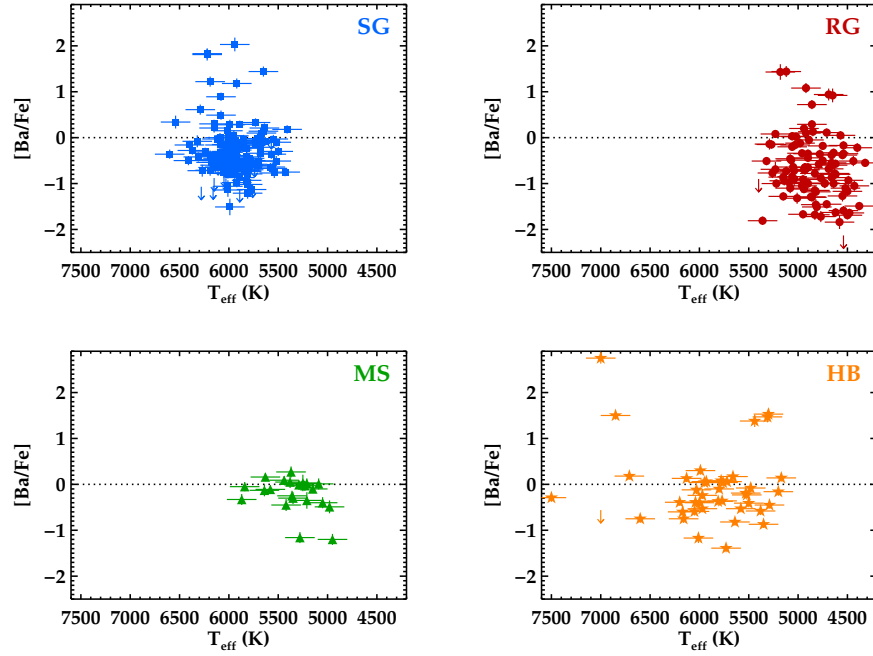


FIG. 48.— Derived $[Ba/Fe]$ ratios as a function of T_{eff} . Symbols are the same as in Figures 22 and 23.

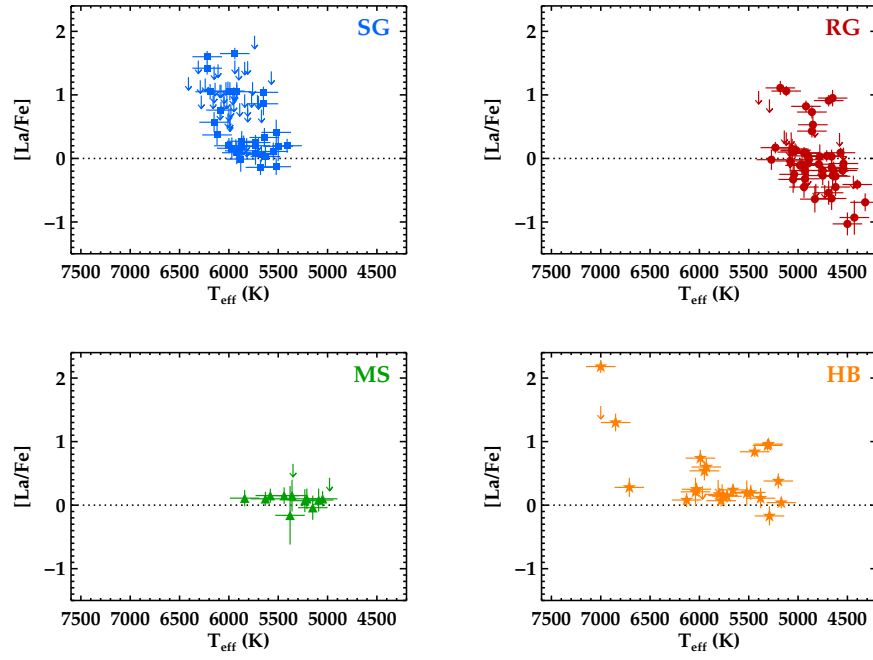


FIG. 49.— Derived $[\text{La}/\text{Fe}]$ ratios as a function of T_{eff} . Symbols are the same as in Figures 22 and 23.

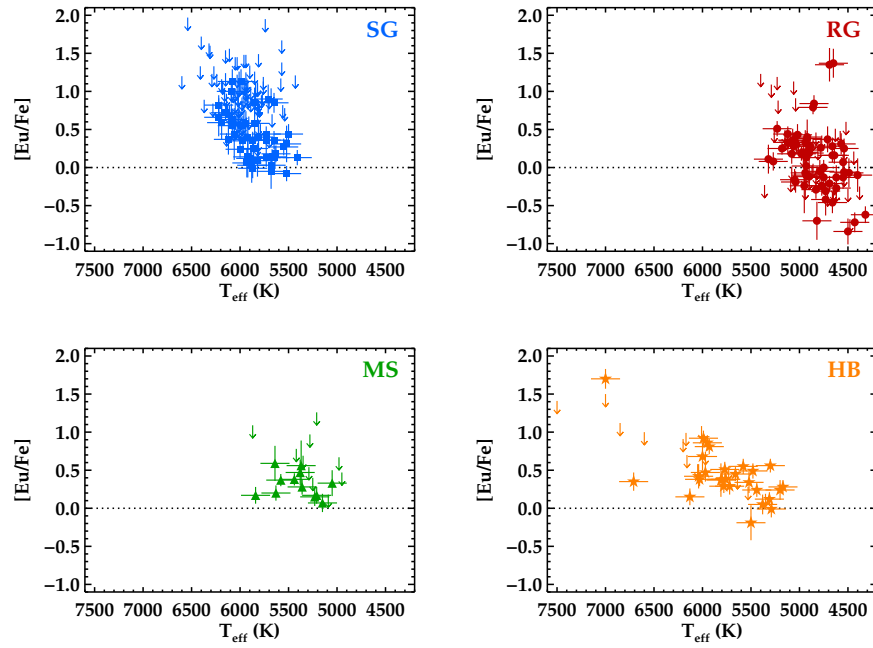


FIG. 50.— Derived $[\text{Eu}/\text{Fe}]$ ratios as a function of T_{eff} . Symbols are the same as in Figures 22 and 23.

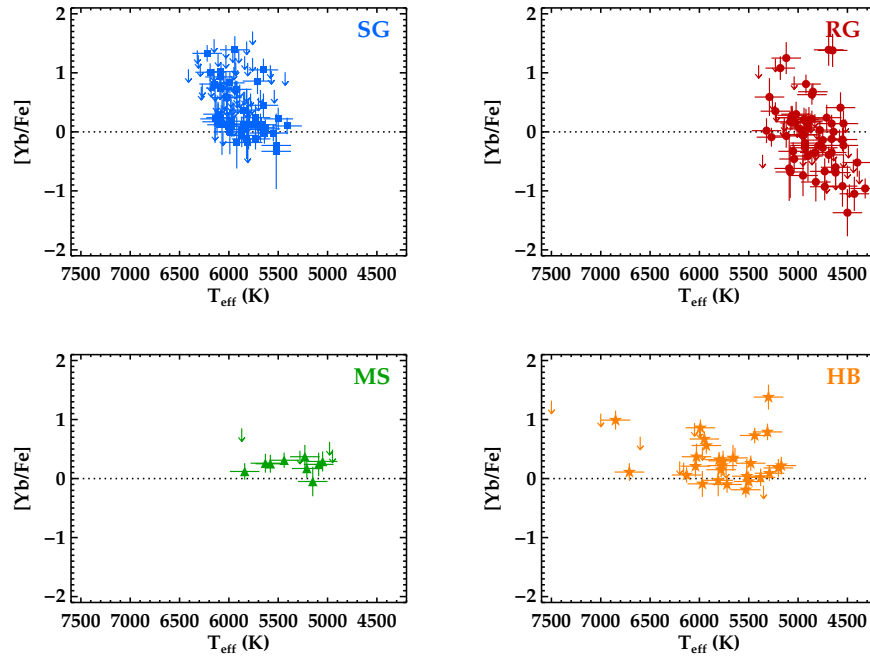


FIG. 51.— Derived [Yb/Fe] ratios as a function of T_{eff} . Symbols are the same as in Figures 22 and 23.

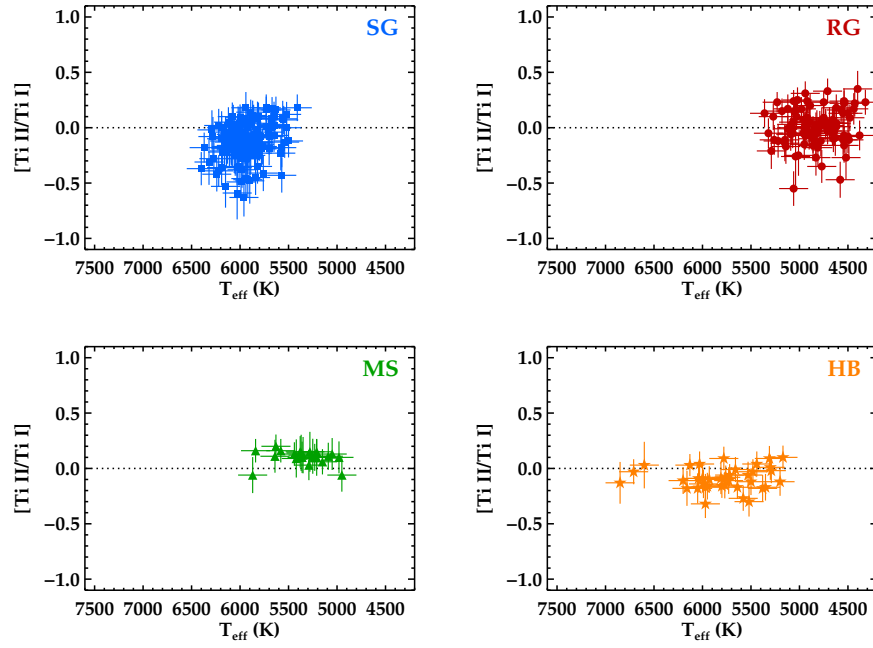


FIG. 52.— Ratios of the total titanium abundance derived from each of the ionized and neutral species as a function of T_{eff} . Each star is displayed only if both species have been detected. Symbols are the same as in Figures 22 and 23.

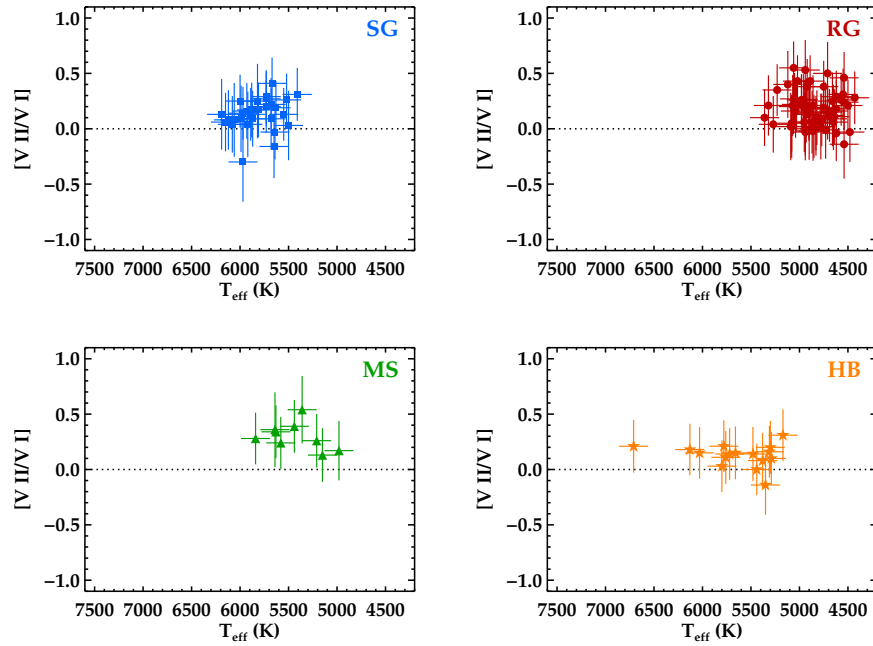


FIG. 53.— Ratios of the total vanadium abundance derived from each of the ionized and neutral species as a function of T_{eff} . Each star is displayed only if both species have been detected. Symbols are the same as in Figures 22 and 23.

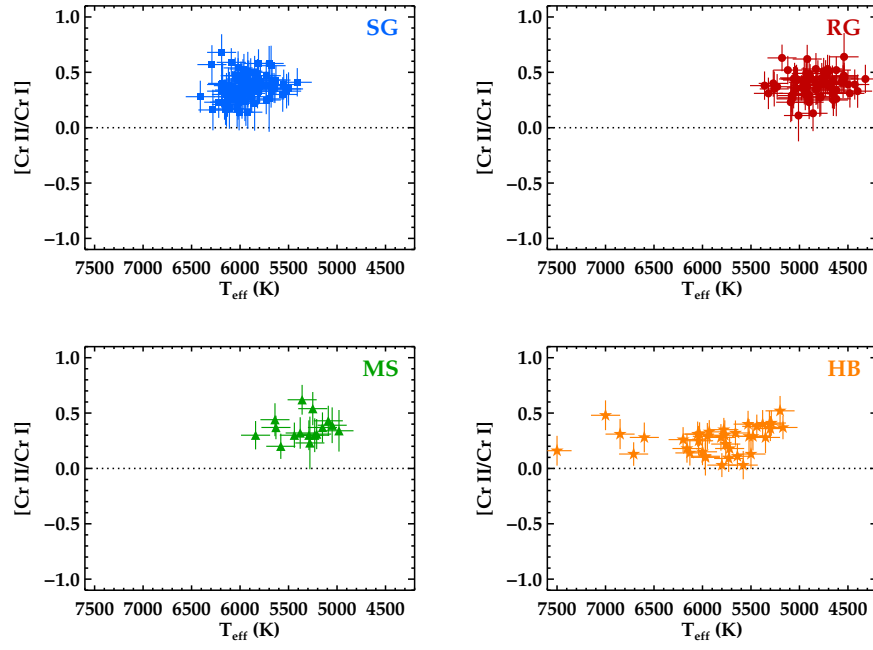


FIG. 54.— Ratios of the total chromium abundance derived from each of the ionized and neutral species as a function of T_{eff} . Each star is displayed only if both species have been detected. Symbols are the same as in Figures 22 and 23.

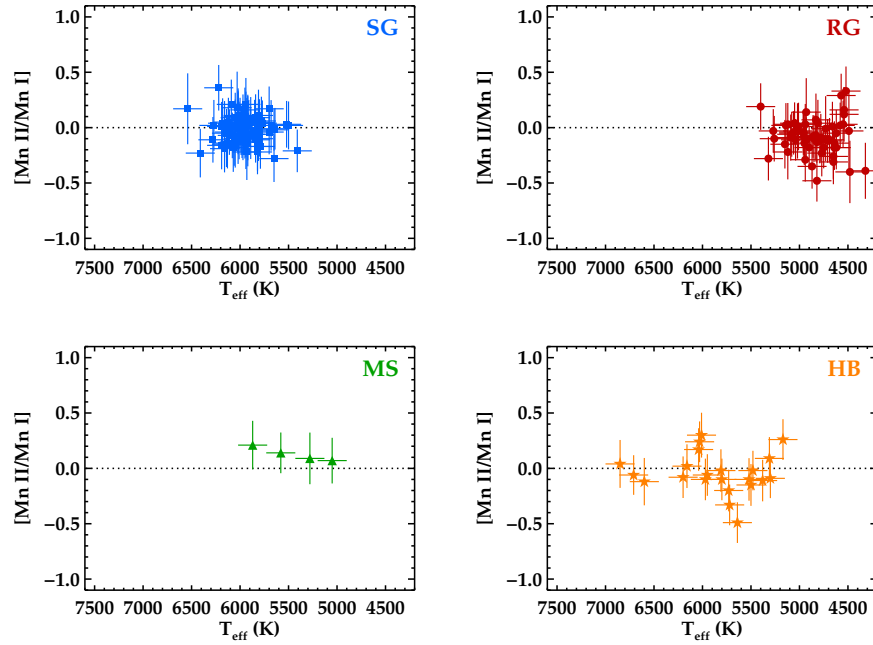


FIG. 55.— Ratios of the total manganese abundance derived from each of the ionized and neutral species as a function of T_{eff} . Each star is displayed only if both species have been detected. Symbols are the same as in Figures 22 and 23.

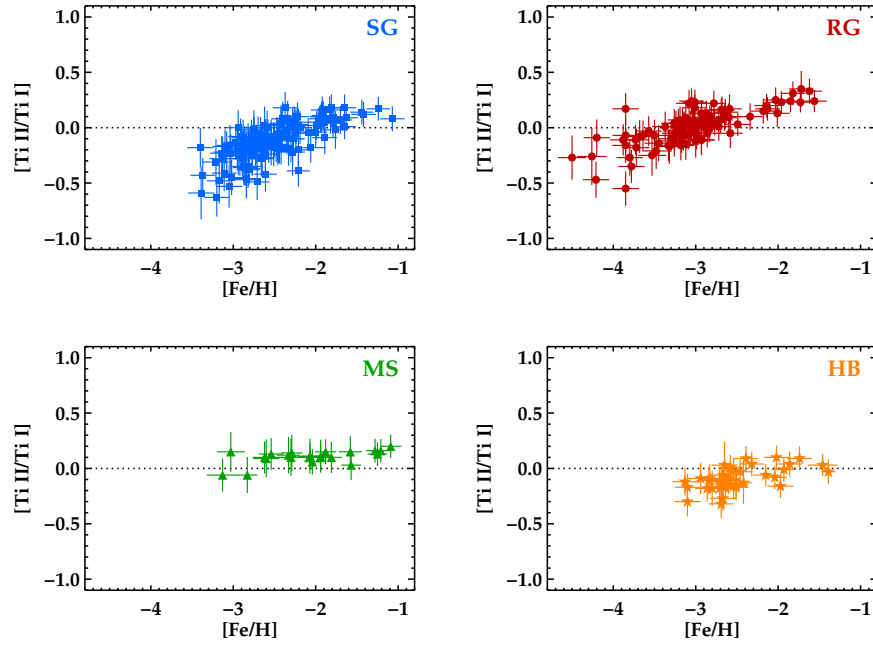


FIG. 56.— Ratios of the total titanium abundance derived from each of the ionized and neutral species as a function of $[\text{Fe}/\text{H}]$. Each star is displayed only if both species have been detected. Symbols are the same as in Figures 22 and 23.

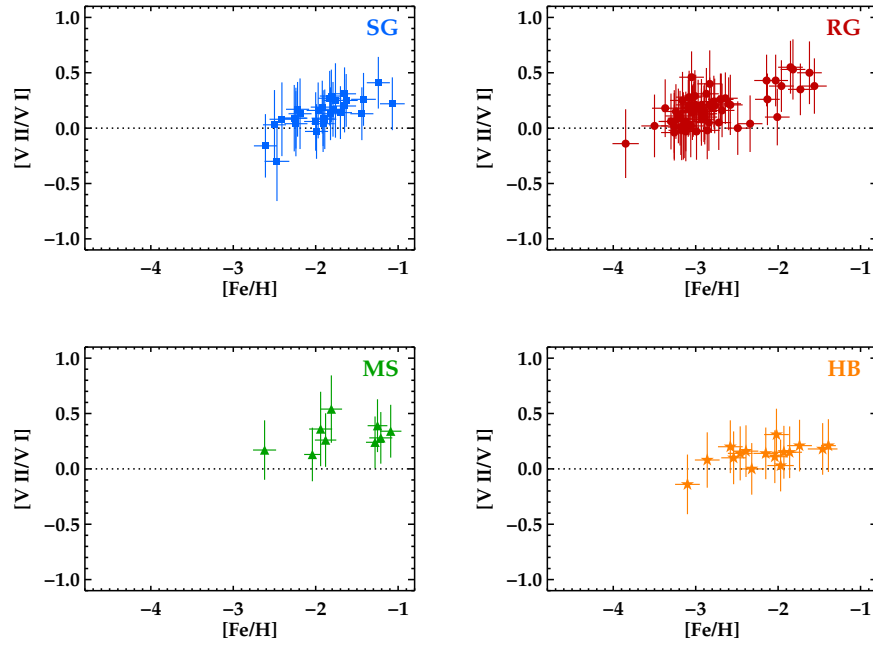


FIG. 57.— Ratios of the total vanadium abundance derived from each of the ionized and neutral species as a function of $[\text{Fe}/\text{H}]$. Each star is displayed only if both species have been detected. Symbols are the same as in Figures 22 and 23.

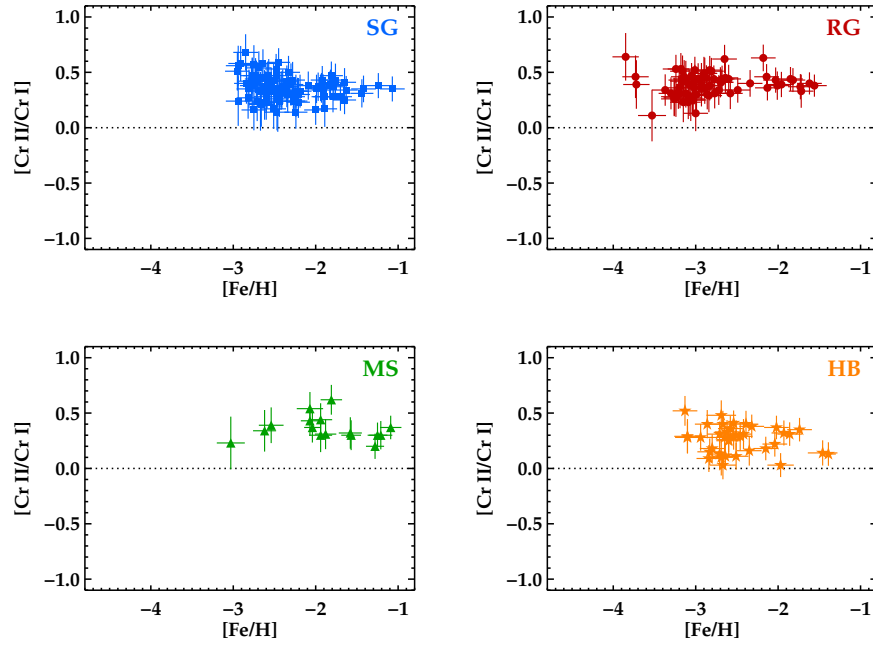


FIG. 58.— Ratios of the total chromium abundance derived from each of the ionized and neutral species as a function of $[\text{Fe}/\text{H}]$. Each star is displayed only if both species have been detected. Symbols are the same as in Figures 22 and 23.

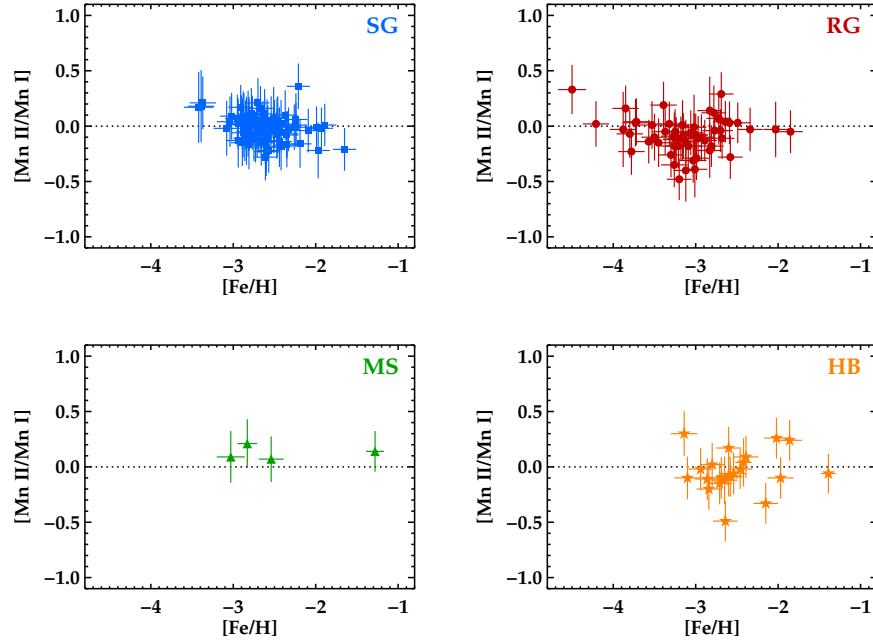


FIG. 59.— Ratios of the total manganese abundance derived from each of the ionized and neutral species as a function of $[\text{Fe}/\text{H}]$. Each star is displayed only if both species have been detected. Symbols are the same as in Figures 22 and 23.

TABLE 17
MAGNITUDES, REDDENINGS, COLORS, ATMOSPHERIC PARAMETERS, AND
RANDOM UNCERTAINTIES

Class ^a	Star	V	$E(B - V)$	$(B - V)_0$	$(V - K)_0$	T_{eff} (K)	$\log g$	v_t (km s ⁻¹)	[M/H]	$\sigma_{T_{\text{eff}}}$ (K)	$\sigma_{\log g}$	σ_{v_t} (km s ⁻¹)	$\sigma_{[\text{M}/\text{H}]}$ ^b
RG	CS 22166-016	12.75	0.025	0.63	1.92	4900	1.75	1.50	-3.09	37	0.14	0.06	0.06
SG	CS 22169-008	14.99	0.057	0.37	1.27	5810	3.60	1.30	-2.59	54	0.16	0.06	0.06
RG	CS 22169-035	12.88	0.043	0.89	2.41	4480	0.50	1.70	-3.12	34	0.14	0.06	0.06
SG	CS 22171-031	13.93	0.023	0.37	1.22	6010	3.70	1.35	-2.42	53	0.21	0.06	0.06
SG	CS 22171-037	14.93	0.020	0.33	1.11	6110	3.65	1.60	-3.35	40	0.15	0.06	0.09
RG	CS 22172-029	14.36	0.056	...	1.81	4960	1.90	1.30	-2.70	37	0.16	0.06	0.06
SG	CS 22174-020	15.06	0.040	0.36	1.18	5840	3.55	1.40	-3.02	58	0.16	0.06	0.06
SG	CS 22177-009	14.27	0.044	0.36	1.20	5940	3.55	1.25	-3.37	38	0.16	0.06	0.08
SG	CS 22177-010	14.31	0.050	0.35	1.25	6050	3.70	1.50	-2.88	46	0.18	0.06	0.07
SG	CS 22180-014	13.58	0.021	0.41	1.38	5780	3.55	1.50	-2.90	43	0.16	0.06	0.07
SG	CS 22182-033	14.67	0.033	0.41	1.41	5810	3.60	1.30	-2.47	47	0.16	0.06	0.06
SG	CS 22182-047	13.24	0.047	0.43	1.43	5640	3.60	1.05	-1.99	48	0.17	0.06	0.06
RG	CS 22183-031	13.62	0.039	0.63	1.93	4850	1.60	1.55	-3.50	36	0.14	0.06	0.06
RG	CS 22185-007	13.34	0.047	0.64	2.08	4730	1.30	1.55	-3.02	38	0.15	0.06	0.06
SG	CS 22186-002	13.77	0.014	0.40	1.33	5500	3.35	1.15	-2.50	38	0.18	0.06	0.06
SG	CS 22186-017	13.53	0.021	0.41	1.35	5770	3.55	1.30	-2.90	50	0.15	0.06	0.07
RG	CS 22186-023	12.84	0.022	0.66	1.96	4820	1.55	1.60	-2.89	34	0.12	0.06	0.06
RG	CS 22189-009	14.06	0.025	0.73	2.19	4540	0.60	1.65	-3.85	34	0.14	0.06	0.06
HB	CS 22191-029	14.05	0.019	0.39	1.39	5810	1.55	2.80	-2.94	44	0.36	0.06	0.06
SG	CS 22871-104	14.91	0.116	0.31	1.04	6370	4.00	1.40	-2.06	48	0.48	0.06	0.06
SG	CS 22872-102	13.65	0.231	0.36	1.40	6020	3.65	1.40	-2.82	49	0.16	0.06	0.07
SG	CS 22873-072	14.64	0.066	0.34	1.14	6030	3.70	1.40	-2.86	42	0.15	0.06	0.06
RG	CS 22873-128	13.05	0.036	0.66	2.08	4710	1.20	1.65	-3.24	34	0.14	0.06	0.06
SG	CS 22874-123	14.70	0.105	0.34	1.24	6240	3.80	1.65	-2.61	40	0.20	0.06	0.06
HB	CS 22875-029	13.69	0.013	0.39	1.39	5990	1.85	2.80	-2.69	44	0.27	0.06	0.06
SG	CS 22876-040	15.09	0.015	0.39	1.20	6090	3.80	1.45	-2.21	50	0.18	0.06	0.06
RG	CS 22877-001	12.16	0.057	0.71	2.01	4790	1.45	1.55	-3.24	34	0.14	0.06	0.06
RG	CS 22877-011	13.86	0.038	0.56	1.88	4950	1.90	1.45	-3.12	37	0.14	0.06	0.06
SG	CS 22877-015	13.23	0.040	0.36	1.23	6150	3.85	1.30	-2.00	43	0.22	0.06	0.06
SG	CS 22877-051	14.26	0.051	0.29	1.19	6050	3.70	1.50	-2.77	46	0.17	0.06	0.07
SG	CS 22878-002	14.36	0.076	0.37	1.24	5850	3.55	1.30	-3.10	41	0.18	0.06	0.07
SG	CS 22878-027	14.41	0.067	0.37	1.26	5820	3.55	1.20	-2.97	51	0.15	0.06	0.07
RG	CS 22878-101	13.73	0.100	0.75	2.21	4650	1.05	1.90	-3.30	35	0.14	0.06	0.06
SG	CS 22879-012	14.72	0.035	0.35	1.22	6020	3.65	1.25	-2.81	49	0.14	0.06	0.07
SG	CS 22879-029	14.43	0.042	0.38	1.19	5920	3.70	1.30	-2.35	41	0.17	0.06	0.06
SG	CS 22879-051	13.89	0.039	0.35	1.16	6190	3.75	1.50	-2.85	51	0.22	0.06	0.07
SG	CS 22879-094	15.20	0.046	0.37	1.33	5820	3.60	1.35	-2.81	51	0.14	0.06	0.06
HB	CS 22879-097	14.22	0.048	0.41	1.47	5640	1.55	2.55	-2.64	56	0.36	0.06	0.06
HB	CS 22879-103	14.30	0.045	0.44	1.52	5720	1.60	2.55	-2.15	44	0.22	0.06	0.05
SG	CS 22880-067	15.08	0.083	0.43	1.36	5570	3.35	1.05	-3.37	57	0.20	0.08	0.07
RG	CS 22880-086	14.41	0.067	0.57	1.94	4960	1.90	1.40	-3.25	39	0.15	0.06	0.06
SG	CS 22881-032	15.23	0.015	0.36	1.25	5430	3.20	1.25	-3.10	36	0.18	0.06	0.06
SG	CS 22881-036	13.93	0.014	0.44	1.21	5940	3.70	1.10	-2.37	45	0.16	0.06	0.06
HB	CS 22881-039	15.14	0.014	0.38	1.46	6170	2.05	2.80	-2.79	40	0.29	0.06	0.06
SG	CS 22881-070	14.39	0.011	0.36	1.19	6020	3.70	1.35	-2.73	49	0.19	0.06	0.07
HB	CS 22882-001	14.82	0.018	0.38	1.46	5930	1.90	3.00	-2.62	52	0.32	0.06	0.05
SG	CS 22882-006	14.14	0.023	0.39	1.35	5800	3.60	1.35	-2.66	44	0.18	0.06	0.07
SG	CS 22882-012	15.26	0.015	0.46	1.18	6290	3.80	1.40	-2.75	48	0.17	0.06	0.07
SG	CS 22882-030	14.83	0.017	0.36	1.34	5580	3.40	1.10	-3.14	45	0.14	0.06	0.06
HB	CS 22883-037	14.73	0.028	0.52	1.28	5800	1.50	3.15	-1.97	44	0.25	0.06	0.05
SG	CS 22884-020	14.95	0.110	0.35	1.12	6040	3.75	1.45	-2.27	49	0.19	0.06	0.06
SG	CS 22884-108	14.24	0.135	0.37	1.28	6320	3.75	1.20	-3.21	52	0.17	0.06	0.10
SG	CS 22885-040	15.24	0.056	0.34	1.29	6160	3.75	1.45	-2.60	47	0.17	0.06	0.06
RG	CS 22885-096	13.33	0.056	0.63	2.09	4580	0.75	1.75	-4.21	34	0.15	0.06	0.07
SG	CS 22885-203	14.23	0.046	0.36	1.27	5820	3.60	1.30	-2.57	44	0.16	0.06	0.06
SG	CS 22886-003	14.60	0.043	0.37	1.18	5970	3.65	1.40	-2.87	38	0.16	0.06	0.09
SG	CS 22886-012	14.52	0.049	0.42	1.37	5650	3.50	1.45	-2.61	42	0.15	0.06	0.06
HB	CS 22886-013	13.65	0.050	0.19	0.73	6200	1.75	2.95	-2.60	40	0.22	0.06	0.06
SG	CS 22886-044	14.23	0.050	0.46	1.45	5730	3.75	1.20	-1.65	43	0.19	0.06	0.06
SG	CS 22888-002	14.70	0.018	0.40	1.36	5700	3.50	1.30	-2.91	46	0.15	0.06	0.07
SG	CS 22888-014	14.44	0.021	0.38	1.21	6020	3.70	1.35	-2.69	45	0.19	0.06	0.06
SG	CS 22888-031	14.90	0.014	0.40	1.28	5810	3.50	1.25	-3.41	44	0.20	0.06	0.08
HB	CS 22888-047	14.61	0.019	0.38	1.44	5950	1.90	3.00	-2.54	46	0.27	0.06	0.05
SG	CS 22889-050	14.28	0.055	0.32	1.19	5920	3.60	1.40	-2.84	50	0.19	0.06	0.06
SG	CS 22890-011	14.61	0.045	0.33	1.15	6010	3.70	1.25	-2.47	57	0.18	0.06	0.06
RG	CS 22890-024	13.41	0.054	0.52	1.82	5320	2.95	1.25	-2.58	37	0.17	0.06	0.06
SG	CS 22890-064	14.70	0.043	0.35	1.16	5960	3.60	1.30	-3.20	52	0.16	0.06	0.06
HB	CS 22891-184	13.83	0.071	0.43	1.45	5530	1.60	2.05	-2.67	65	0.45	0.06	0.05
RG	CS 22891-200	13.93	0.079	0.78	2.30	4490	0.50	1.70	-3.88	33	0.12	0.06	0.06
RG	CS 22891-209	12.17	0.078	0.75	2.33	4620	0.95	1.80	-3.26	34	0.13	0.06	0.05
RG	CS 22891-221	14.43	0.076	0.48	1.62	5290	2.80	1.85	-3.48	42	0.25	0.06	0.07
SG	CS 22892-025	14.03	0.032	0.36	1.21	6140	3.75	1.45	-2.66	43	0.19	0.06	0.06
RG	CS 22892-052	13.21	0.031	0.77	2.19	4690	1.15	1.50	-3.16	37	0.15	0.06	0.07

TABLE 17 — *Continued*

Class ^a	Star	V	$E(B - V)$	$(B - V)_0$	$(V - K)_0$	T_{eff} (K)	$\log g$	v_t (km s ⁻¹)	[M/H]	$\sigma_{T_{\text{eff}}}$ (K)	$\sigma_{\log g}$	σ_{v_t} (km s ⁻¹)	$\sigma_{\text{[M/H]}}$ ^b
RG	CS 22893-005	14.22	0.041	0.49	1.66	5260	2.75	1.30	-2.93	44	0.22	0.06	0.07
RG	CS 22893-010	14.74	0.038	0.55	...	5150	2.45	1.35	-2.93	44	0.20	0.06	0.07
SG	CS 22893-011	14.54	0.041	0.39	1.29	6010	3.75	1.40	-2.27	49	0.19	0.06	0.07
SG	CS 22894-004	14.17	0.043	0.37	1.25	5920	3.65	1.50	-2.65	41	0.19	0.06	0.07
SG	CS 22894-019	13.92	0.035	0.41	1.32	5930	3.60	1.25	-3.04	48	0.19	0.06	0.10
SG	CS 22894-023	13.75	0.035	0.37	1.27	5980	3.65	1.40	-2.82	42	0.17	0.06	0.07
MS	CS 22894-049	14.46	0.030	0.42	1.35	5870	3.90	1.15	-2.83	36	0.22	0.09	0.08
RG	CS 22896-015	14.85	0.058	0.35	...	5080	2.25	1.25	-2.84	38	0.16	0.06	0.07
HB	CS 22896-055	13.53	0.050	0.38	1.44	5970	1.85	3.15	-2.51	48	0.28	0.06	0.06
HB	CS 22896-110	13.56	0.060	0.47	1.62	5380	1.15	2.25	-2.86	48	0.39	0.06	0.06
SG	CS 22896-115	14.13	0.058	0.36	1.27	5910	3.65	1.20	-2.72	45	0.14	0.06	0.08
SG	CS 22896-136	14.71	0.059	0.35	1.14	6190	3.85	1.40	-2.19	47	0.21	0.06	0.07
RG	CS 22897-008	13.33	0.033	0.66	2.24	4550	0.70	1.70	-3.73	36	0.14	0.06	0.07
HB	CS 22898-043	14.06	0.050	0.38	1.28	6160	2.15	3.10	-2.80	48	0.30	0.06	0.07
RG	CS 22898-047	14.24	0.059	0.50	1.74	5150	2.40	1.40	-3.45	37	0.18	0.06	0.09
HB	CS 22937-072	14.02	0.041	0.49	1.69	5500	1.75	2.05	-2.71	44	0.22	0.06	0.06
HB	CS 22940-070	14.87	0.055	0.42	1.41	6130	1.85	3.00	-1.46	84	0.47	0.06	0.06
HB	CS 22940-077	14.13	0.070	0.46	1.72	5350	1.35	2.00	-3.10	44	0.22	0.06	0.06
HB	CS 22940-121	14.16	0.053	0.50	1.75	5200	1.15	1.95	-3.13	48	0.30	0.06	0.07
RG	CS 22941-017	15.00	0.021	0.54	1.84	5070	2.20	1.45	-3.08	40	0.17	0.06	0.08
HB	CS 22941-027	14.05	0.016	0.33	1.26	6050	1.70	3.15	-2.71	48	0.30	0.06	0.06
RG	CS 22942-002	13.79	0.021	0.59	1.77	5010	2.00	1.55	-3.53	38	0.17	0.06	0.10
RG	CS 22942-011	12.94	0.017	0.61	2.01	4930	1.85	1.25	-2.83	39	0.17	0.06	0.07
RG	CS 22942-035	14.56	0.021	0.59	1.96	4940	1.85	1.50	-2.99	38	0.16	0.06	0.06
SG	CS 22943-059	14.40	0.041	...	0.97	5810	3.60	1.15	-2.64	54	0.15	0.06	0.07
SG	CS 22943-095	11.71	0.033	0.32	1.16	6140	3.80	1.35	-2.44	51	0.18	0.06	0.07
SG	CS 22943-132	13.31	0.043	0.37	1.25	5850	3.60	1.40	-2.67	41	0.16	0.06	0.08
RG	CS 22943-137	14.45	0.038	0.37	1.42	5400	3.10	1.20	-3.39	48	0.27	0.06	0.08
HB	CS 22943-201	15.98	0.037	0.33	2.12	5970	2.45	1.60	-2.69	52	0.39	0.06	0.06
SG	CS 22944-014	14.18	0.057	0.37	1.29	6020	3.70	1.30	-2.62	45	0.20	0.06	0.08
RG	CS 22944-032	13.28	0.043	0.55	1.84	5090	2.30	1.45	-3.15	36	0.14	0.06	0.08
SG	CS 22944-061	14.35	0.046	0.38	1.34	5920	3.60	1.50	-2.95	45	0.21	0.06	0.08
SG	CS 22945-017	14.43	0.020	0.37	1.12	6080	3.70	1.25	-2.73	54	0.19	0.06	0.08
RG	CS 22945-024	14.36	0.026	0.69	1.86	5120	2.35	1.15	-2.59	50	0.24	0.07	0.06
RG	CS 22945-028	14.64	0.025	0.66	1.92	4900	1.75	1.50	-2.89	41	0.18	0.06	0.06
SG	CS 22945-031	14.77	0.022	0.36	1.18	5820	3.55	1.35	-3.03	47	0.19	0.06	0.08
HB	CS 22945-056	14.09	0.020	0.38	1.42	6000	1.75	3.45	-2.83	48	0.25	0.06	0.06
SG	CS 22945-058	14.96	0.023	0.34	1.21	5990	3.65	1.55	-2.71	45	0.17	0.06	0.08
HB	CS 22945-063	14.55	0.022	...	1.55	5730	1.70	2.55	-2.84	48	0.31	0.06	0.06
HB	CS 22947-187	12.96	0.064	0.58	1.76	5300	1.40	1.85	-2.58	52	0.37	0.06	0.06
RG	CS 22948-066	13.47	0.025	0.61	1.96	4830	1.55	2.00	-3.18	34	0.15	0.06	0.07
SG	CS 22948-093	15.18	0.016	0.34	1.14	6540	3.85	1.15	-3.42	51	0.15	0.06	0.13
SG	CS 22949-030	13.85	0.045	0.38	1.21	5890	3.60	1.40	-2.88	48	0.16	0.06	0.07
RG	CS 22949-037	14.36	0.051	0.74	2.14	4630	0.95	1.70	-4.20	34	0.13	0.06	0.07
RG	CS 22949-048	13.67	0.036	0.80	2.29	4620	0.95	1.70	-3.37	35	0.14	0.06	0.07
RG	CS 22950-046	14.22	0.062	...	2.46	4380	0.50	1.80	-3.64	32	0.12	0.06	0.07
SG	CS 22951-005	14.90	0.017	0.37	1.15	5950	3.65	1.30	-2.67	48	0.16	0.06	0.07
RG	CS 22951-059	14.44	0.017	0.54	1.70	5120	2.35	1.50	-2.83	42	0.19	0.06	0.07
HB	CS 22951-077	13.61	0.016	0.48	1.72	5290	1.45	1.85	-2.54	52	0.43	0.06	0.06
RG	CS 22952-015	13.27	0.035	0.78	2.26	4500	0.55	1.75	-3.68	33	0.13	0.06	0.07
RG	CS 22953-003	13.77	0.017	0.67	2.08	4860	1.65	1.45	-3.00	37	0.17	0.06	0.07
SG	CS 22953-037	13.64	0.028	0.34	1.11	6150	3.70	1.65	-3.05	47	0.17	0.06	0.10
SG	CS 22954-004	14.27	0.028	0.39	1.26	5810	3.55	1.30	-2.78	51	0.18	0.06	0.08
SG	CS 22954-015	13.03	0.031	0.42	1.23	5930	3.75	1.30	-1.97	42	0.17	0.06	0.06
BS	CS 22955-110	13.61	0.052	0.29	0.92	6710	3.45	1.90	-1.39	36	0.29	0.06	0.06
HB	CS 22955-174	14.38	0.049	0.45	1.48	5520	1.35	2.20	-3.10	48	0.27	0.06	0.07
SG	CS 22956-015	14.19	0.042	0.35	1.21	5960	3.70	1.35	-2.48	48	0.15	0.06	0.07
SG	CS 22956-021	14.70	0.038	0.34	1.19	6020	3.70	1.20	-2.51	49	0.18	0.06	0.08
RG	CS 22956-050	14.25	0.034	0.74	2.14	4640	1.00	1.75	-3.57	36	0.14	0.06	0.07
SG	CS 22956-062	14.84	0.033	0.44	1.40	5540	3.40	1.65	-2.76	42	0.15	0.06	0.07
SG	CS 22956-081	15.18	0.029	0.35	1.26	6310	3.80	1.65	-2.80	57	0.20	0.06	0.07
SG	CS 22956-102	15.10	0.026	0.41	1.26	6220	3.85	1.50	-2.21	60	0.23	0.06	0.07
SG	CS 22956-106	14.47	0.032	0.35	1.12	6410	3.90	1.75	-2.60	53	0.21	0.06	0.07
HB	CS 22956-110	14.79	0.027	0.36	1.25	6010	1.85	2.85	-3.14	56	0.39	0.06	0.07
RG	CS 22956-114	14.04	0.027	0.57	...	4900	1.75	1.85	-2.86	39	0.16	0.06	0.06
RG	CS 22957-013	14.08	0.030	0.70	2.14	4620	0.95	1.55	-3.01	35	0.15	0.06	0.06
SG	CS 22957-019	13.71	0.035	0.38	1.30	6070	3.75	1.25	-2.42	42	0.19	0.06	0.07
RG	CS 22957-022	13.34	0.033	0.58	1.94	4860	1.65	1.55	-3.17	37	0.15	0.06	0.07
SG	CS 22957-024	14.30	0.032	0.35	1.19	6160	3.75	1.35	-2.81	55	0.20	0.06	0.09
SG	CS 22957-026	13.16	0.040	0.40	1.25	6120	3.90	1.35	-1.89	47	0.25	0.06	0.07
RG	CS 22957-027	13.60	0.039	0.79	1.99	5220	2.65	1.45	-3.00	39	0.23	0.06	0.07
SG	CS 22957-036	14.43	0.038	0.38	1.21	5970	3.75	1.25	-2.09	45	0.19	0.06	0.06
HB	CS 22958-037	14.91	0.019	0.51	1.66	5770	2.10	2.30	-2.51	40	0.29	0.06	0.06
SG	CS 22958-041	15.07	0.024	0.40	1.29	6010	3.65	1.55	-2.88	39	0.30	0.06	0.08
SG	CS 22958-042	14.52	0.025	0.45	1.24	5760	3.55	0.95	-2.99	57	0.18	0.08	0.11

TABLE 17 — *Continued*

Class ^a	Star	V	$E(B - V)$	$(B - V)_0$	$(V - K)_0$	T_{eff} (K)	$\log g$	v_t (km s ⁻¹)	[M/H]	$\sigma_{T_{\text{eff}}}$ (K)	$\sigma_{\log g}$	σ_{v_t} (km s ⁻¹)	$\sigma_{\text{[M/H]}}$ ^b
SG	CS 22958-052	14.22	0.024	0.41	1.14	6090	3.75	1.95	-2.42	46	0.18	0.06	0.07
SG	CS 22958-065	14.48	0.023	0.44	1.24	6020	3.75	1.30	-2.24	57	0.20	0.06	0.07
SG	CS 22958-074	14.80	0.025	0.47	1.31	5800	3.60	1.40	-2.62	44	0.18	0.06	0.08
RG	CS 22958-083	14.42	0.036	0.63	1.93	4900	1.75	1.40	-3.04	35	0.13	0.06	0.07
RG	CS 22959-074	14.22	0.093	0.56	1.95	4940	1.90	1.35	-2.49	35	0.17	0.06	0.06
SG	CS 22959-139	14.29	0.059	0.34	1.25	6090	3.75	1.55	-2.45	46	0.17	0.06	0.07
MS	CS 22960-010	13.81	0.011	0.45	1.21	5280	4.00	1.20	-3.03	44	0.36	0.13	0.08
SG	CS 22960-029	15.05	0.016	0.39	1.36	5890	3.60	1.45	-2.77	52	0.14	0.06	0.08
RG	CS 22960-048	14.96	0.018	0.60	1.95	4770	1.40	1.55	-3.78	36	0.14	0.06	0.07
RG	CS 22960-053	14.95	0.012	0.74	2.16	4860	1.65	1.60	-3.33	40	0.18	0.06	0.08
RG	CS 22960-064	13.94	0.017	0.60	1.87	5060	2.20	1.40	-2.77	36	0.14	0.06	0.07
RG	CS 22963-004	14.98	0.052	0.48	1.64	5060	2.15	1.50	-3.85	42	0.16	0.06	0.08
SG	CS 22964-115	14.94	0.083	0.35	1.08	6090	3.70	1.40	-2.70	54	0.15	0.06	0.07
SG	CS 22964-176	15.33	0.078	0.36	1.15	6000	3.70	1.40	-2.46	49	0.19	0.06	0.07
SG	CS 22964-183	14.45	0.079	0.26	1.20	6010	3.65	1.45	-2.87	42	0.15	0.06	0.08
SG	CS 22964-214	13.66	0.088	0.31	1.11	6180	3.75	1.45	-2.84	47	0.17	0.06	0.08
RG	CS 22965-016	14.05	0.044	0.71	2.16	4770	1.40	1.85	-2.93	33	0.12	0.06	0.06
SG	CS 22965-054	15.07	0.130	0.37	1.27	6050	3.70	1.60	-2.89	53	0.15	0.06	0.07
SG	CS 22968-001	14.74	0.018	0.37	1.25	5940	3.65	1.30	-2.84	52	0.21	0.06	0.09
RG	CS 22968-014	13.68	0.012	0.74	2.18	4540	0.60	1.75	-3.85	34	0.14	0.06	0.08
SG	CS 22968-026	14.24	0.033	0.40	1.39	5850	3.65	1.20	-2.33	44	0.18	0.06	0.07
SG	CS 22968-029	14.29	0.016	0.39	1.35	5760	3.50	1.40	-3.11	47	0.15	0.06	0.09
SG	CS 29493-023	14.59	0.031	0.35	1.22	5980	3.65	1.25	-2.66	52	0.15	0.06	0.08
SG	CS 29493-050	14.39	0.033	0.35	1.10	6270	3.80	1.45	-2.89	48	0.17	0.06	0.08
SG	CS 29493-062	13.17	0.034	0.43	1.53	5520	3.40	1.15	-2.59	44	0.18	0.06	0.08
SG	CS 29493-094	14.12	0.025	0.35	1.19	6130	3.80	1.55	-2.44	43	0.19	0.06	0.07
SG	CS 29495-005	14.32	0.035	0.38	1.26	5990	3.75	1.15	-2.26	38	0.19	0.06	0.08
RG	CS 29495-042	13.61	0.033	0.59	1.65	5180	2.55	1.45	-2.18	46	0.26	0.06	0.06
BS	CS 29497-030	12.66	0.017	0.28	0.88	7000	4.00	1.60	-2.52	44	0.39	0.06	0.08
RG	CS 29498-043	13.72	0.104	1.08	2.78	4440	0.50	1.75	-3.85	20	0.13	0.06	0.08
SG	CS 29499-003	14.29	0.017	0.35	1.09	6080	3.75	1.25	-2.35	46	0.18	0.06	0.07
SG	CS 29499-058	13.76	0.021	0.37	1.26	6060	3.70	1.45	-2.61	42	0.17	0.06	0.08
SG	CS 29499-060	13.03	0.020	0.35	1.12	6280	3.80	1.30	-2.75	52	0.18	0.06	0.09
SG	CS 29501-032	14.53	0.093	0.38	1.28	5950	3.65	0.60	-2.71	48	0.14	0.07	0.09
RG	CS 29502-092	11.87	0.097	0.67	2.00	4820	1.50	1.50	-3.20	34	0.14	0.06	0.07
HB	CS 29504-004	14.34	0.019	0.16	0.58	7500	2.50	1.95	-2.35	44	0.18	0.06	0.06
SG	CS 29504-006	14.39	0.018	0.35	0.99	6150	3.70	1.60	-2.91	68	0.22	0.06	0.07
SG	CS 29506-007	14.18	0.045	0.33	1.19	5940	3.60	1.50	-2.94	42	0.15	0.06	0.08
SG	CS 29506-090	14.33	0.045	0.36	1.14	5940	3.60	1.35	-3.08	42	0.20	0.06	0.10
BS	CS 29509-027	12.44	0.022	0.29	0.91	6850	3.50	1.65	-2.42	41	0.22	0.06	0.07
SG	CS 29512-073	14.14	0.051	0.52	1.49	5650	3.60	0.90	-1.93	52	0.23	0.07	0.07
HB	CS 29513-003	13.52	0.014	0.48	1.67	5480	1.90	1.75	-2.46	48	0.34	0.06	0.06
HB	CS 29513-014	13.80	0.013	0.70	1.50	5440	1.55	2.00	-2.32	52	0.38	0.06	0.06
SG	CS 29513-015	14.25	0.017	0.35	1.17	6110	3.75	1.35	-2.51	46	0.16	0.06	0.07
SG	CS 29513-031	15.09	0.020	0.33	0.98	6600	4.00	0.75	-2.59	61	0.28	0.07	0.08
SG	CS 29513-032	14.47	0.019	0.44	1.37	6080	3.85	1.30	-1.91	50	0.21	0.06	0.06
SG	CS 29514-007	13.97	0.023	0.37	1.25	6400	3.85	1.75	-2.81	45	0.19	0.06	0.07
RG	CS 29514-017	13.55	0.015	0.62	1.62	5270	2.80	1.20	-2.34	45	0.26	0.06	0.06
SG	CS 29514-018	13.34	0.017	0.48	1.17	5990	3.70	1.25	-2.58	45	0.15	0.06	0.07
SG	CS 29514-037	13.95	0.014	0.49	1.22	5970	3.70	1.15	-2.47	45	0.20	0.06	0.08
SG	CS 29517-018	14.50	0.025	0.41	1.39	5680	3.50	1.55	-2.94	37	0.16	0.06	0.09
SG	CS 29517-042	14.10	0.026	0.36	1.20	6120	3.75	1.40	-2.54	47	0.17	0.06	0.08
SG	CS 29529-054	14.85	0.039	0.49	1.52	5710	3.55	1.65	-2.75	40	0.18	0.06	0.07
RG	CS 30312-044	13.34	0.083	0.70	2.12	4660	1.05	1.65	-3.19	35	0.14	0.06	0.06
RG	CS 30312-059	13.10	0.114	0.69	2.09	4780	1.40	1.65	-3.26	36	0.14	0.06	0.07
HB	CS 30312-062	12.58	0.119	0.21	0.95	6600	2.45	3.00	-2.65	40	0.33	0.06	0.07
RG	CS 30312-100	12.92	0.083	0.63	1.81	5040	2.15	1.30	-2.68	38	0.17	0.06	0.07
RG	CS 30314-067	11.85	0.065	1.13	2.82	4320	0.50	1.85	-3.01	12	0.10	0.06	0.06
SG	CS 30339-015	15.28	0.017	0.38	1.27	5840	3.60	1.45	-2.86	38	0.15	0.06	0.07
HB	CS 30339-046	15.31	0.016	0.37	1.20	7000	2.55	3.15	-2.69	48	0.49	0.06	0.07
HB	CS 30339-052	15.30	0.012	0.48	1.70	5580	2.35	2.10	-2.67	65	0.45	0.06	0.06
SG	CS 30339-069	14.74	0.009	0.15	1.27	5900	3.55	1.15	-3.17	52	0.20	0.06	0.08
RG	CS 30339-073	14.75	0.012	0.53	1.95	4830	1.55	1.50	-3.80	38	0.15	0.06	0.08
SG	CS 30492-001	14.20	0.031	0.42	1.96	5790	3.65	0.85	-2.35	50	0.15	0.07	0.07
SG	CS 30492-016	13.89	0.033	0.42	1.40	5570	3.35	1.50	-3.40	45	0.15	0.06	0.10
RG	CS 30492-110	14.63	0.088	0.67	2.13	4660	1.05	1.80	-3.16	40	0.19	0.06	0.06
SG	CS 30493-071	13.21	0.021	0.40	1.38	5700	3.55	1.30	-2.46	40	0.14	0.06	0.07
RG	CS 30494-003	12.33	0.051	0.63	1.80	4930	1.85	1.35	-2.97	37	0.15	0.06	0.07
RG	CS 31082-001	11.67	0.016	0.75	2.16	4650	1.05	1.55	-3.03	35	0.14	0.06	0.07
RG	BD-20 6008	9.84	0.043	0.83	2.32	4540	0.65	1.70	-3.05	33	0.16	0.06	0.06
RG	BD-18 5550	9.25	0.165	0.75	2.24	4660	1.05	1.60	-3.15	34	0.14	0.06	0.07
RG	BD-15 5781	10.72	0.041	...	2.32	4550	0.70	1.70	-2.87	34	0.14	0.06	0.06
RG	BD-01 2582	9.66	0.022	...	2.00	4920	1.80	1.50	-2.65	40	0.17	0.06	0.07
RG	BD+10 2495	9.72	0.022	...	2.09	4890	1.85	1.50	-2.14	34	0.13	0.06	0.06
MS	BD+19 1185A	9.32	1.127	5440	4.30	1.05	-1.25	41	0.24	0.12	0.06

TABLE 17 — *Continued*

Class ^a	Star	V	$E(B-V)$	$(B-V)_0$	$(V-K)_0$	T_{eff} (K)	$\log g$	v_t (km s ⁻¹)	[M/H]	$\sigma_{T_{\text{eff}}}$ (K)	$\sigma_{\log g}$	σ_{v_t} (km s ⁻¹)	$\sigma_{[\text{M}/\text{H}]}$ ^b
SG	BD+24 1676	10.82	0.057	...	1.13	6140	3.75	1.45	-2.54	43	0.18	0.06	0.08
SG	BD+26 3578	9.36	0.671	6060	3.75	1.30	-2.41	42	0.17	0.06	0.08
RG	BD+29 2356	11.35	0.013	...	2.26	4710	1.75	1.50	-1.62	42	0.20	0.06	0.06
RG	BD+44 493	9.04	0.092	...	1.59	5040	2.10	1.35	-4.26	36	0.14	0.06	0.12
RG	BD+80 245*	10.07	0.026	0.51	1.74	5360	3.15	1.20	-2.01	34	0.22	0.06	0.07
RG	CD-38 245	11.97	0.012	...	2.29	4520	0.65	1.80	-4.50	34	0.13	0.06	0.08
HB	CD-36 1052	9.94	0.025	0.44	1.36	6030	2.05	3.30	-1.86	44	0.24	0.06	0.05
RG	CD-30 298	10.78	0.024	...	1.89	4810	1.50	1.55	-3.72	38	0.15	0.06	0.07
RG	CD-24 1782	9.65	0.020	0.59	1.64	4950	1.90	1.50	-3.02	36	0.14	0.06	0.06
SG	G004-036	11.49	0.099	0.38	1.21	5810	3.65	1.35	-2.22	40	0.17	0.06	0.07
SG	G004-037	11.43	0.153	0.32	1.04	6110	3.75	1.35	-2.67	46	0.18	0.06	0.08
MS	G009-027	12.11	0.022	0.57	1.74	5360	4.15	1.00	-1.81	47	0.27	0.15	0.07
MS	G010-054	12.58	0.016	0.58	1.77	5210	4.40	0.80	-2.30	41	0.53	0.12	0.08
MS	G015-010	12.06	0.088	0.56	1.68	5050	4.05	0.90	-2.54	41	0.30	0.12	0.09
MS	G016-025	13.34	0.053	0.54	1.57	5250	4.10	1.10	-2.07	53	0.31	0.17	0.09
MS	G025-022	12.32	0.088	0.47	1.38	5350	3.95	1.15	-2.33	41	0.25	0.12	0.09
SG	G025-024	11.63	0.056	0.44	1.35	5670	3.55	1.70	-2.28	45	0.15	0.06	0.08
SG	G026-001	11.27	0.062	0.43	1.33	5860	3.75	1.10	-1.94	41	0.17	0.06	0.06
SG	G064-012	11.49	0.030	0.35	1.21	6030	3.60	1.20	-3.39	36	0.18	0.06	0.10
SG	G071-055	10.78	0.026	5550	3.55	1.15	-1.82	39	0.18	0.06	0.07
SG	G075-056	11.94	0.069	0.38	1.20	6190	3.85	1.45	-2.30	51	0.20	0.06	0.09
MS	G088-023	12.04	0.056	0.43	1.34	5640	3.95	1.30	-1.94	44	0.28	0.13	0.08
SG	G090-003	10.43	0.066	0.41	1.38	5680	3.60	1.20	-2.24	37	0.15	0.06	0.07
MS	G090-025*	8.30	0.050	0.56	1.63	5150	4.05	0.90	-2.04	41	0.17	0.12	0.07
SG	G107-050	11.81	0.077	0.41	1.39	6030	3.85	1.20	-1.89	49	0.20	0.06	0.08
MS	G115-049	11.60	0.022	0.48	1.45	5420	3.80	1.30	-2.60	44	0.30	0.13	0.10
SG	G122-069	12.42	0.020	0.41	1.30	6010	3.70	1.65	-2.50	42	0.22	0.06	0.09
SG	G126-062*	9.48	0.053	0.39	1.26	5970	3.85	1.05	-1.70	38	0.18	0.06	0.07
SG	G137-086	13.06	0.043	0.44	1.23	5820	3.75	1.15	-1.76	40	0.16	0.06	0.07
MS	G146-056	13.24	0.017	0.61	1.72	5290	4.05	1.20	-1.57	38	0.22	0.10	0.07
RG	G146-076	10.49	0.010	0.66	1.95	4980	2.10	1.30	-2.13	37	0.17	0.06	0.07
MS	G153-064	11.44	0.237	0.46	1.34	5630	4.15	0.90	-1.09	44	0.27	0.13	0.06
SG	G161-073	10.84	0.052	0.45	1.36	5680	3.90	1.05	-1.07	49	0.22	0.06	0.06
SG	G166-047	12.04	0.016	0.39	1.29	5960	3.70	1.50	-2.28	52	0.19	0.06	0.09
RG	G170-047	8.95	0.064	0.58	1.82	4930	1.85	1.50	-2.90	35	0.12	0.06	0.07
MS	G180-058*	11.31	0.010	0.68	1.89	4980	4.40	0.80	-2.62	41	0.25	0.12	0.09
SG	G186-026	10.82	0.294	0.11	0.43	5950	3.65	1.45	-2.90	45	0.15	0.06	0.08
SG	G188-022*	10.04	0.084	0.41	1.17	5890	3.90	0.95	-1.44	48	0.22	0.06	0.07
MS	G188-030*	11.03	0.109	0.54	1.63	5090	4.30	0.85	-2.07	44	0.20	0.13	0.07
MS	G190-010	11.22	0.237	0.37	1.15	5230	4.35	0.70	-1.94	47	0.29	0.15	0.07
MS	G190-015*	11.04	0.125	0.54	1.61	4950	3.85	1.50	-3.13	41	0.40	0.12	0.09
SG	G199-066	12.68	0.018	0.48	1.46	5560	3.45	1.60	-2.34	42	0.14	0.06	0.09
SG	G201-044	10.51	0.013	0.44	1.41	6000	3.90	1.05	-1.63	42	0.19	0.06	0.06
SG	G206-034	11.40	0.155	0.28	0.94	5930	3.60	1.35	-3.13	38	0.16	0.06	0.09
MS	G214-001	12.08	0.137	0.43	1.31	5370	4.05	0.95	-2.29	44	0.23	0.13	0.09
SG	G234-028	11.10	0.040	0.44	1.34	5870	3.75	1.20	-1.78	41	0.18	0.06	0.07
SG	G238-030	12.91	0.022	0.45	1.38	5740	3.50	1.65	-3.40	53	0.14	0.06	0.12
MS	G238-032	12.66	0.016	0.74	1.67	5380	4.35	0.75	-1.58	47	0.28	0.15	0.08
RG	HD 6268	8.08	0.017	0.84	2.32	4570	0.70	1.85	-2.69	34	0.16	0.06	0.06
RG	HD 11582	9.57	0.016	0.64	1.88	5020	2.20	1.45	-2.03	40	0.17	0.06	0.07
RG	HD 13979	9.18	0.014	...	2.05	4830	1.60	1.60	-2.72	38	0.16	0.06	0.07
SG	HD 16031*	9.77	0.022	0.42	1.26	5870	3.75	0.90	-1.91	38	0.15	0.06	0.07
SG	HD 19445	8.08	0.148	0.30	1.04	5820	3.65	1.25	-2.40	38	0.15	0.06	0.07
RG	HD 21581	8.72	0.123	0.63	1.97	4940	2.10	1.50	-1.82	40	0.20	0.06	0.06
RG	HD 26169	8.76	0.077	0.58	1.91	4750	1.35	1.60	-2.81	34	0.12	0.06	0.06
RG	HD 26297	7.47	0.032	1.05	2.74	4400	1.10	1.75	-1.72	38	0.26	0.06	0.06
SG	HD 31128*	9.14	0.037	0.45	1.31	5630	3.60	1.10	-1.92	42	0.16	0.06	0.06
RG	HD 45282	8.02	0.567	5230	2.90	1.35	-1.73	41	0.25	0.06	0.06
RG	HD 88609	8.57	0.009	0.93	2.54	4430	0.50	1.70	-3.08	35	0.16	0.06	0.07
SG	HD 94028*	8.22	0.027	0.44	1.32	5730	3.70	1.00	-1.81	43	0.20	0.06	0.07
HB	HD 106373	8.92	0.063	...	1.31	6040	1.85	2.90	-2.60	40	0.29	0.06	0.07
RG	HD 108317*	8.05	0.018	...	1.85	5030	2.10	1.45	-2.60	38	0.16	0.06	0.07
HB	HD 119516	9.09	0.032	...	1.64	5660	1.90	1.90	-1.93	40	0.29	0.06	0.06
SG	HD 122196*	8.73	0.092	0.37	1.21	5880	3.80	1.20	-1.79	45	0.22	0.06	0.06
RG	HD 122563*	6.20	0.025	0.88	2.39	4500	0.55	1.95	-2.93	34	0.15	0.06	0.07
RG	HD 126238*	7.66	0.115	0.69	2.00	4750	1.65	1.55	-1.96	37	0.23	0.06	0.06
RG	HD 126587	9.12	0.100	0.73	2.18	4640	1.00	1.75	-3.21	34	0.13	0.06	0.07
RG	HD 128279*	8.02	0.100	0.54	1.68	5050	2.15	1.55	-2.64	38	0.16	0.06	0.07
SG	HD 132475*	8.55	0.107	0.44	1.35	5410	3.50	1.00	-1.65	40	0.25	0.06	0.07
RG	HD 175305	7.18	0.105	0.64	1.83	4920	2.30	1.40	-1.56	42	0.22	0.06	0.06
SG	HD 175606	9.78	0.063	0.38	1.23	5920	3.70	1.20	-2.24	45	0.18	0.06	0.07
HB	HD 178443	9.98	0.090	0.63	1.82	5170	1.45	1.85	-2.02	48	0.32	0.06	0.06

TABLE 17 — *Continued*

Class ^a	Star	V	$E(B - V)$	$(B - V)_0$	$(V - K)_0$	T_{eff} (K)	$\log g$	v_t (km s ⁻¹)	[M/H]	$\sigma_{T_{\text{eff}}}$ (K)	$\sigma_{\log g}$	σ_{v_t} (km s ⁻¹)	$\sigma_{[\text{M}/\text{H}]}$ ^b
HB	HD 184266	7.60	0.128	0.45	1.42	5780	1.85	2.55	-1.74	44	0.24	0.06	0.06
RG	HD 186478	9.15	0.114	0.86	2.39	4540	0.65	1.75	-2.78	34	0.14	0.06	0.06
MS	HD 188510	8.82	0.217	5210	4.10	0.80	-1.88	44	0.27	0.13	0.07
MS	HD 193901	8.65	0.060	0.49	1.35	5580	4.05	1.10	-1.28	47	0.24	0.15	0.06
SG	HD 196892	8.24	0.044	0.46	1.30	5670	3.85	1.05	-1.24	49	0.17	0.06	0.06
HB	HD 196944	8.38	0.042	...	1.74	5310	1.75	1.65	-2.39	48	0.33	0.06	0.06
RG	HD 200654	9.08	0.029	0.61	1.85	5080	2.25	1.35	-3.06	36	0.14	0.06	0.08
MS	HD 201891	7.37	0.111	0.40	1.14	5840	4.10	1.10	-1.21	41	0.32	0.12	0.07
HB	HD 214362	9.09	0.027	0.47	1.48	5760	1.60	2.25	-2.04	48	0.26	0.06	0.06
SG	HD 219617	8.16	0.033	0.44	1.30	5730	3.70	1.30	-1.83	37	0.16	0.06	0.07
RG	HD 220127	10.15	0.012	0.65	1.93	5060	2.40	1.30	-1.85	40	0.19	0.06	0.07
RG	HD 237846	9.96	0.011	...	2.11	4730	1.30	1.45	-3.14	34	0.13	0.06	0.07
RG	HE 0454-4758	13.48	0.010	0.56	1.78	5140	2.40	1.35	-3.32	40	0.18	0.06	0.08
SG	HE 0938+0114	10.21	0.101	0.17	0.67	6030	3.65	1.20	-2.92	42	0.17	0.06	0.10
RG	HE 1012-1540	14.04	0.070	...	1.72	5230	2.65	1.70	-3.76	32	0.20	0.06	0.14
RG	HE 1124-2335	14.63	0.047	0.65	2.08	4870	1.65	1.45	-3.26	23	0.14	0.06	0.07
RG	HE 1320-1339	10.26	0.066	1.01	1.70	4690	1.20	1.75	-2.93	34	0.14	0.06	0.06
SG	HIP 99423	8.88	0.577	5520	3.70	1.05	-1.42	41	0.20	0.06	0.07

^a Classification scheme: BS = blue straggler-like stars warmer than the main sequence turnoff; HB = stars on the horizontal branch; MS = stars on the main sequence; RG = stars on the red giant branch; SG = stars on the subgiant branch.

^b $\sigma_{[\text{M}/\text{H}]} = \sigma_{\text{Fe II}}$

* Star with reliable parallax and $E(B - V) < 0.12$

TABLE 18
LINE ABUNDANCE CORRECTIONS AND UNCERTAINTIES

Species	Wavelength (Å)	RG		SG		HB		MS	
		Correction	σ	Correction	σ	Correction	σ	Correction	σ
O I	7771.94	-0.50	0.25	-0.50	0.25	-0.50	0.25	-0.50	0.25
O I	7774.17	-0.50	0.25	-0.50	0.25	-0.50	0.25	-0.50	0.25
O I	7775.39	-0.50	0.25	-0.50	0.25	-0.50	0.25	-0.50	0.25
Na I	5682.63	+0.00	0.13	+0.00	0.13	+0.00	0.13	+0.00	0.13
Na I	5688.20	+0.00	0.13	+0.00	0.13	+0.00	0.13	+0.00	0.13
Na I	5889.95	+0.01	0.06	+0.01	0.06	+0.01	0.06	+0.01	0.06
Na I	5895.92	-0.01	0.06	-0.01	0.06	-0.01	0.06	-0.01	0.06
Mg I	3829.36	+0.04	0.08	+0.19	0.07	+0.04	0.08
Mg I	3832.30	+0.14	0.09	+0.34	0.07
Mg I	3838.29	+0.18	0.10	+0.44	0.04
Mg I	4057.51	+0.02	0.07	-0.01	0.07	+0.02	0.09	-0.01	0.16
Mg I	4167.27	-0.05	0.09	-0.02	0.05	+0.04	0.07	-0.11	0.07
Mg I	4702.99	+0.06	0.04	+0.05	0.06	+0.12	0.05	+0.10	0.10
Mg I	5172.68	-0.05	0.07	-0.08	0.08	-0.20	0.11	-0.11	0.04
Mg I	5183.60	-0.10	0.07	-0.09	0.08	-0.35	0.13	-0.13	0.09
Mg I	5528.40	-0.05	0.08	-0.05	0.05	-0.02	0.05	-0.01	0.08
Mg I	5711.09	-0.02	0.13	-0.02	0.08	-0.06	0.08	+0.00	0.06
Al I	3944.00	-0.04	0.09	-0.04	0.08	-0.01	0.10
Al I	3961.52	+0.04	0.09	+0.04	0.08	+0.01	0.10
Si I	3905.52	+0.14	0.16	+0.14	0.16	+0.14	0.16	+0.14	0.16
Si I	4102.94	+0.14	0.16	+0.14	0.16	+0.14	0.16	+0.14	0.16
Si I	5665.55	+0.02	0.11	+0.02	0.11	+0.02	0.11	+0.02	0.11
Si I	5701.10	+0.02	0.11	+0.02	0.11	+0.02	0.11	+0.02	0.11
Si I	5708.40	+0.00	0.11	+0.00	0.11	+0.00	0.11	+0.00	0.11
Si I	5772.15	-0.04	0.13	-0.04	0.13	-0.04	0.13	-0.04	0.13
K I	7664.90	+0.01	0.09	+0.01	0.09	+0.01	0.09	+0.01	0.09
K I	7698.96	-0.01	0.09	-0.01	0.09	-0.01	0.09	-0.01	0.09
Ca I	4226.73	+0.18	0.07	+0.06	0.13	-0.23	0.06
Ca I	4283.01	-0.09	0.08	+0.01	0.04	+0.03	0.05	+0.01	0.06
Ca I	4318.65	+0.07	0.04	+0.05	0.04	+0.08	0.04	+0.11	0.05
Ca I	4425.44	+0.05	0.07	+0.05	0.05	+0.09	0.03	+0.07	0.07
Ca I	4434.96	+0.01	0.06	+0.02	0.04	+0.05	0.07	-0.01	0.02
Ca I	4435.69	+0.02	0.05	+0.05	0.06	+0.00	0.05	+0.05	0.06
Ca I	4454.78	+0.10	0.06	+0.08	0.04	+0.09	0.04	+0.10	0.05
Ca I	4455.89	+0.05	0.06	+0.07	0.06	+0.03	0.12	+0.09	0.05
Ca I	5588.76	-0.05	0.05	-0.09	0.08	-0.05	0.05	-0.11	0.04
Ca I	5857.45	-0.05	0.11	-0.06	0.07	-0.05	0.06	-0.07	0.07
Ca I	6102.72	-0.06	0.07	-0.08	0.08	-0.14	0.07	-0.06	0.04
Ca I	6122.21	-0.10	0.04	-0.08	0.06	-0.09	0.05	-0.09	0.03
Ca I	6162.17	-0.07	0.02	-0.07	0.06	-0.07	0.04	-0.07	0.04
Ca I	6439.07	+0.09	0.05	+0.07	0.06	+0.10	0.03	+0.07	0.07
Sc II	3576.34	-0.10	0.14	-0.10	0.12	-0.21	0.21
Sc II	3590.47	-0.23	0.17	-0.04	0.11	-0.13	0.14
Sc II	3645.31	-0.14	0.12	+0.00	0.06	-0.11	0.10
Sc II	4246.82	+0.08	0.10	-0.04	0.09	-0.06	0.09	+0.04	0.03
Sc II	4400.39	+0.03	0.04	+0.00	0.04	+0.05	0.05	+0.00	0.02
Sc II	4415.54	+0.03	0.04	+0.01	0.05	+0.06	0.03	+0.01	0.03
Sc II	4670.41	-0.02	0.04	+0.02	0.05	+0.03	0.06	+0.04	0.02
Sc II	5526.79	+0.01	0.05	+0.03	0.05	+0.01	0.06	+0.02	0.04
Sc II	5657.91	-0.03	0.07	-0.02	0.03	-0.03	0.10	-0.08	0.02
Ti I	3989.76	-0.01	0.10	-0.09	0.06	-0.05	0.18	-0.06	0.02
Ti I	3998.64	+0.05	0.08	-0.01	0.07	+0.08	0.09	+0.02	0.03
Ti I	4512.73	-0.02	0.09	+0.03	0.04	+0.00	0.07	+0.01	0.04
Ti I	4518.02	-0.01	0.10	-0.01	0.05	-0.02	0.02	+0.01	0.04
Ti I	4533.24	+0.03	0.05	-0.01	0.04	+0.05	0.07	+0.01	0.04
Ti I	4534.78	+0.04	0.04	+0.01	0.05	+0.07	0.08	+0.03	0.02
Ti I	4548.76	+0.02	0.08	+0.03	0.07	+0.02	0.11	+0.03	0.03
Ti I	4555.48	+0.02	0.08	+0.05	0.08	-0.03	0.10	+0.05	0.02
Ti I	4656.47	+0.01	0.08	+0.01	0.06	-0.02	0.15	+0.00	0.02
Ti I	4681.91	+0.01	0.06	+0.01	0.11	+0.01	0.05	+0.00	0.03
Ti I	4840.87	-0.02	0.11	+0.02	0.06	-0.02	0.18	+0.04	0.06
Ti I	4981.73	+0.03	0.06	+0.02	0.07	+0.07	0.12	+0.03	0.02
Ti I	4991.07	-0.03	0.07	-0.06	0.11	-0.02	0.07	-0.08	0.04
Ti I	4999.50	-0.02	0.10	-0.01	0.06	-0.03	0.08	-0.04	0.06
Ti I	5016.16	-0.04	0.10	+0.01	0.02	+0.03	0.04	-0.01	0.10
Ti I	5064.65	-0.05	0.08	-0.03	0.06	-0.07	0.02	-0.04	0.02
Ti I	5173.74	-0.01	0.08	-0.03	0.14	-0.03	0.04
Ti I	5192.97	-0.03	0.09	-0.01	0.09	-0.04	0.06	-0.03	0.02
Ti I	5210.38	+0.01	0.09	+0.00	0.06	-0.03	0.07	-0.14	0.09
Ti II	3372.79	+0.05	0.18
Ti II	3387.83	+0.00	0.15	-0.03	0.11
Ti II	3394.57	-0.02	0.20	-0.08	0.11
Ti II	3456.38	+0.24	0.07	+0.21	0.11
Ti II	3477.18	-0.17	0.05

TABLE 18 — *Continued*

Species	Wavelength (Å)	RG		SG		HB		MS	
		Correction	σ	Correction	σ	Correction	σ	Correction	σ
Ti II	3489.74	-0.23	0.13	-0.10	0.13
Ti II	3491.05	-0.11	0.14	-0.05	0.09
Ti II	3759.29	-0.01	0.07	-0.04	0.05
Ti II	3761.32	-0.04	0.08	+0.00	0.08	+0.02	0.12
Ti II	3913.46	-0.13	0.11	-0.11	0.09	+0.06	0.04
Ti II	4028.34	+0.06	0.11	+0.06	0.07	+0.08	0.06	-0.04	0.11
Ti II	4337.91	+0.05	0.08
Ti II	4394.06	+0.01	0.05	+0.05	0.08	+0.01	0.04	-0.04	0.08
Ti II	4395.03	-0.09	0.09	-0.08	0.10	-0.18	0.12	-0.06	0.11
Ti II	4395.84	+0.09	0.07	+0.12	0.05	+0.06	0.03	+0.13	0.12
Ti II	4398.29	+0.23	0.07
Ti II	4399.77	-0.04	0.08	-0.02	0.10	+0.05	0.05	-0.07	0.15
Ti II	4409.52	+0.09	0.05	+0.02	0.13
Ti II	4417.71	-0.03	0.07	-0.03	0.08	+0.02	0.03	-0.01	0.08
Ti II	4418.33	+0.03	0.06	+0.04	0.07	+0.02	0.06	-0.06	0.04
Ti II	4443.80	-0.02	0.09	-0.13	0.09	-0.06	0.06	-0.01	0.06
Ti II	4444.55	+0.03	0.05	+0.08	0.08	+0.05	0.05	+0.08	0.05
Ti II	4450.48	-0.04	0.07	-0.03	0.07	-0.01	0.04	-0.01	0.09
Ti II	4464.45	-0.01	0.04	+0.04	0.05	+0.01	0.02	-0.03	0.04
Ti II	4470.85	+0.13	0.06	+0.16	0.05	+0.14	0.04	+0.12	0.06
Ti II	4493.52	+0.10	0.08	+0.16	0.10	+0.11	0.12	+0.20	0.05
Ti II	4501.27	-0.06	0.08	-0.15	0.08	-0.05	0.06	-0.07	0.07
Ti II	4533.96	-0.05	0.11	-0.10	0.11	-0.08	0.07	-0.06	0.09
Ti II	4571.97	+0.03	0.12	-0.09	0.11	-0.02	0.07	-0.09	0.10
Ti II	4583.41	-0.01	0.12	+0.10	0.10	-0.10	0.12	+0.04	0.06
Ti II	4636.32	+0.13	0.08
Ti II	4657.20	+0.01	0.07	+0.04	0.06	+0.00	0.00	+0.07	0.06
Ti II	4708.66	-0.02	0.08	+0.08	0.05	+0.03	0.08	+0.05	0.07
Ti II	4798.53	-0.04	0.08	+0.04	0.10	-0.13	0.11	+0.04	0.09
Ti II	5129.16	-0.01	0.11	-0.02	0.10	+0.02	0.10	-0.04	0.05
Ti II	5185.90	+0.08	0.09	+0.05	0.08	+0.11	0.11
Ti II	5188.69	-0.08	0.12	-0.10	0.10	-0.03	0.10	-0.16	0.13
Ti II	5226.54	-0.01	0.06	+0.00	0.07	+0.05	0.06	-0.04	0.03
Ti II	5336.79	+0.02	0.06	+0.07	0.06	+0.08	0.05	+0.01	0.06
Ti II	5381.02	-0.02	0.08	+0.03	0.06	-0.04	0.05	+0.01	0.04
Ti II	5418.77	-0.02	0.08	-0.01	0.10	+0.07	0.03	+0.00	0.05
V II	3951.96	+0.06	0.09	+0.04	0.12	+0.04	0.10	+0.03	0.17
V II	4005.71	-0.06	0.09	-0.04	0.12	-0.04	0.10	-0.03	0.17
Cr I	3578.68	+0.11	0.14	-0.06	0.18	-0.02	0.13
Cr I	4274.80	+0.01	0.11	-0.09	0.09	-0.01	0.14
Cr I	4289.72	+0.10	0.17	+0.00	0.08	+0.18	0.13	+0.07	0.05
Cr I	4545.95	-0.01	0.07	+0.00	0.06	-0.02	0.13	+0.03	0.08
Cr I	4646.15	+0.01	0.04	-0.03	0.03	+0.03	0.05	-0.02	0.03
Cr I	4651.28	-0.03	0.12	+0.00	0.06	-0.04	0.04	-0.02	0.07
Cr I	4789.34	-0.06	0.08	-0.06	0.12	-0.02	0.05
Cr I	5206.04	+0.00	0.08	-0.07	0.08	-0.04	0.14	+0.00	0.06
Cr I	5296.69	-0.03	0.07	+0.04	0.08	-0.06	0.15	+0.00	0.03
Cr I	5298.28	-0.06	0.06	-0.01	0.05	-0.05	0.06	-0.06	0.09
Cr I	5300.74	+0.10	0.05	+0.01	0.11	+0.09	0.05
Cr I	5345.80	-0.01	0.07	+0.02	0.04	-0.02	0.09	-0.04	0.06
Cr I	5348.31	+0.05	0.07	+0.06	0.06	+0.02	0.11	+0.00	0.04
Cr I	5409.77	+0.00	0.06	+0.01	0.06	+0.01	0.04	-0.06	0.11
Cr II	3408.74	+0.09	0.11	+0.08	0.20
Cr II	4558.59	-0.03	0.07	-0.03	0.05	-0.05	0.06	-0.02	0.07
Cr II	4588.14	+0.04	0.05	+0.01	0.05	+0.00	0.04	+0.03	0.09
Cr II	4591.99	-0.03	0.07	+0.03	0.07	+0.06	0.09	-0.02	0.08
Mn I	4030.75	+0.15	0.19	+0.11	0.25	+0.33	0.22	-0.12	0.19
Mn I	4033.06	+0.38	0.13	+0.23	0.17	+0.40	0.14	+0.07	0.08
Mn I	4034.48	+0.38	0.09	+0.20	0.14	+0.33	0.14	-0.02	0.27
Mn I	4041.35	+0.04	0.06	+0.01	0.08	+0.02	0.06	-0.01	0.11
Mn I	4754.04	+0.00	0.06	+0.02	0.09	-0.01	0.05	+0.07	0.09
Mn I	4762.37	-0.06	0.07	-0.08	0.08	-0.06	0.07	-0.01	0.14
Mn I	4823.52	-0.01	0.06	+0.02	0.08	+0.02	0.03	-0.03	0.07
Mn I	6021.82	-0.03	0.08	-0.03	0.05	-0.05	0.06
Mn II	3441.99	+0.01	0.10	+0.00	0.14	-0.09	0.07	+0.03	0.05
Mn II	3460.32	+0.05	0.12	+0.01	0.09	+0.05	0.04	-0.01	0.05
Mn II	3482.90	+0.06	0.11	+0.01	0.10	+0.01	0.11	+0.01	0.08
Mn II	3488.68	-0.05	0.12	-0.02	0.08	+0.05	0.17	+0.00	0.11
Mn II	3497.53	-0.11	0.09	-0.03	0.08	-0.06	0.09	-0.05	0.15
Co I	3409.18	+0.11	0.05
Co I	3412.34	-0.09	0.16	+0.05	0.15	+0.05	0.15	+0.05	0.15
Co I	3412.63	-0.24	0.09	-0.18	0.14	-0.18	0.14	-0.18	0.14
Co I	3449.44	+0.10	0.06	+0.02	0.03	+0.02	0.03	+0.02	0.03
Co I	3502.28	+0.38	0.13	+0.15	0.09	+0.15	0.09	+0.15	0.09
Co I	3518.34	+0.19	0.07	+0.12	0.10	+0.12	0.10	+0.12	0.10

TABLE 18 — *Continued*

Species	Wavelength (Å)	RG		SG		HB		MS	
		Correction	σ	Correction	σ	Correction	σ	Correction	σ
Co I	3521.57	-0.06	0.08	-0.04	0.04	-0.04	0.04	-0.04	0.04
Co I	3529.03	+0.07	0.11	-0.05	0.07	-0.05	0.07	-0.05	0.07
Co I	3842.05	-0.10	0.08	-0.10	0.06	-0.10	0.06	-0.10	0.06
Co I	3845.47	-0.02	0.07	-0.02	0.05	-0.02	0.05	-0.02	0.05
Co I	3894.08	+0.07	0.07	+0.10	0.02	+0.10	0.02	+0.10	0.02
Co I	4121.32	-0.11	0.07	-0.02	0.04	-0.02	0.04	-0.02	0.04
Ni I	3437.28	-0.05	0.14	+0.01	0.12
Ni I	3452.89	+0.02	0.15	-0.07	0.11
Ni I	3472.54	+0.13	0.13	-0.05	0.13
Ni I	3492.96	+0.20	0.11	+0.04	0.12
Ni I	3500.85	-0.02	0.15	-0.08	0.12	-0.02	0.20	-0.07	0.23
Ni I	3519.77	+0.01	0.14	+0.06	0.08
Ni I	3524.54	+0.11	0.08	+0.06	0.14
Ni I	3597.70	+0.14	0.15	+0.03	0.09	+0.09	0.07	+0.05	0.28
Ni I	3783.53	+0.03	0.13	+0.08	0.07	+0.25	0.14
Ni I	3807.14	+0.15	0.14	+0.08	0.09	+0.19	0.13	+0.20	0.16
Ni I	4605.00	+0.02	0.08	+0.04	0.09	+0.07	0.04	+0.05	0.02
Ni I	4686.22	+0.07	0.04	-0.01	0.06	-0.01	0.12
Ni I	4904.41	-0.05	0.09	-0.04	0.09	+0.00	0.05	+0.00	0.04
Ni I	5081.11	-0.04	0.08	-0.01	0.10	+0.01	0.09	+0.06	0.07
Ni I	5084.08	+0.04	0.08	+0.06	0.10	+0.02	0.06	+0.13	0.04
Ni I	5115.40	-0.02	0.11	-0.02	0.06	+0.04	0.08
Ni I	5155.76	+0.02	0.06	-0.03	0.06	-0.02	0.12
Ni I	5476.91	-0.06	0.09	-0.14	0.09	-0.12	0.05	-0.23	0.12
Ni I	6643.64	-0.05	0.09	-0.05	0.05	-0.02	0.04	-0.09	0.08
Ni I	6767.77	-0.05	0.06	-0.02	0.04	+0.01	0.02	-0.11	0.03
Zn I	4680.14	-0.07	0.09	-0.05	0.10	-0.05	0.12
Zn I	4722.16	+0.04	0.12	+0.01	0.16	-0.02	0.15	+0.00	0.10
Zn I	4810.54	+0.08	0.12	+0.04	0.16	+0.06	0.15	+0.00	0.10
Sr II	4077.71	+0.00	0.12	+0.00	0.12	-0.01	0.16	+0.03	0.14
Sr II	4215.52	+0.00	0.12	+0.00	0.12	+0.01	0.16	-0.03	0.14
Y II	3600.73	+0.01	0.11	-0.06	0.19	-0.05	0.15	-0.06	0.19
Y II	3774.33	-0.01	0.12	-0.05	0.08	+0.00	0.13	-0.05	0.08
Y II	4398.01	+0.08	0.08	+0.16	0.05	+0.10	0.07	+0.16	0.05
Y II	4883.68	-0.02	0.06	+0.01	0.07	-0.04	0.06	+0.01	0.07
Y II	5087.42	-0.06	0.07	-0.01	0.06	-0.09	0.08	-0.01	0.06
Y II	5200.41	-0.01	0.09	+0.06	0.06	+0.02	0.09	+0.06	0.06
Y II	5205.72	-0.05	0.04	-0.09	0.06	-0.09	0.06
Zr II	4149.20	-0.04	0.12	-0.04	0.12	-0.03	0.12	-0.04	0.10
Zr II	4161.20	+0.03	0.12	+0.00	0.12	-0.01	0.12	+0.03	0.10
Zr II	4208.98	+0.00	0.12	+0.05	0.12	+0.05	0.12	+0.01	0.10
Ba II	4554.03	+0.05	0.11	+0.01	0.09	-0.04	0.17	+0.01	0.09
Ba II	5853.68	+0.11	0.05	+0.08	0.09	+0.16	0.13	+0.08	0.09
Ba II	6141.71	+0.00	0.06	-0.02	0.06	-0.07	0.11	-0.02	0.06
Ba II	6496.90	-0.13	0.04	-0.10	0.05	-0.22	0.12	-0.10	0.05
La II	3988.51	+0.04	0.05	+0.04	0.06	+0.02	0.03	+0.04	0.06
La II	3995.74	+0.05	0.04	+0.05	0.05	+0.00	0.05	+0.05	0.05
La II	4086.71	-0.05	0.06	-0.08	0.04	-0.06	0.06	-0.08	0.04
La II	4123.22	-0.01	0.05	+0.01	0.06	+0.06	0.06	+0.01	0.06
Ce II	3999.24	+0.06	0.06	+0.06	0.06	+0.06	0.06	+0.06	0.06
Ce II	4073.47	+0.04	0.03	+0.04	0.03	+0.04	0.03	+0.04	0.03
Ce II	4083.22	-0.01	0.06	-0.01	0.06	-0.01	0.06	-0.01	0.06
Ce II	4418.78	-0.05	0.08	-0.05	0.08	-0.05	0.08	-0.05	0.08
Ce II	4562.36	-0.03	0.04	-0.03	0.04	-0.03	0.04	-0.03	0.04
Pr II	4062.80	-0.13	0.20	-0.13	0.20	-0.13	0.20	-0.13	0.20
Pr II	4143.13	+0.04	0.20	+0.04	0.20	+0.04	0.20	+0.04	0.20
Pr II	4179.40	-0.10	0.20	-0.10	0.20	-0.10	0.20	-0.10	0.20
Pr II	4222.95	+0.13	0.20	+0.13	0.20	+0.13	0.20	+0.13	0.20
Pr II	4408.81	+0.05	0.20	+0.05	0.20	+0.05	0.20	+0.05	0.20
Nd II	4109.45	-0.10	0.08	-0.10	0.08	-0.10	0.08	-0.10	0.08
Nd II	4446.38	+0.10	0.06	+0.10	0.06	+0.10	0.06	+0.10	0.06
Nd II	4462.98	-0.06	0.04	-0.06	0.04	-0.06	0.04	-0.06	0.04
Nd II	4706.54	+0.01	0.04	+0.01	0.04	+0.01	0.04	+0.01	0.04
Nd II	4825.48	+0.03	0.04	+0.03	0.04	+0.03	0.04	+0.03	0.04
Sm II	4424.34	+0.05	0.10	+0.05	0.10	+0.05	0.10	+0.05	0.10
Sm II	4467.34	-0.05	0.10	-0.05	0.10	-0.05	0.10	-0.05	0.10
Eu II	3819.67	+0.02	0.05	+0.02	0.05	+0.02	0.05	+0.02	0.05
Eu II	3907.11	+0.02	0.06	+0.02	0.06	+0.02	0.06	+0.02	0.06
Eu II	4129.72	-0.02	0.07	-0.02	0.07	-0.02	0.07	-0.02	0.07
Eu II	4205.04	-0.02	0.04	-0.02	0.04	-0.02	0.04	-0.02	0.04
Gd II	4049.85	+0.02	0.08	+0.02	0.08	+0.02	0.08	+0.02	0.08
Gd II	4130.37	-0.10	0.08	-0.10	0.08	-0.10	0.08	-0.10	0.08
Gd II	4251.73	+0.09	0.08	+0.09	0.08	+0.09	0.08	+0.09	0.08
Dy II	3757.37	+0.05	0.20	+0.05	0.20	+0.05	0.20	+0.05	0.20
Dy II	3944.68	+0.07	0.20	+0.07	0.20	+0.07	0.20	+0.07	0.20

TABLE 18 — *Continued*

Species	Wavelength (Å)	RG		SG		HB		MS	
		Correction	σ	Correction	σ	Correction	σ	Correction	σ
Dy II	4103.31	-0.15	0.20	-0.15	0.20	-0.15	0.20	-0.15	0.20
Dy II	4449.70	+0.04	0.20	+0.04	0.20	+0.04	0.20	+0.04	0.20
Er II	3729.52	-0.01	0.09	-0.01	0.09	-0.01	0.09	-0.01	0.09
Er II	3830.48	+0.02	0.03	+0.02	0.03	+0.02	0.03	+0.02	0.03
Er II	3896.23	-0.02	0.06	-0.02	0.06	-0.02	0.06	-0.02	0.06